Dynamics of Surfactants
at Soft Interfaces using
Droplet-Based Microfluidics

Dissertation

for the award of the degree

"Doctor rerum naturalium"

of the Georg-August-Universität Göttingen

within the doctoral program

Göttingen Graduate School

for Neurosciences, Biophysics and Molecular Biosciences (GGNB)

of the Georg-August University School of Science (GAUSS)

submitted by

Birte Riechers

from Bielefeld, Germany

Göttingen, 2015

Thesis Committee

Prof. Dr. Jean-Christophe Baret

Soft Micro Systems, Centre de Recherche Paul Pascal (CNRS)

University of Bordeaux, Pessac, France

Max Planck Research Group 'Droplets, Membranes and Interfaces'

Max Planck Institute for Dynamics and Self-Organization, Göttingen, Germany

Prof. Dr. Sarah Köster

Nanoscale Imaging of Cellular Dynamics, Institute for X-ray Physics

Georg-August University, Göttingen, Germany

Asst. Prof. Dr. Oskar Hallatschek

Biophysics and Evolutionary Dynamics Group

Departments of Physics and Integrative Biology

University of California, Berkeley, USA

Members of the Examination Board

Referee:

Prof. Dr. Jean-Christophe Baret

Soft Micro Systems, Centre de Recherche Paul Pascal (CNRS)

University of Bordeaux, Pessac, France

Max Planck Research Group 'Droplets, Membranes and Interfaces'

Max Planck Institute for Dynamics and Self-Organization, Göttingen, Germany

2nd Referee

Prof. Dr. Sarah Köster

Nanoscale Imaging of Cellular Dynamics, Institute for X-ray Physics

Georg-August University, Göttingen, Germany

Further members of the Examination Board

Asst. Prof. Dr. Oskar Hallatschek

Biophysics and Evolutionary Dynamics Group

Departments of Physics and Integrative Biology

University of California, Berkeley, USA

Prof. Dr. Philipp Vana

Macromolecular Chemistry

Institute of Physical Chemistry

Georg-August University, Göttingen, Germany

Dr. Thomas Burg

Department for Biological Micro- and Nanotechnology

Max Planck Institute for Biophysical Chemistry, Göttingen, Germany

Dr. Manfred Konrad

Department of Enzyme Biochemistry

Max Planck Institute for Biophysical Chemistry, Göttingen, Germany
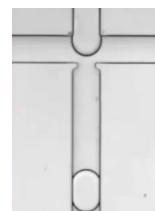
Date of oral examination: 21.12.2015

The following work is subject of the following publications. The sections which are overlapping strongly with these papers are annotated. Small overlaps in other sections, though, are possible as well.

P. Gruner, B. Riechers, L. Chacon, Q. Brosseau, F. Maes, T. Beneyton, D. Pekin, J.-C. Baret, Stabilisers for water-in-fluorinated-oil dispersions: Key properties for microfluidic applications, *Current Opinion in Colloid & Interface Science* **2015**, *20* (3), 183-191, DOI:10.1016/j.cocis.2015.07.005.

P. Gruner, B. Riechers, J. Lim, A. Johnston, K. Short, J.-C. Baret, Surfactant Control of Molecular Transport in Minimal Emulsions, *Nature Communications* **2015**, in press.

B. Riechers, F. Maes, E. Akoury, B. Semin, P. Gruner, J.-C. Baret, working title: Dynamics of surfactant adsorption at soft interfaces in droplet-based microfluidics, *in preparation* **2015**.
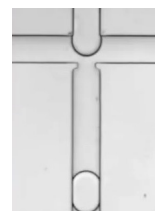
F. Maes, D. Pekin, B. Riechers, J. Vrignon, J.-C. Baret, working title: Active soft matter: From biomimetics to self-sorting bioreactors, *in preparation* **2015**.

Contents

Chapter 1

Introduction

"Without interfaces, there is only bulk" (by Dirk Aarts[1]).

An interface is the boundary between two immiscible fluid phases having dissimilar physico-chemical properties[1,2]. From a simple mathematical viewpoint, the interface corresponds to the two dimensional surface dividing a volume into two parts with each of them containing one of the two media[3].

Some two phase systems can be solely described by the physical properties of the interface[3]. A soap film can, for example, be considered as a pure two-dimensional object. The mathematical description of the interface is sufficient to explain why bubbles minimise their surface area[3], but in practice the complete physics of the foam cannot be captured with such a minimal model. In reality soap films age and eventually break[3]. The underlying mechanisms are related to the molecular dynamics occurring within the soap film and this description becomes important in understanding the dynamic properties of the film. Thermal fluctuations influence dynamic processes that occur on the molecular length-scale[4–6]. Throughout my thesis, I will focus on interfaces in liquid-liquid systems, in which the interface is the diffuse layer of molecules where the thermodynamic properties vary abruptly from their bulk values in one phase to those in the other phase[1,6]. From this perspective, the interface corresponds to a soft object in which dynamic processes occur[4]. Surface active molecules (surfactants) increase the complexity of the dynamics

---

[1]Talk at the "Symposium: Frontiers of Soft Matter Research", Institute of Science and Technology Austria, 2014.
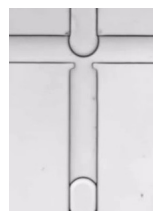
of the interface by coupling to these dynamic processes[2,7]. This interconnection affects not only the properties of the interface but also influences macroscopic properties[7,8].

For convenience, I have started with the discussion on foams and soap films, but interfaces are ubiquitous in nature and technological systems. The analogues of soap films in water are vesicles or liposomes. These lipid membranes are essential for living systems, in which the function of the membrane is to separate (up to a certain extent) the inner part from the outer part of the cell[9,10]. Additionally, interfaces are prevalent in all types of dispersions such as aerosols and emulsions[1,2].

Emulsions are omnipresent in man-made systems throughout industrial applications. They are widely used in paint materials, paper coatings as well as in the cosmetic and the food industry[1,4,5]. Monodisperse aqueous droplets of emulsions become evermore attractive for use as separate microreactors in biotechnological, pharmaceutical and medical applications[4,5,7,11–15]. These droplets can be produced and precisely controlled using droplet-based microfluidics[5,7,11,16–19]. Using microfluidics, a detection of molecules with high-sensitivity and high-throughput is feasible while using only small volumes in the range of picolitres[11,17–20]. Biological material can be encapsulated in the aqueous emulsion droplets to obtain information on the single cell or single enzyme level[5,11–15]. Likewise, it is possible to find rare mutations to perform directed evolution experiments[14,17,20]. The utilization of emulsion droplets can enhance chemical synthesis[21] and open new ways for complex particle synthesis[22,23].

All these applications require constant experimental conditions, which means that the metastable aqueous emulsion droplets need to be kinetically stabilised against coalescence while the transport of molecules through the interface needs to be suppressed as well[7,24,25]. Stabilisation against coalescence can be obtained using surfactants. These molecules adsorb to interfaces and stabilise the emulsions. This stabilisation is due to a reduction of interfacial tension, steric repulsion between surfactant molecules and the coupling of surfactants to hydrodynamic flows (Marangoni effect)[7,26,27]. However, the stabilisation against transport is more ambitious than that of coalescence as surfactants can increase the solubility of solutes inside the oil phase[28]. Surfactants are also involved in other transport processes such as the diffusive transport leading to Ostwald ripening, which is a major effect controlling the ageing of emulsions[29]. **In general, all**

processes which influence the lifetime of emulsions, such as coalescence, exchange and loss of molecules are affected by surfactants [4,5,7,18,19,28]. The dynamics of surfactants at interfaces influence not only the stabilisation and the exchange across the interface, but surfactants also interact with the dispersed and the continuous phase. The coupling between the adsorbed surfactant and the continuous phase can for example induce self-propulsion of droplets via e. g. the Marangoni effect. Droplet emulsions out of equilibrium could become a model system in the steadily growing field of active systems to understand the phenomena of self-organisation [30,31], the swarming behaviour of biological systems and the collective behaviour of micro-organisms [31]. The use of minimal systems paves the way to understand and mimic primitive cells which sense and react to their environment [32].

As surfactants influence all these out-of-equilibrium processes, the dynamics of surfactant adsorption are of great importance in understanding how these molecules affect macroscopic properties of emulsions [7,8]. The adsorption kinetics are controlled by two limiting cases, either being restricted by the diffusion of molecules towards the interface or by the adsorption process itself [33–41]. The dynamics of surfactant adsorption at small length scales, such as in emulsions, are mainly adsorption limited and differ from those at larger scales [41]. The presence of adsorption and desorption barriers, though, is far from understood as their experimental determination is challenging due to the fact that the kinetics of adsorption often differ only slightly from the diffusion limited regime [40]. Droplet-based microfluidics provides means to quantitatively explore the dynamics of adsorption at small scales [33].

1.1 Aims of this work

In my thesis, I study the dynamics of surfactants at interfaces. I am using droplet-based microfluidics to perform a complete analysis of the adsorption kinetics of a surfactant. In microfluidics, perfluoropolyether (PFPE) with hydrophilic headgroups (e. g. carbohydrate, crown ether, polyethylene glycol (PEG) etc.) are often used as surfactants in combination with a fluorous solvent [7,42]. To determine the absorption kinetics, I use the carboxylic acid of a perfluoroether (Krytox) and monitor the transfer of protons across the interface using the pH change of the aqueous droplets produced on chip. I combine these
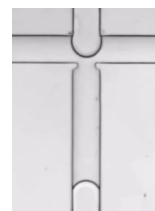
measurements with coalescence experiments to obtain the timescale and the coverage required for interfacial stabilisation. I unite these information to obtain a combined model of the adsorption kinetics of surfactants and the transport of molecules across interfaces. For biotechnological applications, pH changes due to surfactant adsorption could be detrimental to biochemical processes occurring in the droplet. Therefore, non-ionic surfactants are most promising for the use in droplet-based microfluidics, e. g. tri-block copolymers (e. g. PFPE-PEG-PFPE)[7]. These surfactants are often synthesised from the aminoterminated PEG and the PFPE carboxylic acid. The purity of the synthesised product is of great importance as small impurities of the acid lead to the exchange of solutes from the aqueous phase towards the continuous phase[28] and a change of pH of the emulsion droplets as observed in the adsorption studies in this work. Therefore, I improve the surfactant synthesis to circumvent these issues, while characterising the purity of the synthesised products using bulk methods, such as infrared spectroscopy, partitioning experiments and nuclear magnetic resonance spectroscopy.

To obtain information on the interactions between the surfactants at the droplet interface and the continuous phase, I analyse the surfactant properties in a minimal system showing self-propulsion.

In the following chapter (2), I explain the properties of emulsions and surfactants. I illustrate the adsorption behaviour of surfactants to interfaces including interfacial tension methods for the determination of the surfactant coverage, the critical micellar concentration and the adsorption kinetics. Afterwards, I introduce microfluidics as a tool for droplet manipulation. In Chapter 3, I describe the experimental methods and techniques, which I use to obtain the kinetics of surfactant adsorption to interfaces, the transfer of molecules across interfaces, information on the stabilisation of interfaces and criteria for the surfactant synthesis. I analyse the results in Chapter 4. In Chapter 5, I describe the follow-up experiments dealing with alternative adsorption measurements, the role of adsorption in self-propulsion and the stabilisation of emulsion droplets to perform particle synthesis and ice nucleation experiments in droplets. I discuss and conclude in Chapter 6 and 7, respectively. Through these studies, I aim at obtaining a consistent picture of the surfactant dynamics at droplet interfaces.

Thanks to the financial support from the IMPRS-PBCS program from the GGNB doctoral school and from the ERC (FP7/2007-2013 /ERC Grant agreement 306385–SofI), I had the chance and freedom to initiate collaborations on particle synthesis and ice nucleation in emulsion droplets, additionally to the work within the groups of Jean-Christophe Baret.
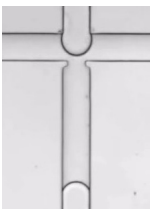
Chapter 2

Theoretical Background

Parts of this chapter are published in P. Gruner, B. Riechers *et al.*[8] and B. Riechers *et al.*[43] (in preparation 2015).

2.1 Emulsions

An emulsion is a liquid phase dispersed into a second liquid phase confined by interfaces in a metastable state[4,24]. An emulsion is obtained upon shearing, spraying or stirring of two immiscible liquids[4,11]. Direct emulsions are made of oil droplets in an aqueous phase (oil in water, O/W) while for inverse emulsions, the two phases are interchanged (water in oil, W/O). Additionally, double or multiple emulsions consist of small droplets of the continuous phase (or a third phase) dispersed in the emulsion droplets[4] (Fig. 2.1). The interfaces of emulsions can be stabilised using surface active agents (surfactants, Sec. 2.2) which are either small molecules, macromolecules (such as proteins[44] or polymer[45]) or even particles[2,7,46,47]. In the special case of solid particles stabilising emulsions (e. g. colloidal silica[48]), the term Pickering emulsions is used[47].

Emulsions are metastable dispersions of one (or more) immiscible phase into another[24]. The immiscibility of these phases is due to the differences of the intermolecular interactions between molecules from the same phase and the second phase[2,8,49,50]. This difference results in an enthalpy of mixing counteracting the entropy of mixing and leads

Emulsion	Double Emulsion	Multiple Emulsion
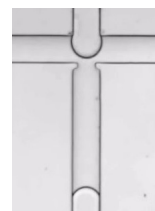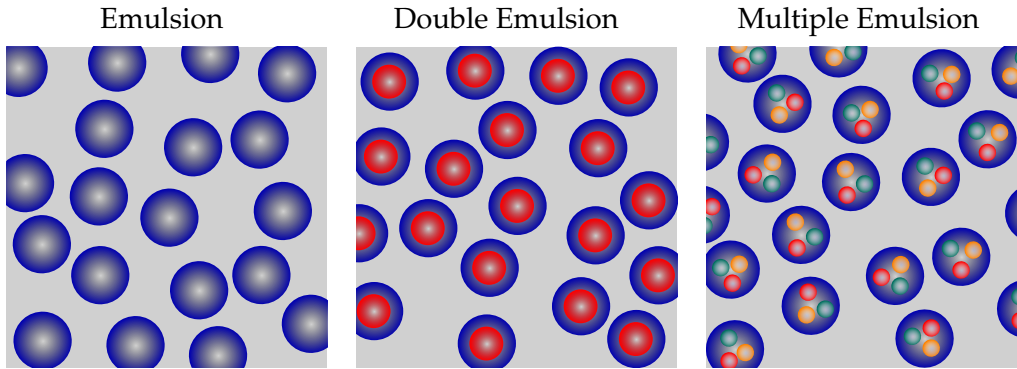
Figure 2.1: Different types of monodisperse emulsions: simple, double and multiple emulsion. The different colours represent the different phases.

to phase separation at below a critical temperature. The presence of an interface between the two phases requires an interfacial free energy G_{int} to create this interface with the area σ at constant temperature T, pressure P and number of particles n. The physico-chemical description of the two phases is then characterised macroscopically by the interfacial tension $\gamma = \partial G_{int}/\partial \sigma \mid_{T,P,n}$ [2,24]. If two emulsion droplets with the same size coalesce, the free energy of the coalesced droplet is about 20% ($1 - 2^{-1/3}$, Fig. 2.2) smaller than that of the two initial droplets due to the change in surface to volume ratio. Thus, emulsions age with time towards the state of minimal energy where the two phases are separated by a minimal surface (in the absence of gravity a large droplet). Several ageing processes coexist such as coalescence (merging of two droplets) [4,5,7,28], Ostwald ripening [4,5,7,29], phase partitioning [7], flocculation [4], gravitational separation [24] and exchange of molecules between neighbouring droplets due to bilayer formation between them [51].

Ostwald ripening is an equilibration process occurring because of the differences in Laplace pressures in different droplets. The pressure equilibrates because of the finite solubility of the dispersed phase inside the continuous phase [5,7]. Therefore, large droplets (low pressure) grow at the expanse of smaller droplets (high pressure). This mechanism leads to a polydispersity of the emulsion [7,52]. This coarsening can be reduced upon the addition of compounds, which are completely insoluble inside the continuous phase such as salts [53]. The osmotic pressure due to the salt will counterbalance the Laplace pressure effect.

The mechanism of Ostwald ripening can be generalised to the equilibration of the chemical potential of all species. The equilibration is mediated by phase partitioning between both phases. The partitioning coefficient is the ratio of the equilibrium solubility of the
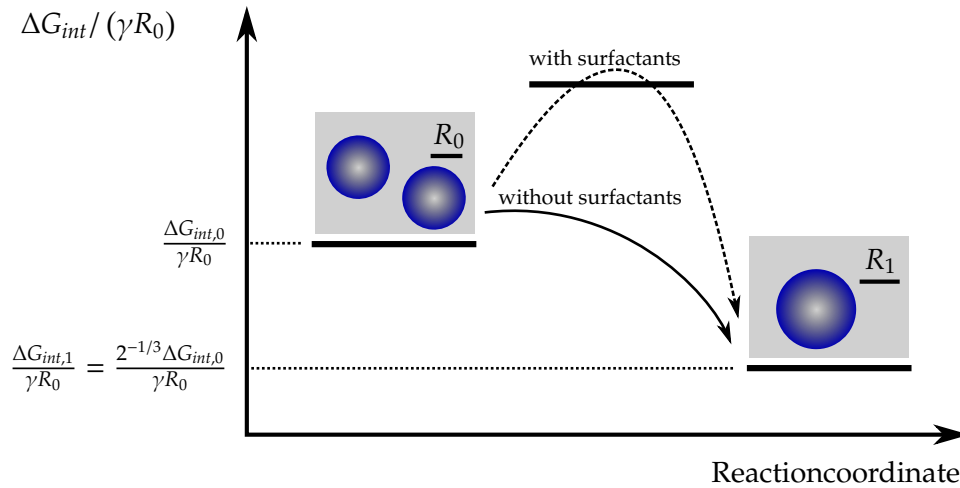
Figure 2.2: If two droplets with the same radius R_0 coalesce, they form a droplet with radius $R_1 = 2^{1/3}R_0$ due to volume conservation. This leads to a change in interfacial free energy from $\Delta G_{int,0} = 2\gamma\Delta\sigma_0$ to $\Delta G_{int,1} = \gamma\Delta\sigma_1$ with $\sigma = 4\pi R^2$. Thus the interfacial free energy decreases from $\Delta G_{int,0}$ to $\Delta G_{int,1} = 2^{-1/3}\Delta G_{int,0}$ (flash with continuous line). Surfactants at the interface create an energy barrier (dashed flash, Section 2.2).

solute in the continuous phase and in the dispersed phase, $K = c_{eq,cont}/c_{eq,disp}$[54]. Phase partitioning occurs when molecules are either soluble in both phases or are introduced into (reverse) micelles (Sec. 2.2)[25]. The permeability of molecules $P = KD/d_{mem}$ through a permeable membrane (such as the interface) depends on the partitioning coefficient K, the diffusion coefficient D, and the thickness of the membrane d_{mem}[54].

The control over these ageing processes is of great relevance for the use of emulsions in industry[7]. Produced creams and homogenised milk, for example, have to be stable over time and should not undergo coarsening. Even more challenging is the use of droplets as single microreactors in biotechnological applications, where partitioning, exchange and Ostwald ripening lead to mixing of components of droplets[8,18,25,55,56]. Thus, the efficient use of droplets as microreactors depends on the timescales of the ageing mechanisms in comparison to the timescale of the experiment considered[28]. Stabilisation against ageing such as coalescence, rupture, exchange and loss of molecules is therefore critical to enhance the lifetime of the emulsion[4,5,7,19,28]. Both, the driving force decreases and the energy barrier increases upon the use of surfactants. In some cases, surfactants even lead to an exergonic formation of the dispersion (microemulsion) meaning the change in the reaction Gibbs free energy is negative[24]. Thus, surfactants play a crucial role in these ageing processes[7,8,25,29] and I will introduce their properties and interactions in the following section.
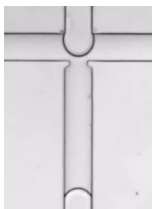
2.2 Surfactants and interfaces

As metastable systems (Fig. 2.2, Section 2.1), emulsions require kinetic stabilisation against ageing[24]. Stabilisation of an emulsion with given droplet sizes can be achieved thermodynamically by lowering the free energy through a decrease of interfacial tension (Sec. 2.1) or kinetically by introducing an activation barrier for the ageing process (Fig. 2.2)[2,27]. The properties of surfactants play a crucial role on both mechanisms. The term 'surfactant' is a composite of the words surface-active agent meaning that the molecules act on the surface or interface of a system[7]. Typical surfactants possess hydrophilic headgroups and hydrophobic tails. They adsorb to interfaces through their amphiphilic character and lower the interfacial tension[1,2]. Additionally, they delay coalescence of emulsion droplets through steric repulsion as well as through the coupling with hydrodynamic flows[7,27]. The hydrodynamic flows (Marangoni effect) between approaching droplets delay the drainage time between the emulsion droplets, and thus, increase the kinetic stabilisation of the emulsion[27] (see Sec. 2.5). Finding a suitable surfactant for an emulsion application is chemically challenging as emulsion stability depends on a large variety of factors, such as the interactions of the hydrophilic and hydrophobic groups with each other and their interactions with the adjacent phases[2,18].

2.2.1 Equilibrium coverage of surfactants

A quantitative approach for the surfactant adsorption of a monolayer to interfaces or surfaces is given by the Gibbs adsorption equation (Eq. 2.1) derived by describing the Gibbs free energy including the surface excess quantities of the system[1,2,57]. The following approach holds for surfaces as well as for interfaces, the surfactant being only present (soluble) in one of the phases. The Gibbs Adsorption Equation is given by

$$d\gamma = -\sum_i \Gamma_i \, d\mu_i \tag{2.1}$$

with the interfacial tension γ, the interfacial excess concentration Γ_i, and the chemical potential μ_i, of each component i. In equilibrium (*eq*), the chemical potential depends on the activity $a_i = x_i \cdot f_i$, with the activity coefficient f_i, and the mole fraction x_i:

$$d\mu_i = RTd \ln a_i \tag{2.2}$$

with R as the ideal gas constant and T as the absolute temperature. In the case of the adsorption of surfactants to the interface, only two species are present, namely the surfactant and the solvent(s)[1,2,57]. The Gibbs convention states, that the major component (the solvent(s)) has an interfacial excess concentration of zero. Thus, only the excess concentration of the surfactant (subscript s) Γ_{eq} differs from zero[1,2,57] leading to

$$-\frac{\mathrm{d}\gamma_{eq}}{RT} = \Gamma_{eq}\,\mathrm{d}\ln a_{eq,s}\,. \tag{2.3}$$

In dilute solutions and for non-ionic surfactants, its activity equals the concentration of the surfactant in solution C, resulting in[1,2,40,57]

$$\Gamma_{eq} = -\frac{1}{RT}\cdot\frac{\mathrm{d}\gamma_{eq}}{\mathrm{d}\ln C}\,. \tag{2.4}$$

For surface active species, the interfacial excess concentration equals the interfacial coverage without significant error[2,57,58]. Therefore, the equilibrium interfacial coverage is obtained from equilibrium interfacial tension measurements of a set of concentrations of surfactant solutions (Fig. 2.3). Equation 2.4 only holds for dilute surfactant concentrations where the interactions between the surfactant molecules are ideal and thus the activity coefficient is close to unity. Above a critical concentration (called the critical micellar concentration, CMC, Sec. 2.2.2), the linear relation between the equilibrium interfacial tension with $\ln C$ deviates (Fig. 2.3 (a)) due to the fact that the surfactant monomers (non-aggregated surfactant molecules) cluster to micelles[1,2] (Sec. 2.2.2).

The maximum interfacial coverage is obtained from the slope $-RT\Gamma_{\infty}$ of the change of equilibrium interfacial tension with $\ln C$ (see Sec. 2.4.2, Eq. 2.22). The change of the interfacial tension with the concentration of surfactant (Eq. 2.4) is also influenced by the size and chemical structure of both the headgroup and the tail of the surfactant and their interactions with the adjacent phases. The interactions between the headgroups are of great relevance as well[2] as charged headgroups for example do not form a dense packing on a pure water interface due to electrostatic repulsion between the headgropus. The charges can be screened by adding counter ions of the opposite charge to the aqueous phase leading to a denser packing of the surfactant molecules at the interface, and thus, a lower interfacial tension[4].
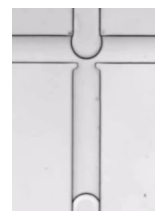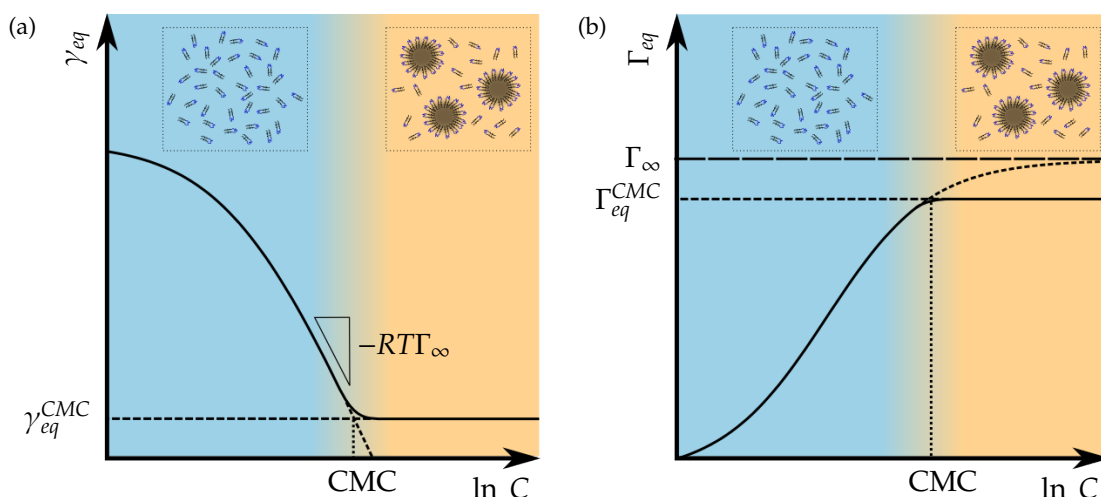
Figure 2.3: (a) Equilibrium interfacial tension and (b) equilibrium coverage versus concentration of surfactant for the determination of the CMC (modified from Barnes *et al.* [1]). At low surfactant concentrations only monomers exist, whereas micelles (Fig. 2.4) coexist with monomers at concentrations above the CMC. The maximum interfacial coverage Γ_∞ is obtained from the slope in (a) (Sec. 2.4.2, Eq. 2.22) and it is higher than the equilibrium interfacial coverage at the CMC is Γ_{eq}^{CMC} (b).

2.2.2 Critical micellar concentration

In the last section, I have described the surfactant adsorption of a monolayer to an interface considering the presence of surfactant monomers in solution. In this section, I will describe the formation of surfactant clusters due to their amphiphilic nature. When the concentration of surfactant is increased to above the CMC, they form clusters to minimise their free energy[2,57,59]. These structures are called micelles and greatly influence the properties of the surfactant solution such as the capacity to solubilise water-insoluble compounds in an aqueous surfactant solution or water-soluble molecules for non-aqueous solutions[2]. Surfactants in an aqueous solvent can form spherical micelles with small aggregation numbers (<100 surfactant molecules form a micelle)[2], large micelles with different shapes (elongated, disk-like) or vesicles which consist of bilayers of surfactant. In all these structures, the hydrophobic tails cluster together and the hydrophylic headgroups point towards the aqueous phase (Fig. 2.4). In non-aqueous media, the organisation is inverted, thus forming reverse or inverse micelles and vesicles (Fig. 2.5)[2,62–64]. Micelles always coexist with monomers above the CMC, whereas its value depends on the solvent and surfactant mixture[2,60]. However, not all surfactants show a CMC in aqueous solutions, e. g. bile salts[60]. Whether the existence of aggregates in solution is energetically more favourable than the existence of monomers, depends
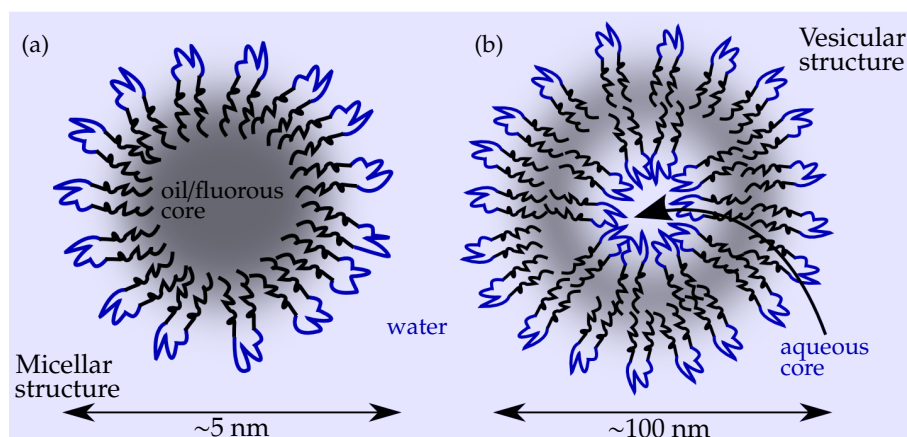
Figure 2.4: Clusters of surfactants in aqueous media and their sizes[60] (figure adjusted from P. Gruner, B. Riechers *et al.*[61]).
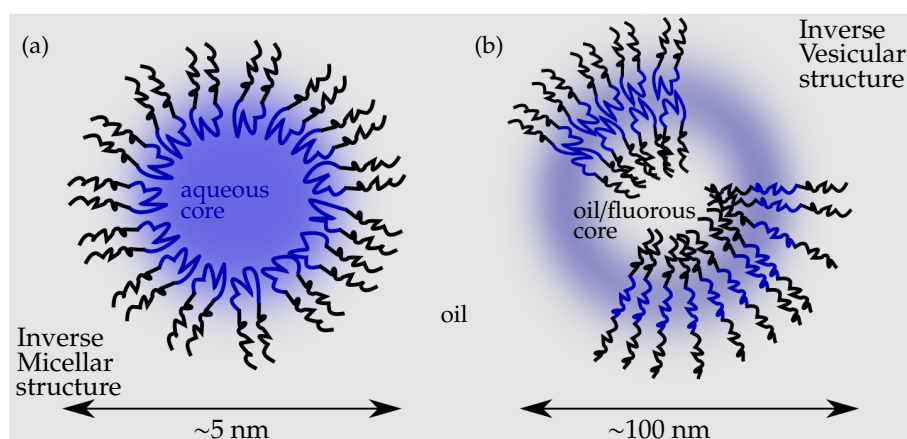
Figure 2.5: Clusters of surfactants in non-aqueous media and their sizes for fluorous media (micelles[65], vesicles[28,61], figure adjusted from P. Gruner, B. Riechers *et al.*[61]).

on the interactions between the surfactant and the solvent[2,62,63]. The different interactions in non-aqueous media lead to mostly smaller aggregation numbers (around 10 to 30)[62,63,66] than the comparable micelles (<100)[2] as they posses weaker interactions. Mostly, non-aqueous solutions show only dipole-dipole interactions, whereas stronger interactions due to hydrogen bonds exist in aqueous media[63]. In non-aqueous systems, the aggregation numbers often gradually increase upon addition of further surfactant or of water leading to larger clusters without a sharp and sudden change in the cluster size[2,62]. Thus, for many non-aqueous solvents, a CMC does not exist[2,62].

For the determination of the CMC, many different methods are described in literature. Firstly, the CMC can be determined indirectly using interfacial tension measurements at different total concentrations (of the surfactant monomers). Upon increasing the surfac-

tant concentration in solution, the equilibrium interfacial tension (usually) decreases[2]. For concentrations above the CMC, the interfacial tension does not decrease further (Fig. 2.3 (a)) and the monomer concentration stays virtually constant[1,2,60]. Secondly, micelles in solution can be measured directly upon changing the concentration of the surfactant, e. g. using light scattering (size of clusters) or nuclear magnetic resonance spectroscopy (NMR, diffusion measurements)[60].
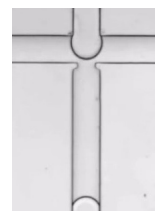
2.3 Measurement of interfacial tension

The interfacial tension of an interface between two bulk fluids covered with a surfactant can be measured using different methods. The first precise method was introduced by Du Nouy[60,67] which then led to the **ring tensiometer**[68] (Fig. 2.6(a)). It is based on the measurement of a force to detach a ring from the liquid-air interface. This force is due to the interfacial tension of the liquid and the weight of the ring itself. Subtracting the effect of the weight, the interfacial tension is given by $\gamma = F_{int}/(2\,l)$ with the force F_{int} arising solely from the interfacial tension acting on the entire circumference of the ring, l[68] (more accurately, $2\,l$ being the sum of the inner and outer circumference of the ring[6]). Later, it was shown that a correction factor for the calculation of the interfacial tension is needed to account for the thickness of the wire. Experimental inaccuracy can arise due to *i. e.* the ring hanging not horizontally, a too small interfacial area and imperfect illumination[6,69,70].

Another very common technique measuring the force exhibited by the interfacial tension, is the **Wilhelmy-plate method**[1,6,71]. Here, the plate is positioned at the interface and the interface exhibits a force onto the plate (Fig. 2.6(b)). It is assumed, that one of the two phases completely wets the plate (contact angle, $\theta = 0$, Fig. 2.6(b)). The contact angle in equilibrium is related to the interfacial and surface tensions of the phase boundaries intersecting at the three phase contact line. For a wetting surface this contact angle is $0°$, for a completely non-wetting surface $180°$[1,6]. The force due to the interfacial tension, F_{int} of the plate downwards is again given by $F_{int} = \gamma\,2\,l$, with $2\,l$ as the circumference[1,6].
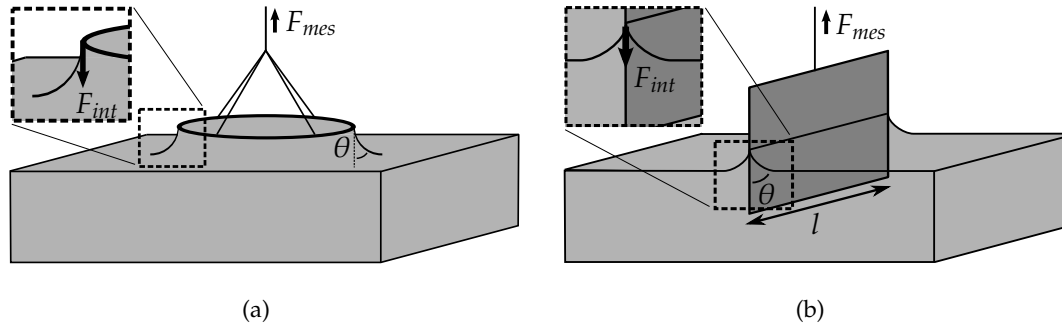
Figure 2.6: Setups to measure the interfacial tension using the force exerted onto a ring (a) or a plate (b) with the contact angle θ, the measured force F_{mes} (gravitational force is subtracted) which counteracts the force F_{int} exhibited by the interfacial tension. (a) Sketch of the ring tensiometer. A ring with a circumference of $2\,l$ is dipped into a solution (adjusted from Du Nouy[68]). (b) Sketch of the Wilhelmy plate dipped into a solution with the length of the plate l (adjusted from Butt *et al.*[6]).

In early experiments, the interfacial tension of drops was obtained using the size of **falling drops** from the tip of a fine capillary tube[72–74]. In these experiments, the interfacial tension counteracts the gravitational force until the growing drop detaches. A scaling law relates the size of the falling drop to the radius of the tip R_{tip} leading to the bond number (Chapter 3 in[75] and[71])

$$\text{Bo} = g\Delta\rho R_{tip}^2/\gamma \,, \tag{2.5}$$

where g is the acceleration of gravity and $\Delta\rho = \rho_i - \rho_o$ the density mismatch between the inner fluid i and the outer fluid o. For known densities ρ_i and ρ_o, and given the acceleration of gravity g, one can compute the magnitude of interfacial tension from the Bond number. During a falling drop experiment, the interfacial area is changing and convection takes place at the interface. These two effects are both disadvantageous for the measurement of dynamic interfacial tensions.

To overcome this, the **sessile bubble** or **pendant drop method** (Chapter 3, 12 in[75] and[6,71,76]) was developed to measure the interfacial tension of a static fluid-fluid interface from a balance of interfacial and gravitational forces. In both techniques, the contour of the hanging drop or the sessile bubble (or drop) is detected (Fig. 2.7) and fitted by the Young-Laplace equation (Eq. 2.6). The free fit parameter is the bond number (Eq. 2.5). The Young-Laplace equation relates the mean curvature and the tension γ of an interface between two fluid phases to the pressure difference $\Delta P = P_i - P_o$ of the two adjacent phases (Chapter 3 in Miller et al.[75]). In mechanical equilibrium, the pressure difference
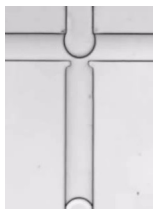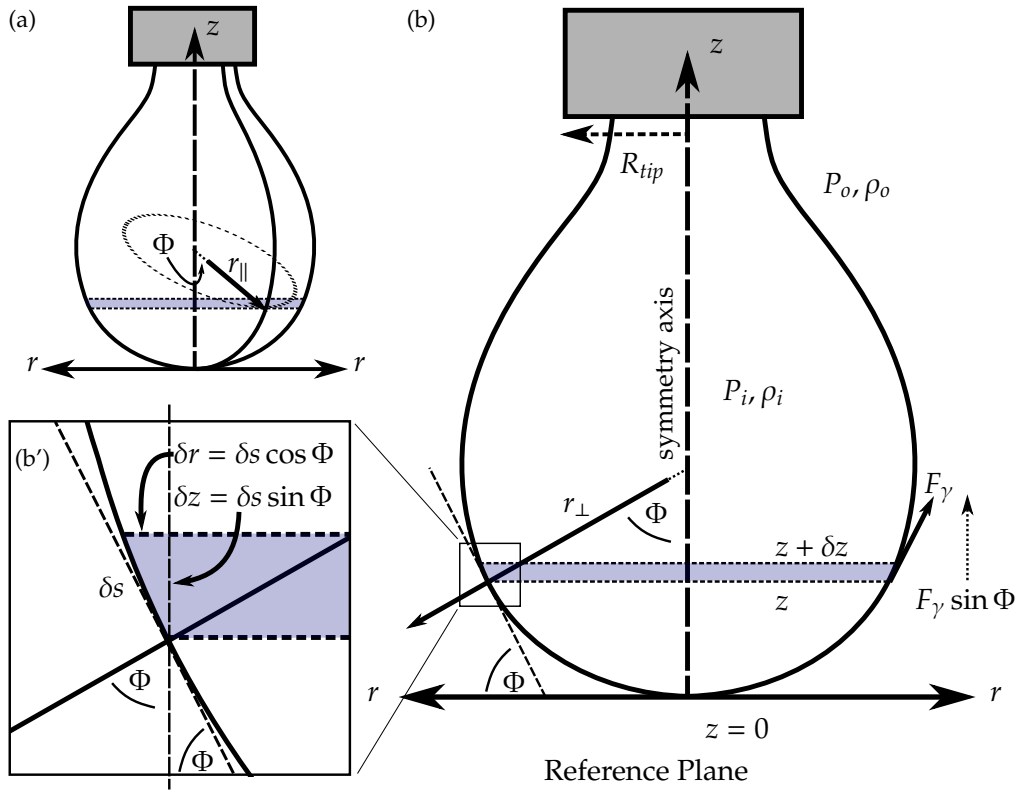
Figure 2.7: The pendant drop method with all important parameters to obtain the interfacial tension using the Young-Laplace Equation (adjusted from Barnes et al.[1] and Miller et al. Chapter 3, 12[75]).

ΔP is related to the two principal radii of curvature, $c_\perp$ and $c_\parallel$, through the law of Young and Laplace:

$$\Delta P = \gamma \left(c_\perp + c_\parallel \right) \tag{2.6}$$

with the two radii $r_\perp = 1/c_\perp$ and $r_\parallel = 1/c_\parallel$ (Fig. 2.7).

In the absence of gravity or if the densities of the two bulk fluids are identical, the pressure difference ΔP does not depend on the position on the interface. Provided that the interfacial tension is the same in all points of the interface, the interface of the pendant drop must be a surface of constant mean curvature[1].

The derivation of the Young-Laplace law (Eq. 2.6) and the equations governing the shape of a pendant drop is given in Chapter 3 and 12 of Miller et al.[75]. It is derived considering all force components acting on a thin slice of the droplet, which is cut out by two parallel planes perpendicular to the symmetry axis (Fig. 2.7(b)) and at z and at $z + \delta z$ over the reference plane. Due to the cylindrical symmetry of the pendant drop with respect

---

[1]Besides the catenoid and the plane, the surface of a sphere is the only non-periodic cylindrically symmetric surface of constant mean curvature.

to the direction of gravity, only the z-components of the forces need to be considered (forces projected onto the z-axis). Thus, this method is only applicable for cylindrically symmetric droplets. For later convenience, the droplet shape is described by the local angle $\phi(s)$ between the local tangent and the reference plane, the distance $r(s)$ to the z-axis, or the coordinate $z(s)$ as a function of the arclength s measured along the interfacial contour. The tip of the droplet $s = 0$ corresponds to $\phi = 0$, $r = 0$ and $z = 0$. As a note, these three functions are not independent from each other, thus, only one of them is sufficient to describe the profile.

In mechanical equilibrium (Chapter 3, 12 in[75] and[1]), the interfacial force δF_γ, the gravity δF_g, and the pressure contributions δF_p to the thin slice balance each other. From geometrical considerations, $dz/ds = \sin\phi$ and $dr/ds = \cos\phi$ (Fig. 2.7(b')). Thus, the interfacial tension γ exerts a force

$$
\begin{aligned}
\delta F_\gamma &= 2\pi\gamma(r\sin\phi)\big|_{z=z_0+\delta z} - 2\pi\gamma(r\sin\phi)\big|_{z=z_0} \\
&= 2\pi\gamma\left(\sin\phi\cos\phi + r\frac{d\phi}{ds}\cos\phi\right)\bigg|_{z=z_0}\delta s + O(\delta s^2)
\end{aligned}
\tag{2.7}
$$

on the slice, while the pressure P_i in the droplet phase amounts to a total force of

$$
\begin{aligned}
\delta F_{P_i} &= -\pi\left(P_i r^2\right)\big|_{z=z_0+\delta z} + \pi\left(P_i r^2\right)\big|_{z=z_0} \\
&= -\pi\left(2r P_i\cos\phi + r^2\frac{dP_i}{dz}\sin\phi\right)\bigg|_{z=z_0}\delta s + O(\delta s^2).
\end{aligned}
\tag{2.8}
$$

The force acting on the fluid-fluid interface due to the pressure of the ambient phase P_o is given by

$$
\delta F_{P_o} = 2\pi r P_o\cos\phi\,\delta s + O(\delta s^2).
\tag{2.9}
$$

The gravitational force on the thin slice simply reads

$$
\delta F_g = -\pi\rho_i g r^2\sin\phi\,\delta s + O(\delta s^2).
\tag{2.10}
$$

Because of the hydrostatic contribution to the pressure in the bulk fluids, the pressure $dP_i/dz = -\rho_i g$ depends on the density of the liquid ρ_i, which leads to the condition

$$
\begin{aligned}
\delta F_\gamma + \delta F_{P_o} + \delta F_{P_i} + \delta F_g &= \\
2\pi r\cos\phi\left(\gamma\frac{d\phi}{ds} + \gamma\frac{\sin\phi}{r} - \Delta P\right) &= 0,
\end{aligned}
\tag{2.11}
$$

for the sum of forces in mechanical equilibrium. Since $r\cos\phi \neq 0$ for a generic point on the droplet contour in equilibrium, it can be concluded that

$$
\gamma\left(\frac{d\phi}{ds} + \frac{\sin\phi}{r}\right) = \Delta P
\tag{2.12}
$$

holds in every point of the droplet contour between the apex $z = 0$ and the tip of the pipette. From the sketch in Fig. 2.7, the meridional curvature is given by $c_\perp = 1/r_\perp = d\phi/ds$ and the normal curvature into the direction of a parallel is $c_\parallel = 1/r_\parallel = \sin\phi/r$ (Fig. 2.7). Condition (2.12) is the Young-Laplace law (2.6) for cylindrically symmetric surfaces.

The pressure difference ΔP depends on the height z above the reference plain at $z = 0$ passing through the apex of the droplet:

$$\Delta P = \Delta P_0 - g\,\Delta\rho\,z \;. \tag{2.13}$$

The Laplace pressure ΔP_0 at the apex $z = 0$ (Chapter 12 in[75]) is related to the curvature $1/b = c_\parallel = c_\perp$ of the contour at the apex through

$$\Delta P_0 = \frac{2\gamma}{b} \;. \tag{2.14}$$

Employing the radius of the pipette R_{tip} as a length scale, γ/R_{tip} as a pressure scale, and respecting Equations (2.13), (2.14), and the definition (2.5), the Young-Laplace law (2.12) in the dimensionless form can be rewritten as

$$\frac{d\phi}{d\tilde{s}} = \frac{2}{\tilde{b}} - \frac{\sin\phi}{\tilde{r}} - \tilde{z}\,\mathsf{Bo} \;, \tag{2.15}$$

where $\tilde{b} = b/R_{tip}$ denotes the dimensionless radius at the apex, $\tilde{z} = z/R_{tip}$ and $\tilde{r} = r/R_{tip}$ the dimensionless cylindrical coordinates, and $\tilde{s} = s/R_{tip}$ the dimensionless arclength on the contour. The definition of $\tilde{r}$, $\tilde{z}$, and ϕ lead to additional conditions

$$\frac{d\tilde{r}}{d\tilde{s}} = \cos\phi \tag{2.16}$$

and

$$\frac{d\tilde{z}}{d\tilde{s}} = \sin\phi \;. \tag{2.17}$$

With the boundary conditions, $\tilde{r}(0) = \tilde{z}(0) = \phi(0) = 0$, and the given meridional curvature $d\phi/d\tilde{s} = 1/\tilde{b}$ at the droplet apex, one can numerically solve the set of first order differential equations (2.15-2.17, Chapter 12 in[75]). The differences between the detected contour in the experiment and numerically computed droplet contours according to Equations 2.15-2.17 as a function of the parameter $\tilde{b}$ and Bo are minimized. The interfacial tension γ is obtained from the optimised Bond number and the known density mismatch $\Delta\rho$ using Equation 2.5[75].

With these methods, the interfacial tension of pure liquids or surfactant solutions can be measured including its change upon time. From such data, the value of the CMC and the interfacial coverage can be obtained (Sec. 2.2.1). Additionally, these data give rise to information on the adsorption kinetics (see the following Sec. 2.4).

2.4 Modelling the kinetics of adsorption

Mechanisms of adsorption kinetics are a highly debated field of scientific research with the first quantitative experiments at the beginning of the 20th century[77,78]. Many different experimental and theoretical studies were performed on the adsorption mechanism of ionic and non-ionic surfactants to fluid-fluid interfaces[33–39,79]. Depending on the properties of the surfactant in relation to the two phases, mainly two limiting mechanisms of the adsorption rate were described. Many different models try to explain adsorption kinetics either by a diffusion-only mechanism or by a mixed diffusion-kinetic controlled adsorption with the implementation of an adsorption barrier[33–40]. The effect of adsorption and desorption barriers in surfactant solutions is far from being understood as contradictory data are published in the literature[40]. Adsorption barriers are difficult to identify as the kinetics often differ only slightly from the diffusion limited regime, apart from the barrier due to electrostatic repulsion. Modelling the complete adsorption kinetics involves many adjustable parameters[40]. Recently, there has been an approach to overcome these difficulties by predicting interfacial tension data using experimental data as inputs[38]. Using this method, it becomes unnecessary to measure the whole interfacial tension data in the complete concentration range using standard techniques like the pendant drop or the Wilhelmy plate method. The disadvantages of these two techniques are the long equilibration times and the need for large amounts of surfactants and solvents[37,40,69,80] (e. g. 30 mL of both adjacent phases per measurement). Depending on the concentration of surfactant, a measurement of one single dynamic interfacial tension curve at a liquid-liquid interface takes more than a week.

The adsorption kinetics of a surfactant to the interface describe the coverage of an interface at given surfactant concentrations from time zero to the time where the equilibrium of the surfactant coverage with the bulk phases is reached (Fig. 2.8). The interfacial tension at time zero is given by the interfacial tension between the pure liquids without any
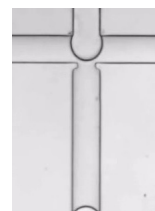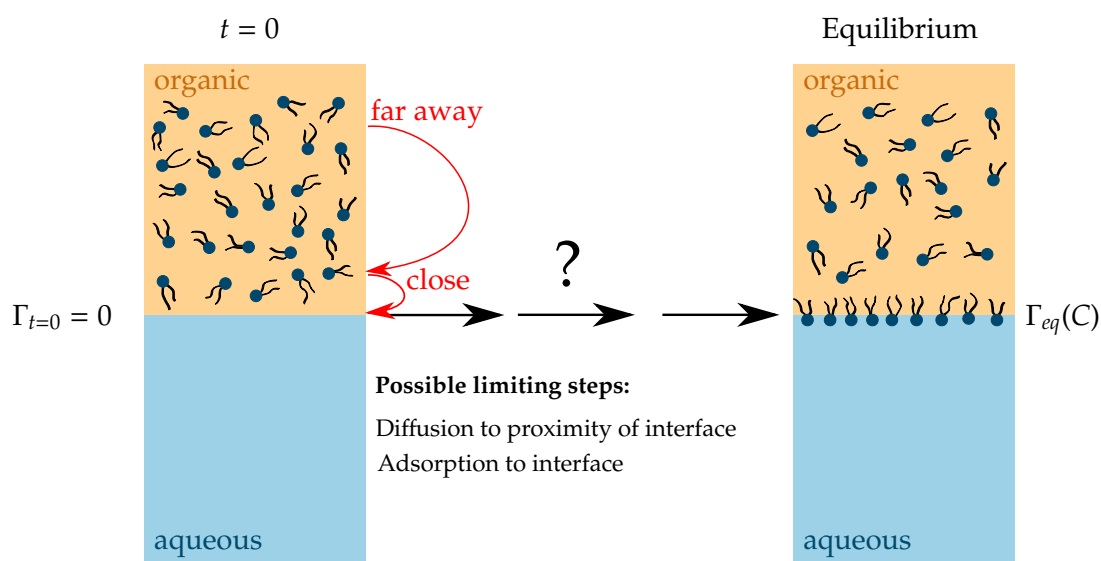
Figure 2.8: The adsorption process of surfactants soluble in one of the two phases including the two limiting cases: diffusion or kinetic.

surfactants leading to a surfactant coverage of $\Gamma_{t=0} = 0$. The relation of the equilibrium surfactant coverage Γ_{eq} with the interfacial tension is discussed in Section 2.2.1.

In the following section, the kinetics of surfactant adsorption from an initially empty interface to an interface with equilibrium coverage are described. Firstly, these kinetics depend on the timescale of the adsorption process of molecules in close proximity to the interface. It describes how fast the layer close to the interface is depleted of surfactant molecules. Secondly, the timescale of diffusion of molecules is set by the average time it takes for molecules to diffuse towards this depleted layer close to the interface (Fig. 2.8)[41,81]. Thus, two possible governing mechanisms exist: the diffusion and the kinetic limited adsorption[41,81,82]. I will now describe these two mechanisms in detail leading to different scalings of the adsorption rate with time and important crossovers (see Fig. 2.9).

For these considerations, the surfactant at a concentration C is only soluble in one of the phases. The interface is created at time $t = 0$ with a surfactant coverage of $\Gamma_{t=0} = 0$, before the surfactant coverage increases with time and reaches the equilibrium coverage $\Gamma_{eq}(C)$.
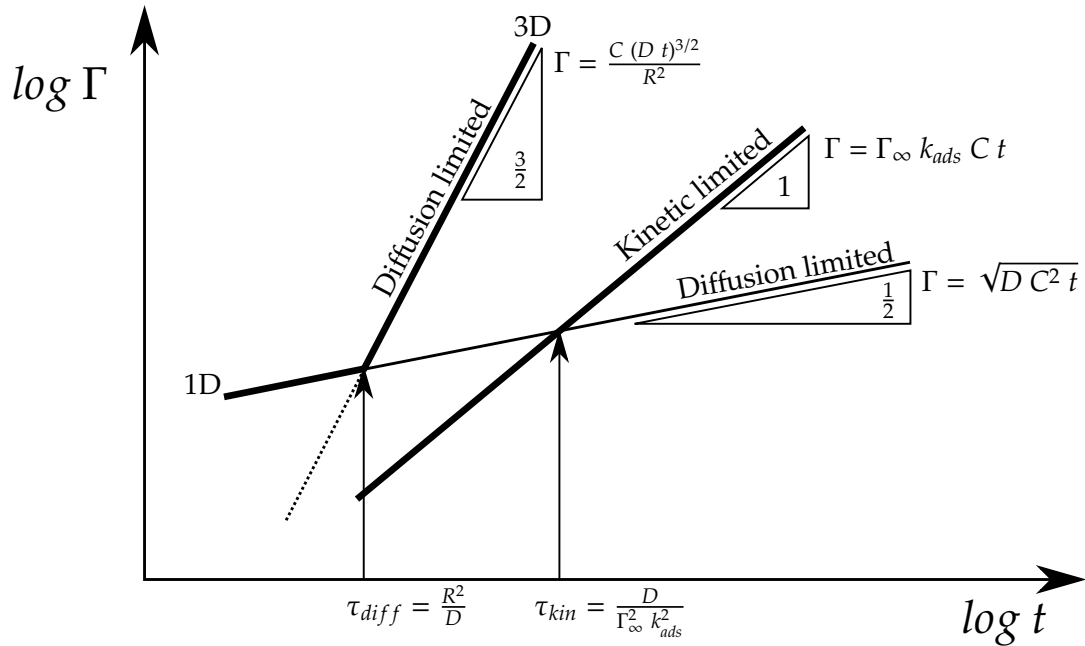
Figure 2.9: Scaling laws for the interfacial coverage if the diffusion (1D: flat interface, 3D: droplet or bubble interface) or the kinetic limited adsorption process is rate limiting.

2.4.1 Diffusion limited adsorption

The adsorption kinetics is diffusion limited when the timescale of diffusion is larger than that of the adsorption process itself. This is directly related to the Fickian diffusion and depends on the geometry of the interface[41,81]. The newly created (at t_0) interface is not covered by surfactants (Fig. 2.10(a)). At small times (at $t \to 0$), the layer close to the interface is depleted of surfactant molecules. Diffusion takes place (at t_{inter}) and leads to an equilibration of the surfactant concentration throughout the bulk (at t_{eq}). If the amount of surfactant initially in the bulk is much larger than the amount at the interface, the bulk concentration of the surfactant at equilibrium (at t_{eq}) is equal to the one at the initial contact of the interfaces (at t_0). The length or depth L of the layer where all molecules adsorb to a planar interface can be explained by considering the adsorption of molecules in a volume element dV to an element of the interface dA[41,81]. As the adsorption in the diffusion limited case is very fast, the amount of molecules adsorbed is always in equilibrium with the concentration of surfactant in the subphase. This coverage Γ_{1D} and the area dA describe the number of adsorbed molecules $\Gamma_{1D} dA$. This amount of molecules equals $C dV = CL dA$ as they were present in the volume dV before adsorption. Thus, the lengthscale follows $L = \Gamma_{1D}/C$. The time, which is required for the surfactant to adsorb
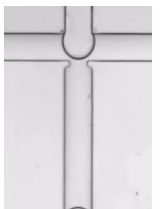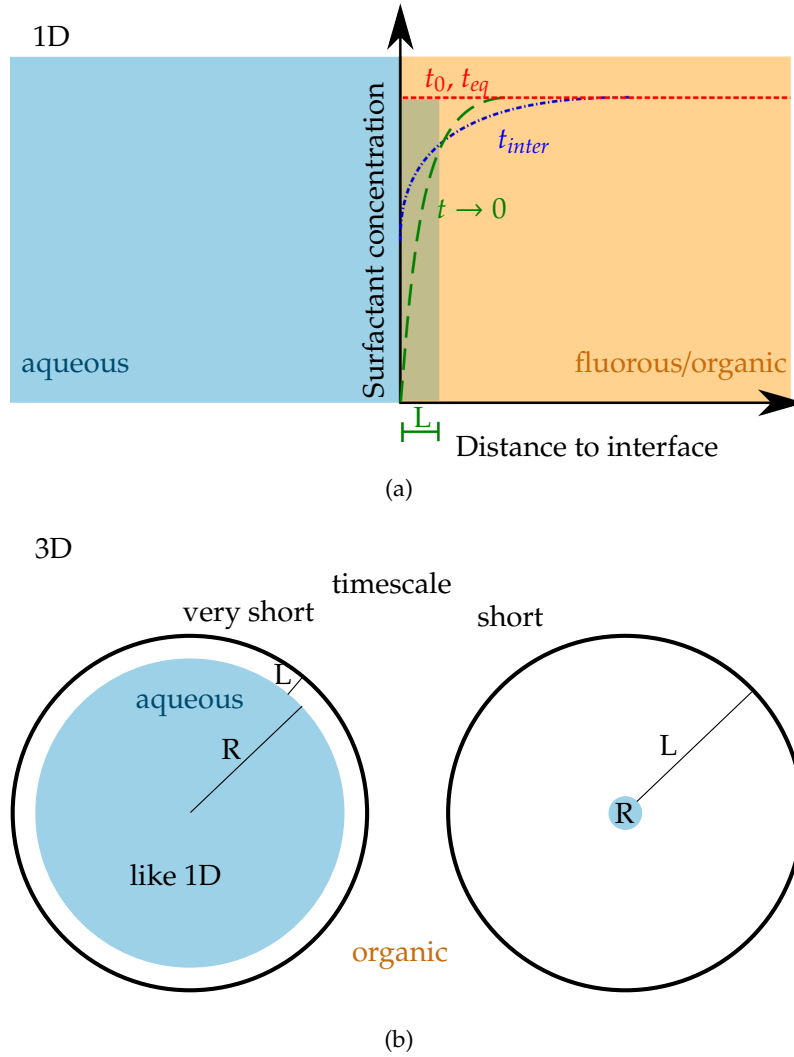
Figure 2.10: The representation of the diffusion limited regime for 1D (a) and 3D interface at different timescales (b) with the radius of the droplet, R, and the diffusion length, L.

from this length scale, is described by the Fickian first diffusion law with $\tau_{diff,1D} = L^2/D$, with the diffusion coefficient D. For dilute surfactant concentrations, the depth L is in the order of 10^{-1} m, for concentrations approaching the CMC, it is in the order of 10^{-5} to 10^{-3} m[41,81]. From these considerations, the surfactant coverage for a flat interface at early times scales with the square root of time (Fig. 2.9)[77,81,83]:

$$\Gamma_{1D}(t) = \sqrt{D\,C^2\,t}\,. \tag{2.18}$$

A 3D interface, namely a bubble or droplet (Fig. 2.10(b)), shows a different scaling law. In the case of a spherical droplet (or bubble), the above developed argument still holds for very small timescales where the curvature of the droplet is insignificantly small (Fig. 2.10(b)). At larger times, this curvature needs to be taken into account[41,81]. Using

geometrical arguments for the depleted volume, the interfacial coverage for the spherical case Γ_{3D} scales with a power of 3/2 with time (Fig. 2.9)[81]:

$$\Gamma_{3D}(t) = \frac{C\ (D\ t)^{3/2}}{R^2}\ .\tag{2.19}$$

The crossover between these two regimes occurs at a time $\tau_{diff} = R^2/D$ (Fig. 2.9)[41].

2.4.2 Kinetic limited adsorption

The second limiting case implies that diffusion is much faster than the adsorption of the surfactant molecules to the interface due to an adsorption barrier. Many different adsorption models are found in the literature. Apart from an adsorption barrier for non screened ionic surfactants due to electrostatic repulsion, other barriers are more difficult to identify as the rate of surfactant coverage often differs only slightly from the one of the diffusion limited regime[40].

In the following, I will only consider the Langmuir adsorption model as it is well understood and the most relevant for this work. It is a simple approach to describe the adsorption and desorption processes. For this approach, the following assumptions are relevant. The surface is considered as being divided into a regular plane lattice on which
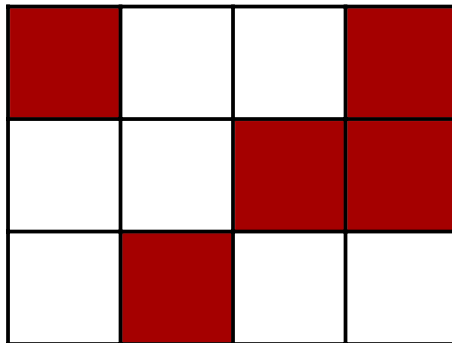
Figure 2.11: The Langmuir isotherm relates to a plane surface where all sites are equal and can hold maximum one molecule. Occupied (red) and unoccupied (white) sites do not interact with each other. Adsorption takes place on random sites.

all sites are equal (Fig. 2.11)[2,39,84]. Each site can hold maximum one adsorbed molecule. If all sites are occupied, the coverage is Γ_∞. The adsorbed molecules do not interact with the neighbouring sites and other adsorbed molecules[2,39,84]. This means that the adsorption of a molecule on one of the sites is independent of the presence of adsorbed
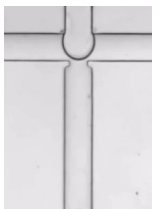
molecules on the neighbouring sites. Considering these assumptions, the rate of adsorption is directly proportional to the concentration of the surfactant inside the bulk solution C, the amount of free sites at the interface ($\Gamma_\infty - \Gamma$), and the adsorption constant k_{ads} (first part of Equation 2.20). The desorption depends on the occupied sites Γ and the desorption constant k_{des} (second part of Equation 2.20) [2,39,40,84].

$$\frac{\partial \Gamma}{\partial t} = k_{ads}C\Gamma_\infty \left(1 - \frac{\Gamma}{\Gamma_\infty}\right) - k_{des}\Gamma \qquad (2.20)$$

At equilibrium coverage Γ_{eq}, the coverage of the interface is in a steady-state ($\partial\Gamma/\partial t = 0$), resulting in the Langmuir isotherm [2,39,40,84]:

$$\Gamma_{eq} = \Gamma_\infty \left(\frac{\kappa C}{1 + \kappa C}\right) \qquad (2.21)$$

with $\kappa = k_{ads}/k_{des}$ (Appendix C.1). This equation holds for surfactant concentrations below the CMC [39]. Equating this relation with the dependency including the interfacial tension (Eq. 2.4) leads to [39] (Appendix A.1):

$$\gamma_{eq} = \gamma_0 - RT\Gamma_\infty ln\,(1 + \kappa C) \ . \qquad (2.22)$$

Upon fitting the equilibrium interfacial tension data versus the concentration lower then the CMC, the maximum interfacial coverage Γ_∞ is obtained (see also Fig. 2.3 (a)). At early stages, the desorption term can be neglected (right side of Equation 2.20) as the coverage is close to zero leading to an integrated form of Equation 2.20 where the surfactant coverage scales linearly with time (Fig. 2.9) [82]:

$$\Gamma(t) = k_{ads}Ct\Gamma_\infty \ . \qquad (2.23)$$

This is the upper boundary for interfacial coverage as desorption of surfactant molecules is not taken into account. Equating the change in surfactant coverage due to adsorption (Eq. 2.23) with the one due to diffusion (3D case, Eq. 2.19) leads to the crossover (Fig. 2.9) between the two regimes of $\tau_{kin} = D/\left(\Gamma_\infty^2 k_{ads}^2\right)$ [41]. The diffusion coefficient D varies slightly with the surfactant but can be estimated to be in the order of 5 x 10^{-10} m^2/s for nonpolymeric surfactants [41]. As long as $\tau_{kin} > \tau_{diff}$, the system is kinetic limited [41]. This holds for radii R smaller than the crossover radius $R^* = D/\left(k_{ads}\Gamma_\infty\right)$ which is in the order of 15 to 70 µm. The crossover timescale is of the order of 0.5 to 10 s [41].

Due to the wide use of emulsions, the understanding of the effects that occur when decreasing the size of droplets is of great relevance. It is important for the emerging field

of droplet-based microfluidics (e. g. pharmaceutical)[17]. The measurements of interfacial tensions with large volumes such as the Wilhelmy plate or the pendant drop method (Sec. 2.3) do not provide the same information on the kinetics as measurements at small length scales (in the range of tens of micrometer). In the case of small length scales, the adsorption kinetics are usually governed by the adsorption limited case.

The crossover radius depends on the diffusion coefficient, the maximum interfacial coverage and the adsorption constant. Many different methods exist for the determination of the diffusion coefficient such as NMR measurements or light scattering. The maximum interfacial coverage can be obtained using interfacial tension measurements. The adsorption rate constant is more challenging to obtain.

In my study, I use droplet-based microfluidic to obtain information on the kinetic limited adsorption of surfactants with the advantages of high throughput, small dimensions and in flow measurements.

2.5   Surfactant induced self-propulsion

The presence of surfactants at interfaces leads to additional phenomena, such as self-propulsion, which arise due to the interfaces being out of equilibrium. This movement of droplets can mimic locomotion of some organisms (called squirmers)[31]. Such a propulsion can lead to a macroscopic directed motion[85]. Self-propulsion is widespread as it is found in many different systems. Prominent examples are the bromination of monoolein at the interface of water in oil droplets[31], liquid crystals[86], microtubuli at interfaces[87], pure water droplets in a surfactant solution[30] and pH induced deprotonation of surfactants at the interface[88]. This motion has different origins, but they all include a reaction at the interface of the droplet and an interaction between the interface and the exterior of the droplet. The above named movement of pure water droplets is created by microemulsification of the aqueous droplet inside a continuous phase of monoolein in squalane[30]. The movement due to deprotonation of surfactants at the interface is induced by the Marangoni effect[88]. Self-propulsion and possible self-assembly and self-sorting are directly linked to the dynamics of surfactant adsorption.
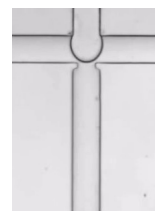
The Marangoni effect occurs due to a local variation of the interfacial tension which arises from the variation in composition or temperature[7,27,89], or an extension or contraction of the interface[89]. This effect was first noticed by James Thomson in 1855 and already qualitatively explained by Marangoni about 150 years ago[89]. It is also observable on a droplet moving with a non-zero velocity through a surfactant solution. Due to the movement, the surfactant molecules at the interface are concentrated at the back of the droplet leading to a non-uniform interfacial tension[7]. This interfacial tension is usually lowered upon increasing the surfactant concentration[2]. A interfacial tension gradient leads to a redistribution of the surfactant molecules to obtain a homogeneous coverage[7]. This flow at the interface opposes the initial flow. This Marangoni flow also rigidifies the interface[7]. A non-uniform distribution of the interfacial tension of a stationary droplet, due to other causes, leads to a movement of the droplet into the direction of lower interfacial tension.

During the entire time of self-propulsion, the surfactant distribution at the interface needs to remain inhomogeneous[7]. As an example, the self-propulsion of an aqueous droplet inside a surfactant-oil solution can be induced due to the adsorption of surfactants to the interface and the subsequent reaction of the surfactant with components from the aqueous phase[31]. This reaction leads to a mixture of different type of surfactant molecules at the interface which can lead to inhomogeneities of the interfacial tension at the droplet's interface, and thus, to self-propulsion. In such a process, the movement is related to two timescales resulting from the reaction rate and the adsorption / desorption kinetics[90]. In case the adsorption / desorption process is very fast, an instantaneous equilibration of the surfactant distribution takes place. In case the reaction rate is much faster than the adsorption / desorption process, the conversion of molecules at the interface will lead to a homogeneous distribution as well. In these two limiting cases, the droplet does not move. If the timescale of the reaction and of the adsorption / desorption kinetics become comparable, self-propulsion can become possible.

The stabilisation of droplets with surfactants is not only due to a decrease in interfacial energy and to steric hindrance of the surfactant molecules, but also due to the Marangoni flow. It stabilises the interface while acting against drainage of the continuous phase between two surfactant laden droplets. This mechanism increases the drainage time[7].

These behaviours of surfactants at out-of-equilibrium interfaces, including resulting self-propulsion, are not fully understood. Thus, a concerted effort is being made in our lab and within other groups[91,92] to study these phenomena in simple systems (minimal systems) in order to advance the understanding.

2.6 Microfluidics

Emulsions are used in many different areas in industry and every day life (Sec. 2.1). Often, these emulsions are polydisperse due to the production mechanism (shearing, spraying, stirring of two immiscible liquids)[4,11]. For the use of emulsions in biotechnological applications, monodispersity meaning every microreactor (droplet) has the same volume, is a prerequisite[7,11,18,19]. Monodisperse emulsions allow screening of reactions (biological, (bio-) chemical), which can be used for pharmaceutical or biotechnological applications because all reactions occur within the exact same environment[7,17].

Using droplet-based microfluidics, emulsions with highly monodisperse droplets can be produced. Further advantages of this method include high sensitivity in the detection (single molecular) with high-throughput (good statistics) including parallel and continuous processing of the different reaction steps[5,7,11,18,19,28]. In the following sections, I will introduce the important aspects of microfluidics.

2.6.1 Single-phase microfluidics

Microfluidics is the study of small amounts of fluids, in the range of 10^{-9} to 10^{-18} L[93], flown in channels of small dimensions (tens to hundreds of micrometer). A typical device consists of inlet(s) to introduce the fluid(s) into the channel(s) and a system of detection further downstream, from which a quantitative and/or qualitative output is obtained. Furthermore, the products are collected at the outlet(s). More concrete, the first microfluidic setups were developed for molecular analysis such as gas-phase chromatography (GPC) and high-performance liquid chromatography (HPLC, also high-pressure LC)[93]. Existing devices typically operate in the nanolitre to femtolitre range[94–96]. With optical detection methods using lasers, these methods combine high sensitivity and high resolu-

tion with the use of only small sample volumes. Advances in microfluidics were driven by the needs in the fields of biodefense (detection of small amount of chemicals in the field), molecular biology (sequencing of genomics and DNA (deoxyribonucleic acid)) and microelectronics (development of lithography)[93]. In all of these cases, the common need for low cost and rapid analysis with a high resolution and high sensitivity was realised by using microfluidic devices[93].
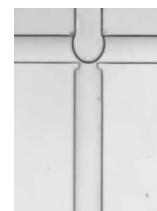
The huge advantage of the small dimensions in microfluidics is the laminar flow which gives a new quality on the control of localisation and time inside the microfluidic channel[93]. The flow can be characterised using suitable dimensionless numbers such as the Capillary number, the Reynolds number and the Péclet number (Sec. 2.6.2).

The Reynolds number Re relates the inertial forces to the viscous stresses with the velocity U, the viscosity μ, the density ρ, and the hydraulic diameter of the microchannel $D_H = 4A/p_w$ calculated from the cross-sectional area A and the wetted perimeter p_w[95,97].

$$Re = \frac{\rho U D_H}{\mu} \tag{2.24}$$

For the small lengthscales typical in microfluidics, the Reynolds number is generally smaller than 1, being characteristic for laminar flow[95,98,99]. Thus, mixing, which is required for many applications, occurs only through diffusion without the help of vortices which are present in turbulent flow. Specific channel geometries, e. g. a zigzag configuration, induce mixing through chaotic advection[100,101]. An additional difficulty in single-phase microfluidics, is the occurrence of dispersion induced by a parabolic velocity profile over the cross-section of the channel with the velocity being zero at the channel walls and maximum at the centre[101]. This leads to a non-uniform residence-time of the reagents across the cross-section of the chip and a non-uniform reaction progress at a specific distance from the start of the reaction.

2.6.2   Basics of droplet-based microfluidics

With the difficulties of mixing and dispersion of materials in single-phase microfluidics due to the above named phenomena, multi-phase microfluidics was developed. Here, droplets of one phase inside another phase are used to localise and encapsulate material[101]. The first droplet-based microfluidic experiments were performed in 2001[98].

(a)   (b)
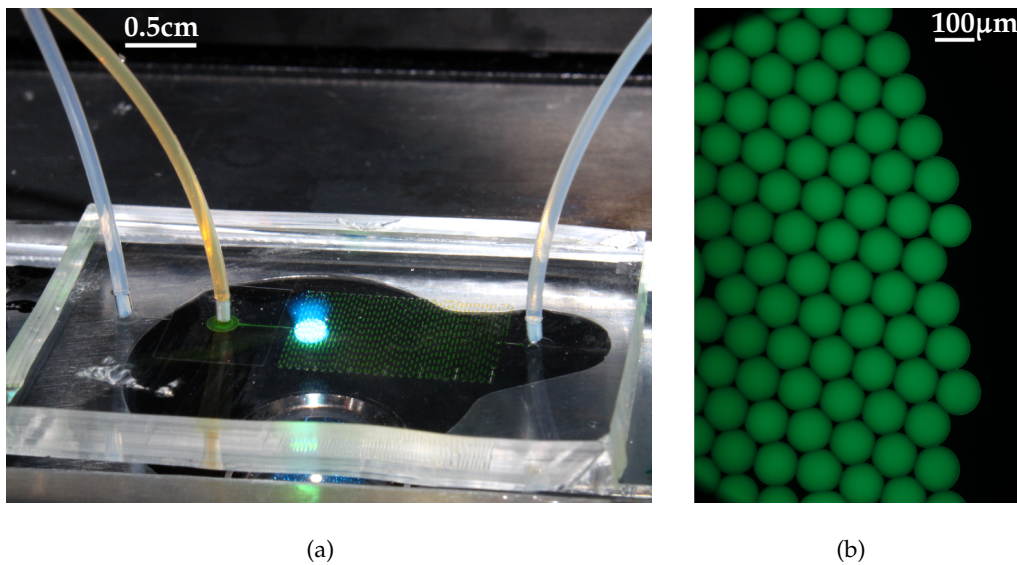
Figure 2.12: Monodisperse droplets produced with a microfluidic PDMS device. (a) Flow focussing (Fig. 2.13) PDMS device with the tubings attached (left: inlet fluorous phase, middle: inlet aqueous phase, right: outlet); the contrast is increased to make the droplets inside the channel visible. The device is mounted onto a fluorescence microscope with LEDs (here blue, see spot). (b) Fluorescein is encapsulated into monodisperse aqueous droplets with a fluorous continuous phase produced with the PDMS device in (a) using a flow focussing junction (Fig. 2.13).

Today, monodisperse droplets (Fig. 2.12) are produced using two immiscible phases which are injected into microfluidic channels with different geometries (Fig. 2.13), such as the co-flowing, cross-flowing (T-junction), flow focussing[95] or step emulsification geometry[102]. The flow rate of the two phases is controlled using syringe or pressure driven pumps[16,99]. Tubings connect the pumps with the chip (Fig. 2.12(a)). Droplet breakup is caused by homogeneous shearing of the two phases and a competition between the stresses which act locally on the fluid to deform the interface and the capillary pressure which acts against this deformation[95]. Generally, the droplet size is controlled by the channel geometries and the flow rate ratios of the two phases[95,99,103,104].

In addition to the flow rates, the production of monodisperse droplets depends on the capillary number Ca of the microfluidic system[105]. It relates the viscosity of the system μ, usually the viscosity of the continuous phase, and the flow velocity U to the interfacial tension, γ[8,106–108]:

$$Ca = \frac{\mu U}{\gamma} \, . \qquad (2.25)$$

Reducing the capillary number of a system, with given flow rates and channel geometry, leads to a domination of interfacial effects in comparison to viscous effects and increases the handling stability of the system[8,106,108]. At low capillary numbers, the droplet
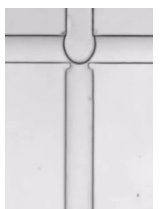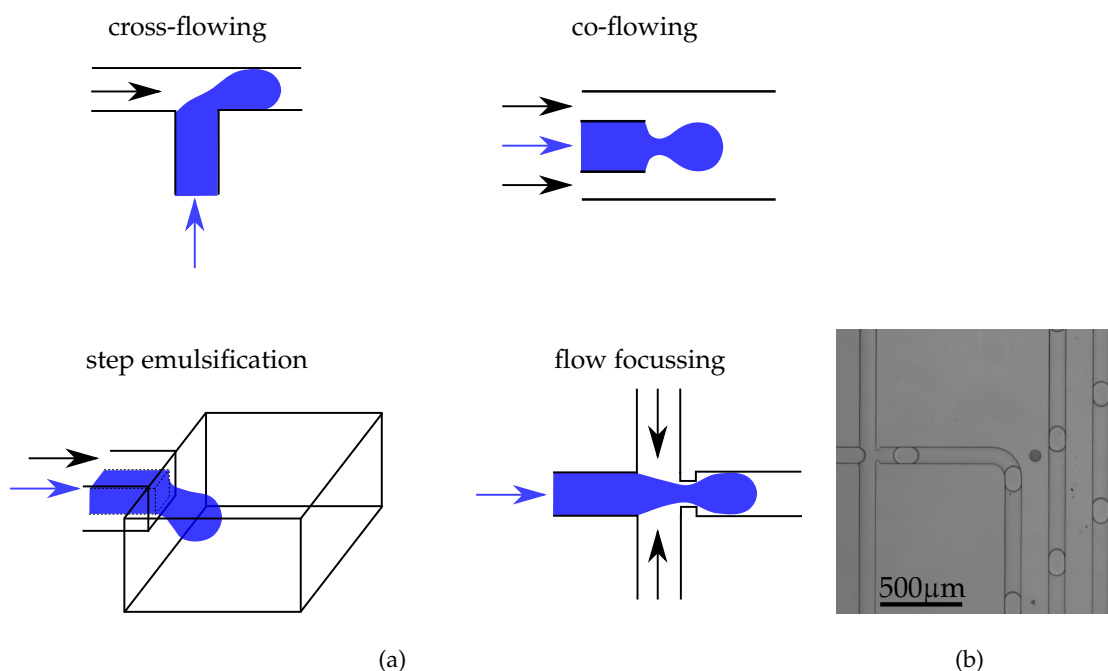
Figure 2.13: Channel geometries for the production of monodisperse droplets. (a) Emulsions are produced using two phases. As an example in blue: aqueous phase, no color: oil phase; the arrows show the flow direction of the aqueous (blue) and the oil phase (black), respectively. (b) In my experiments, I use the flow focussing geometry: the water is pumped from the left and the oil from the top and the bottom. To the right, the droplets are directed through a delayline (with bends to make it fit on the chip - see also Fig. 2.12(a)).

breakup is controlled by the channel geometry. An increase of the capillary number at droplet production results in higher viscous forces of the continuous phase exerted on the inner phase which stretch the droplet (inner) phase upon droplet production[108]. The 'geometry-controlled' breakup becomes first 'dripping' before it turns into 'jetting'[108] (Fig. 2.14). When surfactants are present, thread formation can occur at capillary numbers of around 0.4 to 1.0 (Fig. 2.14). Tipstreaming occurs in the same regime and is due to a combination of these capillary numbers with large flow rate ratios and surfactants at the interface[108,109]. Both tipstreaming and thread formation result in the production of additional small droplets (Fig. 2.14).

In the last paragraph, I have explained the effect of the channel geometry and the flow rate ratio on the droplet size as well as the effect of the capillary number on the flow regimes. In the following, I will discuss the flow pattern inside the droplet, which can be used to achieve mixing of the components inside the droplets. In single-phase microfluidics, mixing is achieved through specific channel geometries (e. g. a zigzag configuration, Sec. 2.6.1)[100,101]. For droplet-based microfluidics, a flow pattern forms automatically

(a)   Without surfactant

Capillary number increases

Geometry-controlled breakup   Dripping regime   Jetting regime

(b)   With surfactant

Capillary numbers around 0.4 to 1.0

Thread formation

Tipstreaming
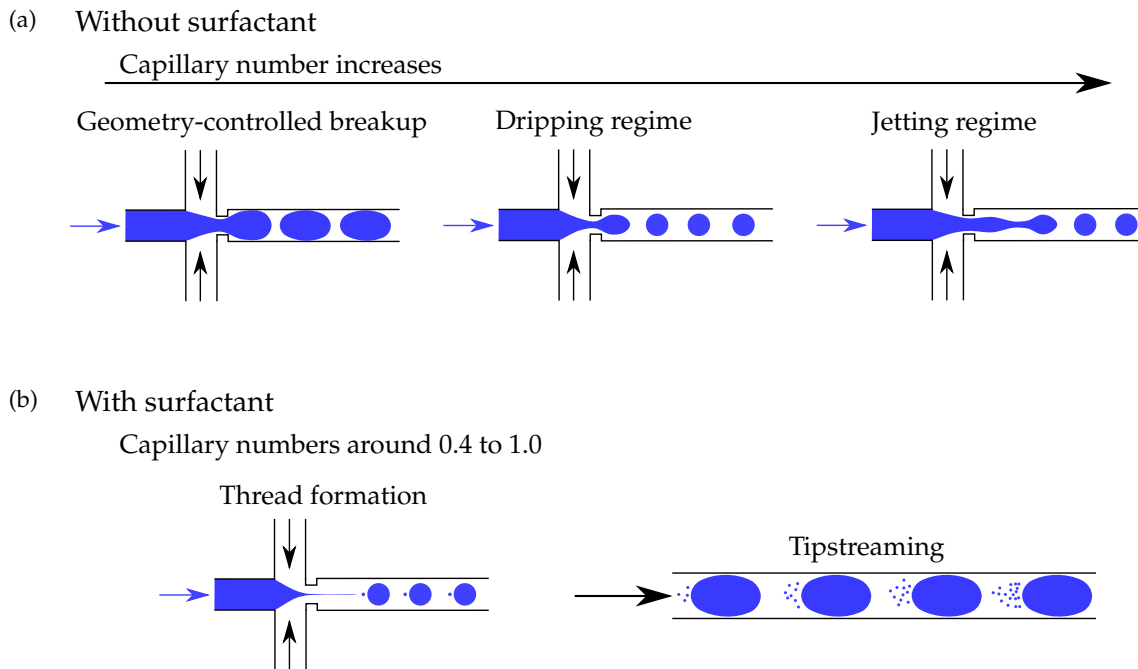
Figure 2.14: The different break-up regimes (a) with a pure two-phase system (as an example: blue: aqueous phase, no color: oil phase) and (b) with the presence of surfactant in a flow-focussing device. Surfactants can lead to the production of additional small droplets. (a)-(b) The arrows show the flow direction of the aqueous (blue) and the oil phase (black), respectively (adjusted from [108]).

inside the droplet and in the continuous phase inducing mixing. This mixing occurs only in the two halves of the droplet, but not across the centre (Fig. 2.15(a))[104,110–112]. For the use of droplets as microreactors, the droplet should be homogeneously mixed. This is achieved analogous to the mixing in single-phase microfluidics using channel geometries which lead to chaotic advection, e. g. winding channels (Fig. 2.15(b))[104,110–112]. The Péclet number, Pe, compares the convective with the diffusive transport. It compares these transports using the flow velocity, U, the characteristic length scale of the system, L, (for droplets, the size of the droplet) and the diffusion coefficient, D[110,113,114].

$$Pe = \frac{U\,L}{D} \tag{2.26}$$

If I consider the typical experimental conditions described in this work: droplet radius of 80 μm, a speed of ~20 mm/s and a diffusion coefficient of 10^{-10} m^2/s, the Péclet number is larger than 1 ($Pe = 16000$) which means that convection is prevalent over diffusion[110,113].
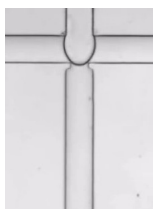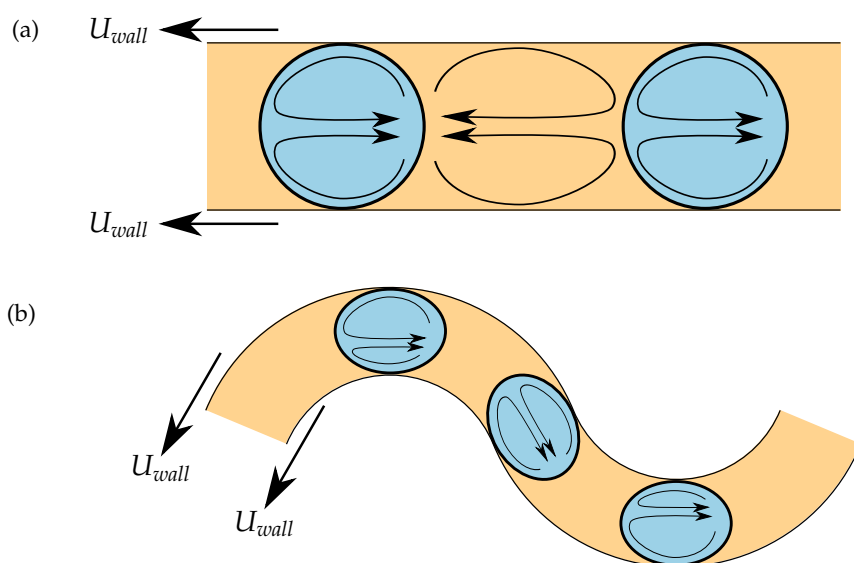
Figure 2.15: The flow pattern induced by flowing droplets in (a) a straight and (b) a winding microchannel in the reference frame of the droplet with the wall moving with a velocity U_{wall} (adapted from [104,110]). In the lab, the droplets would flow from left to right.

2.6.3 Manipulation of droplets on chip

Since the first experiments on the production of monodisperse droplets inside microfluidics [98], the demand for the manipulation of droplets on chip has continually increased. Additional to mixing in droplets on chip (Sec. 2.6.2), droplets can be split by elongation using specific channel geometries [16], fused by electrocoalescence [16,115,116], redirected with valves by changing the pressure in adjacent channels [93], sorted by dielectrophoretical forces [20,117–119] and trapped by making use of the surface energy of the droplet upon deformation [120–122]. Small amounts of solutions can be added to the droplets (picoinjection) [123] or emulsions can be broken using electric fields [124]. For applications requiring an electric field, electrodes can be fabricated by introducing molten metal (e. g. low-temperature soldering) into additional microfluidic channels [119,125,126]. These additional channels are directly included when designing the microfluidic chip. Thus, these electrodes require no alignment as the microfluidic channels define their positions.

Today, there are lab-on-a-chip devices for an extensive range of applications utilising multi-phase flow and droplet manipulation methods. Despite an unprecedented level of control over emulsions made with microfluidic devices, their application at the industrial scale is limited by their relatively low throughput [127]. High-throughput droplet pro-

duction refers to 1000 to 10 000[7] droplets per second with diameters of ~100 μm. This production rate, though, provides only a volume of ~5 mL/h which equals ~10 kg per year[128]. Thus, many research groups are still working towards large-scale droplet production with the achievement of already a couple of hundred millilitres per hour[128–130]. Many industrial formulations need 1000 tons per year[127]. Such a production would need 100 000 parallel droplet makers requiring a volume of the device of 40 L[127]. The space required is similar to commercial homogenizers (polydisperse droplets) but the parallelisation of the droplet makers is challenging. From a commercial point of view, the throughput which are nowadays achievable are only enough for formulations with the need of small volumes such as in the pharmaceutical and cosmetic industry[127].

2.6.4 Fluorous continuous phase

After the description of microfluidics, I will now explain the criteria for the continuous phase and the surfactants which lead to a stable droplet production. The combination of the continuous phase with the surfactant does not only have to lead to a stable production, but the continuous phase including the surfactant must not interact with the interior of the droplet (chemically inert). For devices dealing with biotechnology (e. g. screening applications), this translates into the need for a bicompatible continuous phase and biocompatible surfactants[7,18,19]. The correct choice of the continuous phase and the surfactant can be very challenging[18].

In this part, I describe important aspects concerning the continuous phase. The capillary number describes if viscous effects dominate over interfacial effects meaning a low capillary number is of advantage in droplet-based microfluidics (Sec. 2.6.2)[8,106]. This means, that for a fixed speed and fixed channel geometries, a small viscosity and a high interfacial tension is of advantage.

A combination of fluorous oils with fluoro-surfactants conforms to these conditions[8]. These oils are usually perfluorinated and contain one functional group (e. g. amine or ethoxy). Fluorocarbons are molecules consisting only of fluorine and carbon atoms[8,131]. Due to long names for some substances, the prefix 'perfluoro' is used to define the substitution of all hydrogen atoms of a molecule by fluorine[8,132]. Fluorocarbons show different properties than hydrocarbons.
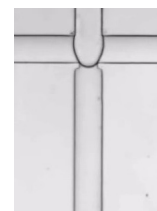
These properties depend on the molecular structure, which I will now discuss in detail. The different properties between fluorocarbons and hydrocarbons are mainly due to the size and electronegativity of the fluorine atoms which show the strongest bonds (C-F) in organic chemistry. The high electronegativity of the fluorine atom leads to extremely polarised C-F bonds with low polarisability. For this reason, the fluorine atom is not a good lone pair donor [8,133,134]. Thus, the C-F groups interact only weakly with other molecules or functional groups by electrostotatic or dipole interactions [133,134]. The high electronegativity also strengthens the C-C bonds from the backbone of the molecule by electron withdrawal [133]. In fact, perfluorocarbons are the least polar existing fluids [8,135,136]. The low polarisability leads to low surface energies, low interfacial tensions and low cohesive forces between fluorocarbon molecules [8,133,137] and above a critical temperature [8,49] to a miscibility of fluorocarbons with aliphatic hydrocarbons [8,50]. This temperature increases with increasing length of the chain of the molecules. Therefore, bigger hydrocarbon molecules are less soluble inside a fluorous phase than smaller ones [8,49]. The solubility of small molecules, e. g. naphtalene in $(C_4F_9)_2)O$ or $(C_3F_7)_3)N$ at 25°C, is extremely small and is only of the order of 0.3 mol percent [8,138].

The low solubility of organic molecules in fluorocarbon fluids results in less partitioning and cross-talk between emulsion droplets [139]. Furthermore, the low intermolecular forces lead to a high compressibility and high interstitial space resulting in a high solubility of respiratory gases, such as oxygen and carbondioxide [8,133,137]. This makes fluorocarbons suitable for blood substitutes and cell culturing in emulsions [8,133,140,141]. Another advantage for applications in microfluidics is directly related to PDMS, the channel material commonly used. In contrast to hydrocarbons, fluorocarbons do not swell PDMS [7,8,142]. All these properties render water-in-fluorinated-oil emulsions a very promising systems for the use in droplet-based microfluidics [7].

2.6.5 Surfactants in microfluidics

Having defined favourable properties for the continuous phase being a fluorous phase, the surfactants have to be adjusted. These surfactants need a fluorophilic and a hydrophilic part [7]. The molecules available for such applications is still limited [7].

Up to now, the most promising surfactants consist of a di- or tri-block copolymer of perfluoropolyether (PFPE, fluorophilic) and polyethylenglycol (PEG, hydrophilic) [7]. These
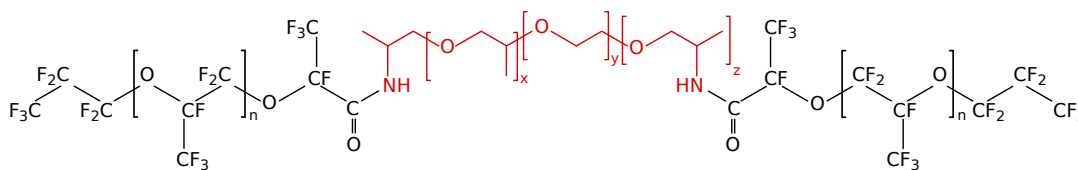
Figure 2.16: PFPE-PEG-PFPE surfactant (black PFPE, red PEG). Different size can be used for the repeating units; in this case: $y \sim 9$, $x + z \sim 3.6$, $n = 22$ (determined in Sec. 4.3.1).

surfactants show a small interaction with cells and proteins inside the droplets making them suitable for the screening of many different cells (mammalian, yeast), bacteria and viruses[7]. The synthesis of these surfactants is well reported as well[143].

Some problems still arise from interactions of the surfactant with encapsulated molecules[8] and from phase partitioning (Sec. 2.1, 2.2), which is due to a finite solubility of molecules of the dispersed phase inside the continuous phase or in reverse micelles (bilayers do not form in these emulsions used here)[8,28]. Depending on the system, the rate of transport is influenced by the partitioning[144,145] as well as by interfacial properties[146–151]. As mentioned in the previous section, organic molecules are mostly insoluble in fluorous phases. These molecules can, however, be extracted changing the partitioning by introducing fluorinated groups into the molecules. This modification can lead to selective extraction[152–154] via non-covalent interactions such as hydrogen bonding or ion pairing depending on the functional groups present[135]. Perfluorinated acids (e. g. perfluoropolyether with a carboxylic headgroup, Krytox DuPont) are surface active molecules. The acid and also its salt form dimers in fluorous solvents[155–159]. The first study on the increased solubility due to intermolecular hydrogen bonding with perfluorinated carboxylic acids was shown using urea[159]. It has to be noted that the interaction of a O-H group with a nitrogen atom is even stronger than with an oxygen atom[156–158,160].

Due to this fact, an appropriate surfactant without the possibility of non-covalent interactions would be perfect. One of the most used surfactants is a PFPE-PEG-PFPE surfactant (Fig. 2.16). This surfactant is synthesised from the PFPE carboxylic acid and the PEG using a two-step synthesis[143]. In the first step, the carboxylic acid is activated to its acyl chloride. In a condensation reaction, it reacts with a primary diamine yielding an amide bond[143]. In the literature, the analysis shows that the reaction is not complete[143,161,162]. Thus, left over carboxylic acid is inevitable and easily leads to leakage problems.

In this chapter, I have described properties of emulsions and their stabilisation using surfactants. I have given an introduction on the effect of surfactants on interfaces including
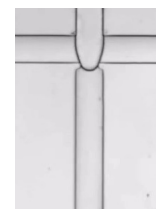
methods for their characterisation and challenges for the use in emulsion stabilisation. Furthermore, I introduced droplet-based microfluidics for the production of monodisperse emulsions. In the next chapter, I describe my experiments used in this study including all necessary materials.

Summary of Chapter 2 – Theoretical Background

I have introduced the physico-chemistry of emulsions and surfactants at interfaces and the methods to characterise them.

The key result coming from this analysis is that the kinetics of surfactant adsorption depends on the droplet size. One can define a critical droplet radius $R^* = D/(k_{ads}\Gamma_\infty)$ which is typically in the range of 50 µm: For droplets with a radius $R < R^*$, the kinetics are always limited by the adsorption / desorption process.

Microfluidics is, therefore, a key technology to study the kinetics of surfactant layers.

Chapter 3

Experimental Methods and Techniques

Parts of this chapter are included in P. Gruner and B. Riechers *et al.*[61] (in press 2015) and in B. Riechers *et al.*[43] (in preparation 2015).

3.1   Manufacturing of microfluidic devices

Having described the basics of microfluidics and manipulation on chip, I will now illustrate the production of microfluidic chips used in this study, starting with the description of lithography before describing micro-milling and embossing[163]. I start with a general introduction before describing the materials and methods used in my experiments.

For the lithographic production of microfluidic chips, the design of the device is created with a computer-aided design (CAD) software[163–165]. It is printed on a transparent foil (such as those used for overhead projectors, Fig. 3.1(a)) using a commercial image setter with high-resolution to obtain the photomask.
Using contact photolithography and the printed photomasks, a master containing the channels is produced for replica molding[163–165] (Fig. 3.1(b)-(c)). In the first step of photolithography, a photoresist is spincoated onto a silicon-wafer to obtain a specific height of the resist and, thus, of the final channels[16,166]. The resist is covered with the mask

(a)

(b)

(c)

(d)

(e)

(f)
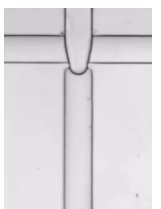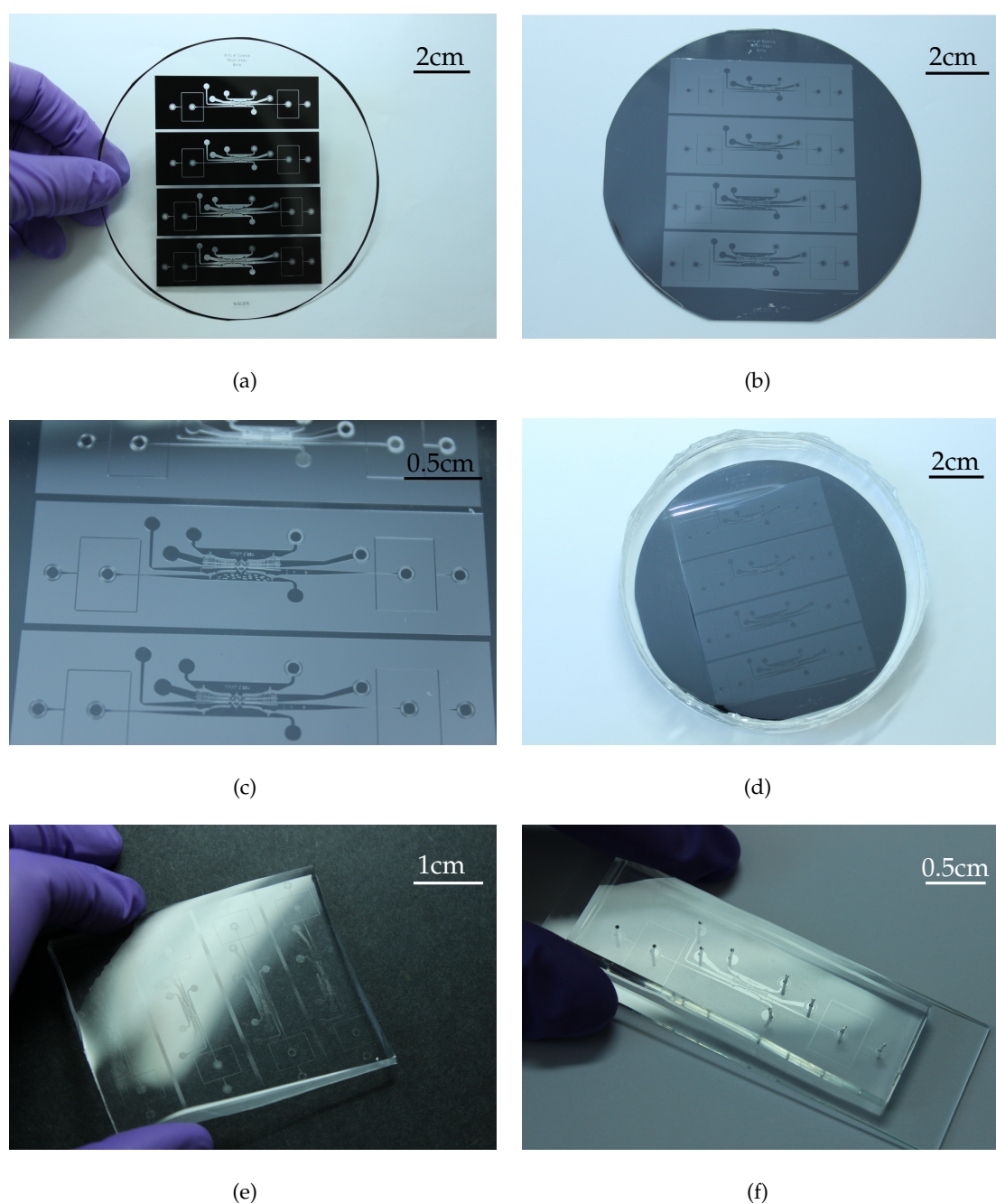
Figure 3.1: An example of the process of mask printing, photolithography, soft lithography and PDMS-glass bonding. (a) Photomask, (b) Master, (c) Zoom of master, (d) Master with PDMS, (e) PDMS, (f) PDMS-chip with microfluidic channels.

for UV (ultraviolet) illumination. A negative photoresist, such as SU-8 (photocurable epoxy) used in this study, polymerises upon UV-exposure. Upon development, the part of the resist which was not exposed to UV-light is washed away to obtain the master (Fig. 3.1(b)-(c)). Additionally, these steps can be repeated to obtain double layers of the resist leading to different heights at different positions of the channels[166]. With such a

master, at least 50 replications can be obtained using soft lithography[167].

In the first step of soft lithography, a liquid prepolymer and its crosslinker (usually poly(dimethylsiloxane) (PDMS)[163]) is cast onto the master[163,164] and degassed[16]. The polymer is crosslinked at elevated temperature (Fig. 3.1(d)) before the replica is peeled from the master (Fig. 3.1(e))[164,167]. The holes for the in- and outlets are punched into the device before it is glued to a substrate using plasma cleaning (Fig. 3.1(f))[164]. The air (or oxygen) plasma produces polar groups on the surface of the PDMS and the substrate[16,164]. Upon contact, the substrate seals the microfluidic channels by condensation of silanol groups with the functional groups of alcohol, carboxylic acid or ketones[164]. The sealing, using this technique, withstands up to 2 to 3.5 bar[164] (Table 3.1).

Untreated PDMS is hydrophobic. Its surface properties can easily be modified upon treatment with plasma or chemicals[163]. To change the wettability of the channels, appropriate chemicals are added which react with the functional groups of the PDMS[164].

PDMS is widely used as it is inexpensive, easily manageable and non toxic (Table 3.1). The elastomeric character of PDMS is an advantage as it allows formation of complex and fragile structures[163]. The deformability of the PDMS allows for good contact also with non planar surfaces. However, in some cases, the elasticity makes it an unsuitable choice[163]. Not all aspect ratios of channels can be obtained due to the deformability as sagging and paring of structures occurs upon too high or too low aspect ratios[163]. The shrinking upon curing (about 1%) is a disadvantage as well[163]. A further advantage of PDMS is the optical transparency down to about 300 nm enabling for photoreactions inside channels using UV light[163]. PDMS is a durable polymer[163] but it swells and dissolves in many common nonpolar organic solvents[93,142]. It has a high permeability to carbon dioxide and oxygen, enabling for the use in biological applications[93]. The high permeability towards water is a significant draw back. For experiments requiring the use of PDMS incompatible solvents or the control of water vapour, other suitable materials such as NOA (Norland Optical Adhesive) should be used instead[16] (Table 3.1). NOA has other disadvantages such as the fluorescence in the visible range[168].

Other polymers such as poly(methyl methacrylate) (PMMA), polystyrene (PS), fused silica and fluorinated thermoplastic polymers have also been successfully used for the production of microchannels[19] (Table 3.1). Usually, these microchips are produced using micromilling[16,116,167,169–173] and/or hot embossing techniques[16,167,169,170,174,175].
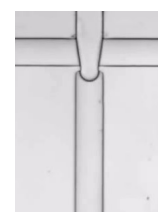
Table 3.1: Comparison of different materials for microfluidic chip production. In this study, I used PDMS and PMMA.

	PDMS	PMMA	Glass	NOA
Cost	cheap [182]	cheap [182]	expensive [182]	cheap [182]
Production	easy [182]	easy [182]	elaborate [182]	medium [182]
Fabrication time	rapid [182]	rapid [182]	slow [182]	good [182]
Resolution	sub-micron [182]	micron [169]	high [182]	sub-micron [182]
Solvent compatibility	low [182]	medium [175]	high [182]	good [182]
Deformability (Young's modulus)	0.5-4 MPa [182]	3 GPa [182]	63 GPa [182]	325 MPa [182]
Pressure before failure	2-3.5 bar [164,182]	3.2 bar [169]	high [182]	4.8-5.5 bar [182]

In the following, I will focus on PMMA as this was the choice for my adsorption experiments. It can also show fluorescence in the visible range, but PMMA needs a lower excitation wavelength than NOA making PMMA usable for the adsorption measurements in this study [168,176,177]. PMMA is a low cost disposable material and replication of devices is easy and fast. It is biocompatible, optically transparent having an amorphous structure and it is stable with temperatures up to about 80°C [175,178]. It does not deform as much as PDMS [179]. Due to this, it has a larger operation window than PDMS and the microfluidic chips can be reused for several months (14 months [175]).

The microfluidic channels are either directly fabricated into the PMMA or milled into a stamp and replicated into PMMA using hot embossing. The direct fabrication includes writing with a CO_2 laser [170,180,181] or drilling with an end mill [169,171,172]. The PMMA plate including the channels and a PMMA substrate are combined using hot embossing. More precisely the plates are pressed (8 to 15 bar [169]) together at an elevated temperature (80 to 100°C [169]) to slightly overcome the glass transition temperature (depending on the PMMA ~100°C [169,180]), melting the surfaces together [169,170,180]. This bonding is improved upon cleaning the surfaces with oxygen plasma before bonding [180]. Using this treatment, a bonding strength of up to 3.2 bar is obtained [169] (Table 3.1). If the microfluidic channels are to be replicated in big numbers, a metal mold (CNC milling with high precision), from which the structures are transferred into PMMA by hot embossing, is more convenient. In the following, I will describe the process of device fabrication for the microfluidic channels in PDMS used in this study. Afterwards, I will explain the production of the PMMA devices, which I used for the determination of adsorption kinetics using pH measurements at the microscale. For all other measurements, I used the PDMS devices.

3.1.1 PDMS device – Lithography

I manufactured microfluidic channels in polydimethylsiloxane (PDMS) using standard photo- and soft lithography techniques (see Sec. 3.1)[163–165]. I designed the channel geometries using a computer-aided design (QCad or LibreCAD) software. This design was then printed on a mask (Selba S.A., laser photoplotting on film, resolution 50800 dots per inch (dpi)). I performed photo-lithography for the production of the mold, using the negative photoresist SU-8 (Series 3000, Microchem), spin coated on a silicon wafer (Si-Mat, diameter 10 cm, thickness 525 ± 25 µm) after having cleaned the wafer with Ethanol and having dried it on a hotplate (200°C, 20 min, No. 4 on CB3000 Stuart). After spin coating (Laurell Technologies Corporation, model WS-650MZ, 23NPPB), I soft baked (95°C, Prescicion Hotplate, ems electronic microsystem Ltd. Model 1000-1) the resist. I placed the mask on the resist and illuminated them with UV light (UV KUB 2, Kloé maximum, dose 25 mW/cm^2, wavelength 365 nm). The UV light is not perfectly collimated[1] but the divergence is less than 2°. This means, that a good contact between the mask and the SU-8 is needed for high spatial resolution in the plane of the wafer and good verticality of the edges. For this, I placed a UV-transparent glass slide (Pyrex) onto the mask. I performed the post exposure baking (95°C) before developing the SU8 (Microchem). Then, I rinsed it with 2-propanol (AnalaR NORMAPUR® ACS, VWR) and dried it with nitrogen. I checked the quality of the developing step under a microscope before performing the hard bake (2 min at 95°C, 5 min at 200°C, 2 min at 95°C). For different heights of the SU-8 layer, I adjusted the spin speeds (see Table 3.2, Figure 3.2), the UV dose and the baking times using the information of the SU-8 data sheet.

For the replica molding, I used PDMS (10:1 polymer to curing agent, Sylgard® 184 silicone elastomer kit, Dow Corning), degassed it (desiccator under vacuum for 45 min) and cured it in an oven (~70°C for 2 h, Dry-Line DL53, VWR). I peeled the PDMS from the mold and punched the inlets and outlet using a biopsy punch (Harris Uni-Core^{TM}, diameter 0.75 mm). Then, I glued the PDMS and the glass substrate together using a Plasmacleaner (air at 0.45 mbar, 30 s, 70%, Diener electronic, Pico). I rendered the channels fluorophilic by injecting Aquapel (PPG Industries) into the channels. I rinsed the channels with Argon before and after the treatment of Aquapel as Aquapel reacts with air. I determined the

---

[1]Information from the company, KLOÉ.
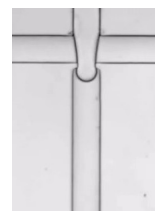
Table 3.2: The settings for the second step of spin coating to obtain different heights of the SU8 resist. The acceleration step is set to a speed of 600 rounds/min with acceleration of 100 (200) rounds/min^2 with a duration of 6 (3) s (in brackets, information for first sample).

| height (μm) | | spin coating | | | SU8 | colour |
| targeted | obtained | speed | acceleration | duration | | in |
		(rounds/min)	(rounds/min^2)	(s)		Fig. 3.2
8	8.2	4000	600	36	3010	green
8	6.8	4000	600	36	3010	blue
15	17	1000	200	32	3010	red
15	19	1000	200	32	3010	black
25	27	3000	300	38	3025	maroon
40	43	1800	300	34	3025	orange

heights of the channels by cutting the devices in half and measuring the cross sections of the channels with a microscope (Tab. 3.2, Fig. 3.2).

Using the photo lithographic process[2], I establish a calibration curve for the height of the microfluidic channels in PDMS (Fig. 3.2, tab. 3.2). I obtain the targeted values within the error due to the measurement at different positions on-chip and upon cutting the PDMS.
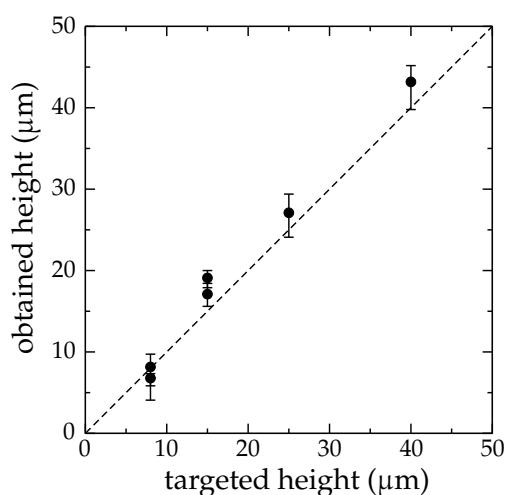
Figure 3.2: The height determined for the different molds produced with the specification of tab. 3.2. The error bars reflect the height differences due to different positions on chip and due to errors in the determination of the height of each microchannel.

---

[2]This experiments were performed at the CRPP (Centre de Recherche Paul Pascal)
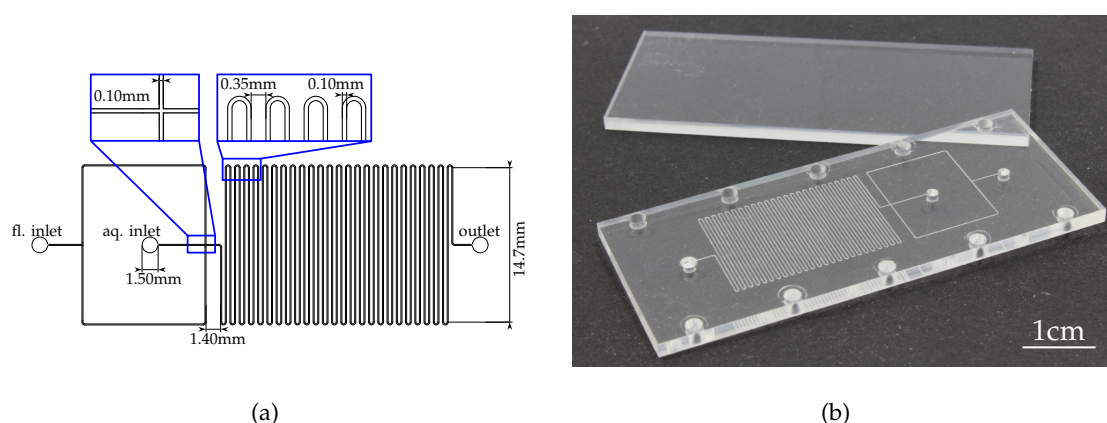
Figure 3.3: PMMA channels prepared with an end mill. (a) Design used for the experiment including the inlets for the two phases (fluorous (left), aqueous phase (middle)) and the outlet (right). (b) PMMA substrate and plate with design engraved.

3.1.2 PMMA device – End milling

As described in Section 3.1, the elasticity of PDMS makes it an unsuitable material for devices with high pressures. For the experiments of the adsorption kinetics involving long channels, I used the PMMA device fabrication.

I designed a channel with a droplet production and a long delayline of the microfluidic channel of 75 cm. The PMMA chip needs two parts: one plate in which the design is milled and one plate as the cover. The microfluidic channels were milled[3] into a PMMA plate (height 2 mm, length 60 mm, width 25 mm, Fig. 3.3)[169,171,172] using an end mill with a diameter of 100 μm (Fig. 3.3, for the speed measurements 150 μm in diameter). To measure the height and uniformity of the channel, I used a white light interferometer (Wyko NT 1100, Veeco, Plainview, NY).

I cleaned the PMMA plate including the channel and another PMMA plate for the cover with the same dimensions (Fig. 3.3(b)) mechanically, in 2-Propanol (ACS reagent, 99.5%, Sigma-Aldrich) in an ultrasound bath (5 min) and twice with plasma[180] (see Sec. 3.1.1). I then combined the two parts using a temperature-controlled press (5 kN at 100°C for 40 min, P/O/Weber)[180]. For stress reduction, I cooled the chip down slowly (~30 min). Finally, I connected the inlets and the outlet of the PMMA chip with the tubing using nanoports (coned, 10-32, Polyether ether ketone (PEEK), Upchurch) which I glued to

---

[3]This milling was done by the mechanics workshop at the Max Planck Institute for Dynamics and Self-Organization (Feinmechanische Hauptwerkstatt) thanks to Wolf Keiderling and Andreas Gerke.
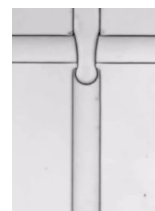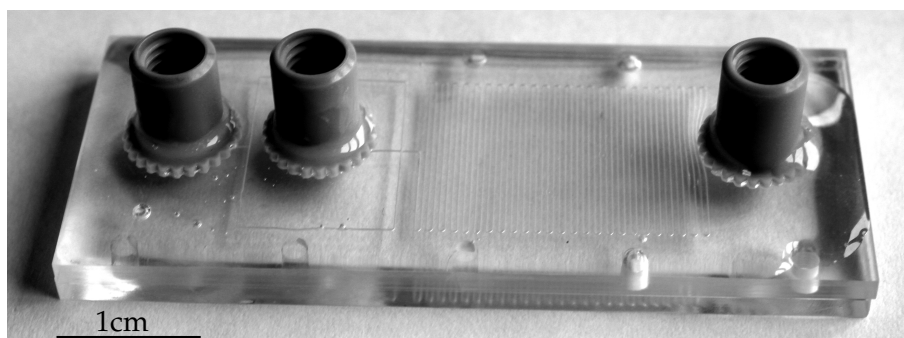
Figure 3.4: Photo (contrast enhanced, desaturated to black and white) of the PMMA device including microchannels and connectors to introduce the two phases (left: fluorous, middle: aqueous) and collect the droplets at the end (right).

the chip applying UV-light (30 min, 365 nm, Polylux-PT, Dreve) onto a UV-curable glue (Loctite, 35261). I coated this PMMA device (fig 3.4) using a coating agent (3 x 15 min, Aquapel, PPG Industries) before I dried the device with nitrogen. The PMMA device is stable using the solvent Novec7500 and the surfactant in solution. Other solvents, such as ethanol and isopropanol are not compatible with the PMMA device, as delamination takes place. Aceton even dissolves PMMA. For the storage and the reuse of the PMMA channels, drying is a great disadvantage as particles clog the channels upon reuse. For small aggregates, rinsing with Novec7500 or water while immersing the device in an ultrasound bath generally solves the problem. To circumvent aggregates inside the channels, the device can be stored with a solvent inside, e. g. fluorinated solvent Novec7500, while avoiding air bubbles and evaporation of the solvent.

For the end milling, the uniformity of the channel height depends on the height differences at different positions on the original PMMA plate used for milling. The height of the channels, which I use for the pH measurements, is very uniform, with 99 μm ± 3 μm (Fig. 3.5) after milling. The mean width of the channels is 95.6 μm ± 4.2 μm. After the bonding step, the channel height is reduced to about 80 μm. I obtain this information from another chip with the same quality upon taking it apart (data not shown). For the velocity of the droplets, I use the 80 μm in height.

3.1.3 Device operation

I injected the two phases into the devices using glass syringes (Hamilton, Gastight, Series 1000, VWR) with needles (Einwegkanülen, Neolus®, Luer, 25 mm length, 0.6 mm
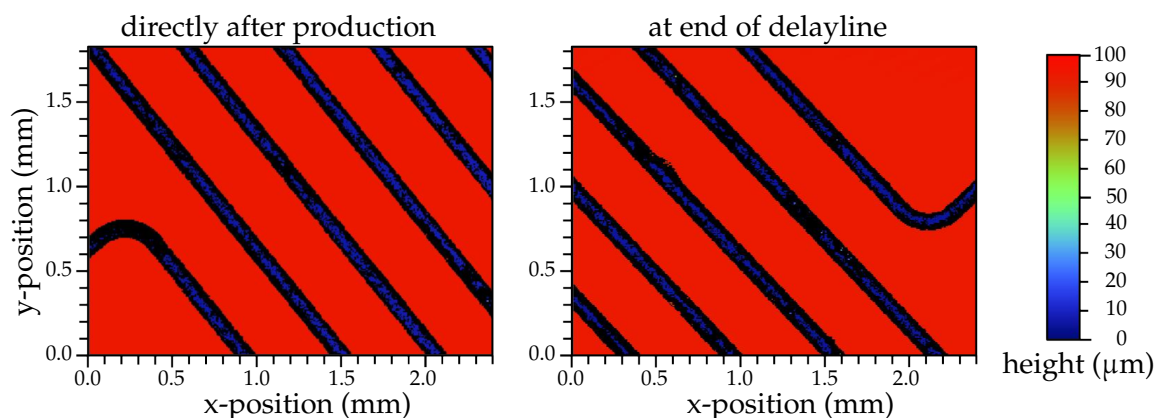
Figure 3.5: Heights of PMMA channels at different positions on chip measured using a white light interferometer. Due to the roughness of the channels, the height in some points could not be measured (black).

diameter, G23, VWR) which I connected to the microfluidic device using Polytetrafluoroethylene (PTFE) tubing (outer diameter (O.D.) 1.07 mm, inner diameter (I.D.) 0.56 mm, Fisher Scientific). I connected the tubings to the PDMS device, by introducing them directly into the hole. For the PMMA device, I connected the syringes with the device using fittings (short headless nut (F-333Nx) with ferrules (F-142N) and nanotight sleeves from fluorinated ethylene propylene (FEP, F-252x, O.D. 1.59 mm, I.D. 1.07 mm, Upchurch). I controlled the flow rates using syringe pumps (neMESYS 29:1, Cetoni). In contrast to PDMS, a stable droplet production without the use of surfactants is possible[182] with this device (150 μm channel width) using flow rates up to 80 and 5 μL/min or 60 and 15 μL/min for the fluorous and aqueous phase, respectively. I did not apply higher flow rates.

3.2 Surfactant characterisation

For all experiments, I characterised the surfactant with standard bulk methods. I used standard interfacial tensiometry to determine the dependence of the interfacial tension on the surfactant concentration and time, giving rise to the value of the CMC and the maximum interfacial coverage (for the adsorption measurements and the biomimetic experiments). Furthermore, I determined the molecular weight of the surfactant, Krytox, as it deviates from the value given by the supplier[143,158,160] (for the adsorption measurements and the synthesis). Here, I used mass spectrometry and nuclear magnetic resonance spectroscopy. I implemented all data from the bulk measurements of the KrytoxFSL into the adsorption model obtained from microfluidics to determine absolute values.

For the characterisation of the adsorption kinetics, I used a fluorous phase containing the fluorous solvent Novec7500 (3-Ethoxyperfluoro(2-methylhexane), 3M) with a molecular mass of, M, 414.11 g/mol and a density, ρ, of 1.617 g/mL. This phase contained the surfactant KrytoxFSL (perfluoropolyether with a carboxylic headgroup with small molecular weight, Sec. 4.1.1, DuPont). For the aqueous solutions, I used a phosphate buffer saline (PBS) solution (Sigma-Aldrich, 10 mM phosphate buffer, 0.154 M sodium chloride, density is considered as 1 g/mL).

I used KrytoxFSH (high molecular weight, DuPont, Sec. 4.3.1) for the synthesis of the surfactant.

For the system showing biomimetic behaviour, I used oleic acid ($\geq$ 99%, Sigma-Aldrich) as surfactant in a continuous phase of squalane ($\geq$ 99%, Sigma-Aldrich). I used millipore water for the determination of the interfacial tension and the CMC. As seen during the tensiometric experiments, the squalane contains surface active impurities which need to be removed to characterise the squalane solutions. I filtered the squalane over Celite® 545 (Sigma Aldrich) using a glass frit (porosity 1) and low pressure. Additionally, I filtered it by gravity filtration using a glass column (diameter 7 cm) which I packed with Alumina (Aluminium oxide, activated, pH = 9.5, Brockmann I, Sigma Aldrich) to a height of 15 cm[80].

3.2.1 Molecular weight of surfactants

Mass spectrometry (MS) was measured in the positive range (m/z 600.00 - 4000.00) using a LTQ XL mass spectrometer (Thermo Fisher, Bremen). Electrospray ionisation (ESI) was used in combination with an ion trap (IT) to determine the mean molecular weight in profile mode[4]. The ESI-MS could not be obtained for the KrytoxFSH, as its molecular mass is too high.

To compare the accuracy of the molecular mass determination, I used nuclear magnetic resonance (NMR) spectroscopy. I prepared a 1:1[5] (w/w) solution of KrytoxFSL and the solvent Novec7500 containing 10% (w/w) Chloroform-d$_1$ (99.8%, 5 x 1 mL, Deutero

---

[4]This measurement was performed by Uwe Pleßmann, member of the research group of Henning Urlaub: Bioanalytical Mass Spectrometry from the Max Planck Institute for Biophysical Chemistry.
[5]0.999:1.000

GmbH). 1D ^{1}H-NMR experiments were recorded at 25°C on a Bruker Avance 400 MHz spectrometer using 16k points and 256 scans with a spectral widths of 4006 Hz.[6] For the determination of the molecular mass of the KrytoxFSH, I also used 1D ^{1}H NMR spectroscopy with a 1:1[7] mixture of KrytoxFSH with Novec7500.

3.2.2 Bulk pH measurements

For the calibration of the experimental setup for the adsorption kinetics, I used 0.1 M HCl and 0.1 M NaOH (Sigma-Aldrich) to change the pH of the PBS solution to 5.46, 5.70, 5.84, 6.04, 6.31, 6.72, 7.10, 7.31, 7.66, 7.94, 8.05, measured with a pH meter (Thermo Scientific, Orion, Star A121), pH electrode (SI Analytics, pH-Einstabmesskette N64) and Automatic Temperature Compensation Probe (Thermo Scientific, Stainless Stell 8" MD Connector). For the titration of the PBS-solution, I diluted a titer of 1 mol of HCl (36.461 g HCl, FIXANAL®, Fluka analytics) with millipore water (Merck Millipore, Milli-Q Advantage A10) to obtain a solution of 0.1 M HCl. I titrated the phosphoric acid (10 mL, 0.1 M, 1x PBS) solution with the titer of 0.1 M HCl (black circles in Fig. 4.5) to obtain the relationship between the amount of protons added and the change in pH.

3.2.3 Tensiometry

I performed interfacial tension measurements of liquid-liquid interfaces with two different setups, namely the pendant drop method[6,71,75,76] and the Wilhelmy plate[1,6,71] configuration. I obtained the change in interfacial tension with time for either a droplet of one phase in another or a flat interface, respectively.

Pendant drop method

The pendant drop method uses the shape of the droplet to calculate the interfacial tension between two fluid phases. I performed such measurements using a pendant drop setup

---

[6]This measurement was performed with the help of Elias Akoury within the research group of Markus Zweckstetter, Structure Determination of Proteins Using NMR, at the Max Planck Institute for Biophysical Chemistry.

[7]1.006:1.000
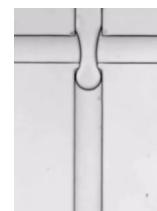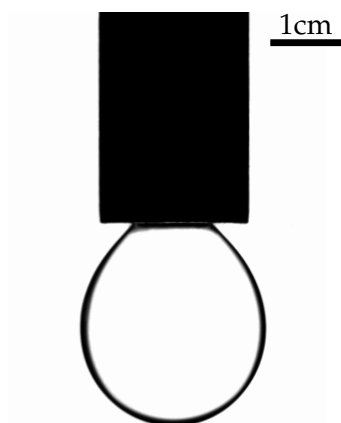
Figure 3.6: Pendant drop of a fluorous oil phase in an aqueous continuous phase.

(Profile Analysis Tensiometer PAT-1M, SINTERFACE). The droplet of a surfactant solutions (oil phase) was automatically produced inside the aqueous phase with a syringe with defined diameter (2 mm) (Fig. 3.6). The shape of the droplet was captured (1 s^{-1}) by a camera (PixeLINK Firewire Camera Release 4) and then fitted to the Young-Laplace equation (Sec. 2.3). The calculation was performed by the program of the pendant drop setup using the needle diameter for the calibration and a gravitational acceleration of 9.807 m/s^2. The production of the droplet was defined as time zero. The program measured a maximum of 100 000 s, but for solutions having very long equilibration times, I restarted the measurement after about 100 000 s. During the whole experiment, the droplet volume was kept constant with a feedback mechanism between the real and theoretical droplet size. I set the volume (size) of the droplet, to the maximum possible without the droplet falling.

With this setup, I characterised the interfacial tensions between solutions containing different concentrations of KrytoxFSL as surfactant inside the fluorous phase Novec7500 with an aqueous phase of millipore water or PBS (see Section 3.2).
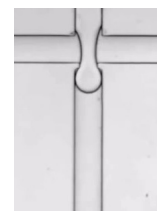
Wilhelmy plate method

I used the Wilhelmy plate method to measure the interfacial tension of a plane interface (KSV-Nima LL, KN-ISR-2, LOT Quantum Design, Fig. 3.7(a)). For this, I carefully layered the two phases on top of each other to obtain no emulsification. I measured the interfacial tensions using two different Wilhelmy plates. Before utilisation of the platinum plate

(a)   (b)   (c)
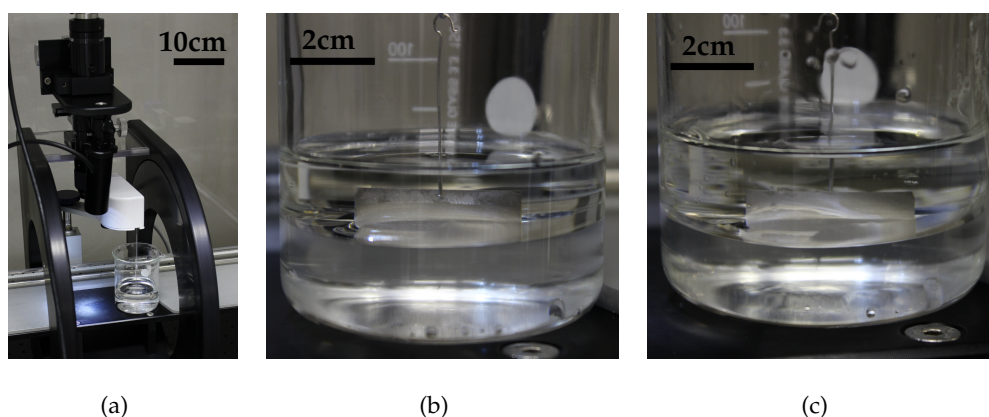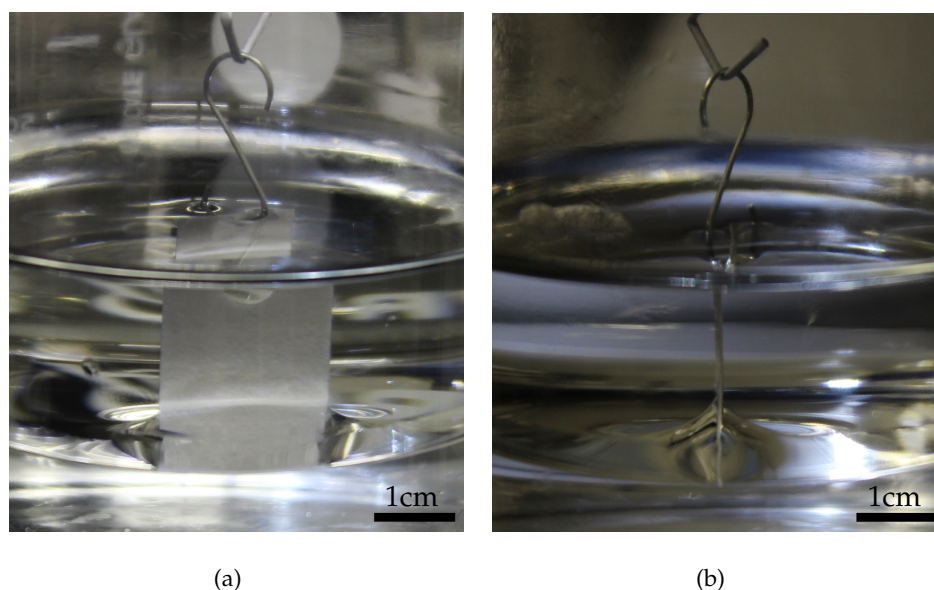
Figure 3.7: Langmuir trough setup used for the Wilhelmy plate method using a platinum plate. The bottom phase is millipore water, the top phase is squalane. (a) Setup, (b) Homogeneous and (c) inhomogeneous wetting of the plate.

(wetted length 39.24 mm, Fig. 3.7), I cleaned it with ethanol and then flame treated it. I shortened the paper plate (wetted length 20.60 mm, single-use only, Fig. 3.8) with cleaned stainless steel scissors (ethanol and flame treatment). After, having hung the plate on the scale, I zeroed the balance while it was totally immersed inside the non-wetting (non-aqueous) phase but as close to the interface as possible. I then lifted the scale so that the plate just touched the interface. Depending on the wetting phase, the meniscus pointed upwards or downwards. The absolute value of the force measured by the scale, gave the surface pressure and, thus, the interfacial tension. I recorded one value every 10 s. The first 100 s of the experiment were discarded as they correspond to the time taken to set up the experiment. For all concentrations, the experiments were equilibrated over several hours. For some concentrations (e. g. $C = 0.3$ µmol (KrytoxFSL)) no equilibrium was reached over 11 days.

I measured the time dependent interfacial tensions of two different systems (see Section 3.2). The first system was the surfactant KrytoxFSL in the fluorous phase, Novec7500, in contact with millipore water or PBS. The second system, I used, was oleic acid in squalane in contact with millipore water. I used the platinum Wilhelmy plate for the measurements of the interfacial tension with the interface between the fluorinated and the aqueous phase. I performed the measurements of the interfacial tension for the squalane water interface using the platinum and the paper plate. For the system with oleic acid, the platinum paper plate has shown wetting inhomogeneities (Fig. 3.7(c)) changing with each measurement (homogeneous: Fig. 3.7(b)) in contrast to a more homogeneous wetting with the paper plate (Fig. 3.8).

(a)   (b)

Figure 3.8: Langmuir trough setup used for the Wilhelmy plate method using a paper plate. The bottom phase is millipore water, the top phase is squalane with the contact lines seen from the front (a) and from the side (b).

From these measurements, I obtained the equilibrium interfacial tension, the interfacial coverage and the CMC. As described before (Sec. 2.4), the kinetic limited adsorption regime cannot be reached at these big scales. Thus, I developed a microfluidic system to approach the kinetic limited regime and I will describe this method in the following section.

3.3 Microfluidic adsorption measurements

I performed these measurements for the determination of the kinetics of surfactant adsorption in the adsorption limited regime. For the droplet-based microfluidic adsorption measurements, I produced water in oil emulsions using a dispersed aqueous and a continuous fluorous phase.

The aqueous phase consisted of a PBS buffer solution at pH ~7.3. To this PBS solution, I added the pH-sensitive dye (SNARF-1, 10 μM (6, 8 μM for test of ratio dependence), life technologies)[183] to obtain a concentration of 9.5 mM phosphate buffer and 10 μM SNARF-1. The dye has two different fluorescence maxima changing with pH (Fig. 3.9), measured with a home-built fluorescence bench using steps of 0.5 nm (Ocean Optics spectrometer, excitation with a green light-emitting diode, LED).
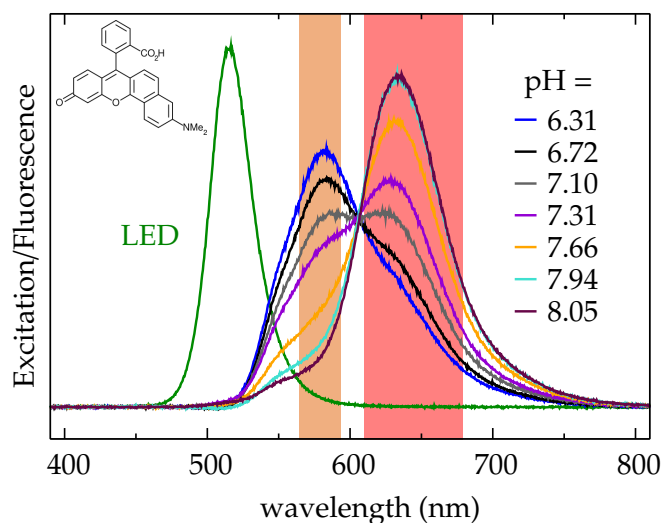
**Figure 3.9:** The intensity of the two fluorescence maxima of the dye, SNARF-1 (see inset), changes with changing pH when excited with green light (here: LED).

For the continuous phase, I used the fluorous solvent Novec7500 and the surfactant, KrytoxFSL, with varying concentrations of 0.01 mM, 0.03 mM, 0.05 mM, 0.10 mM, 0.20 mM, 0.29 mM, 0.39 mM, 0.49 mM, 0.59 mM, 0.69 mM and 2.0 mM. After the production of the droplets, the pH changes inside the aqueous droplets, due to the adsorption of the acidic surfactant from the fluorous phase. I used this pH change to obtain information on the kinetics of adsorption.

3.3.1 Fluorescence setup

To determine the pH inside the droplets at different positions in the microfluidic channel, I used a fluorescence setup[13] Fig. 3.10). The position on chip and the flow rate of the two phases determined the age of the droplet at which the pH was measured.

Before every new surfactant solution and set of pH measurements, I performed the following steps. I rinsed the device with the new surfactant solution and aqueous phase with 30 and 2.5 µL/min, respectively, for a minimum of 10 min. After, I set the flow for the pH measurements to the final flow rates of 7.5 µL/min and 1.5 µL/min for the fluorinated and the aqueous phase, respectively and waited another 10 min before data acquisition. I have chosen these flow rates as tipstreaming occurs upon increasing the flow rates (Sec. 2.6.2). This cleaning procedure is sufficient to clean the channels from previous solutions used, as no difference in signal is detected between repeated measurements. This means the
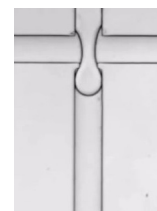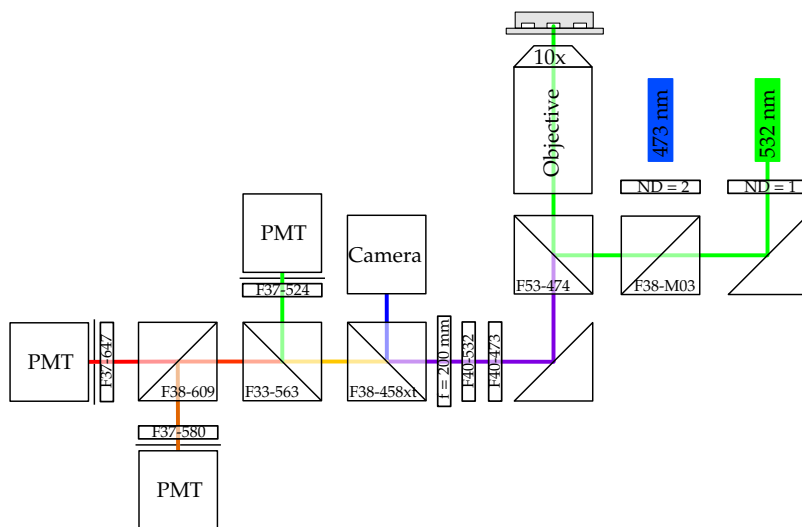
(a)
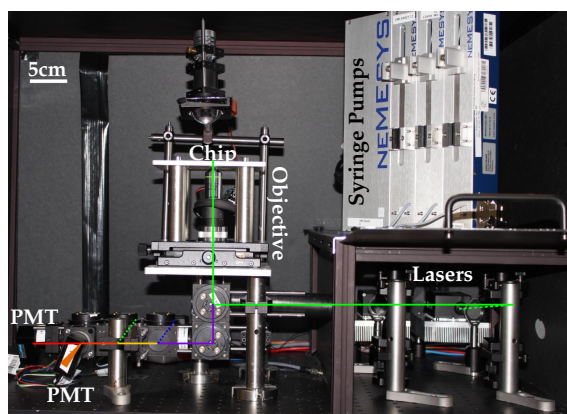
(b)
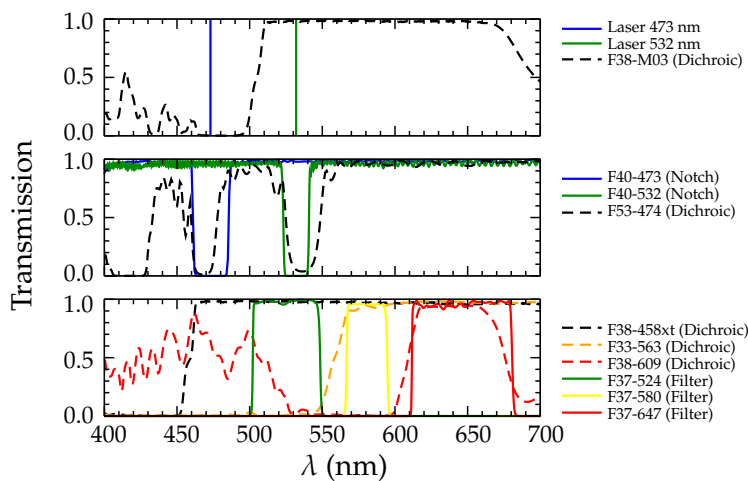
(c)

Figure 3.10: The fluorescence setup used for the pH analysis of the droplets produced in a microfluidic device. (a) The fluorescence setup including all optics. In my case, the 473 nm and the first PMT (for the green, F37-524) were not used. The microfluidic chip was positioned on top of the objective. (b) Photo of the fluorescence setup including the colour of the light which passes the optics described in (a). (c) The transmission data of all optics in (a).

measurement of an aqueous solution does not depend on what other aqueous solution with a different pH was used before. The pH values obtained after rinsing do not change with further cleaning.

I measure the pH using the pH-sensitive dye which exhibits two fluorescence maxima (around 647 nm and 580 nm, Fig. 3.9) depending on the concentration of protons present in the droplets. I measured the ratio of the fluorescence at higher wavelength to the fluorescence at lower wavelength using an optical setup, similar to that reported previously[13]. I used a laser (see Fig. 3.10, 532 nm, 25 mW, Cobolt Samba; the 473 nm was off in these experiments) which I directed through a neutral density filter (ND = 1, see Fig. 3.10, Thorlabs). I focussed the laser with an objective (10x, Olympus) into the microfluidic channels using dichroics (specification see Fig. 3.10 from AHF Analysentechnik, optical accessories from Thorlab). I mounted the microfluidic chip on a x-y-stage (Thorlabs). For focussing, I observed the droplets with a camera (Grashopper) using a blue LED (Olympus) from above. I turned the LED off for data acquisition of the fluorescence signal of the droplets. The dye in the droplets was excited by the 532 nm laser and the fluorescent light was directed through several notches and filters and split with dichroics (AHF Analysentechnik) to be recorded by photomultipliers (PMTs, H9656-20, Hamamatsu). In this experiment, only the voltages U of the two PMTs around 580 nm and around 647 nm were recorded (at gains of $G = 0.8$). The data were transferred by a FPGA board (cRIO, National Instruments) at 3kHz using a program written in LabView (National Instruments). The ratio from these two different PMTs was independent of the total intensity, making it more suitable for the analysis. I transformed the voltage U measured by the PMTs to the relative fluorescence unit[8] $RFU = U/G^{6.8}$. I recorded the signals from the PMTs for 2.73 s which equalled around 25 ± 5 droplets. Increasing this number does not give additional information meaning that 25 droplets are enough for the analysis.

3.4 Coalescence in microfluidics

The following experiments were developed previously[9] to study coalescence events in relation to the time of stabilisation. In this work, I correlate these data with the pH measurements to obtain the kinetics of surfactant adsorption. For these experiments,

---

[8]The exponent depends on the manufacturer. It was experimentally verified for these PMTs.
[9]These experiments were performed by Jean-Christophe Baret.
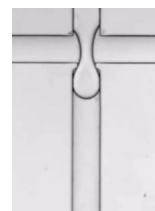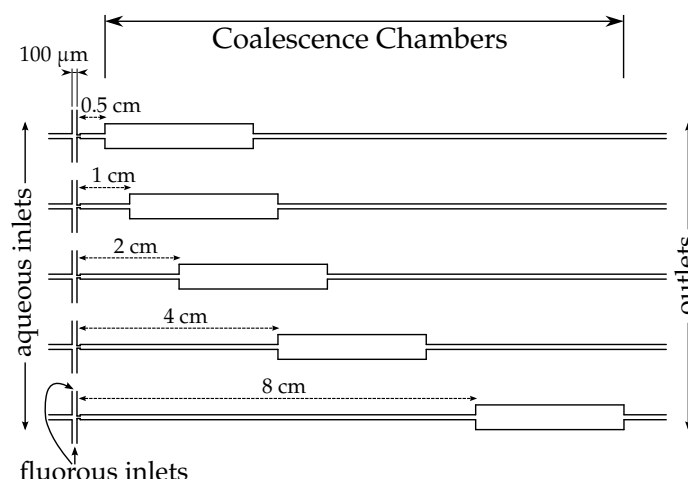
Figure 3.11: The design for the PDMS device for the coalescence experiments.

microfluidic chips with a coalescence chamber at different distances from the production were produced in PDMS (Fig. 3.11). The droplets were produced at the intersection of the aqueous and fluorous phase. Then, they passed the coalescence chambers at different distances from the production before they were collected at the outlets. The channel diameter was 100 μm and the width of the coalescence chamber is fivefold. The height of the channels was set to 40 μm. Videos with 2000 frames at a frame rate of 24 frames per second (fps) were recorded with a Phantom Camera (v210, Vision Research).

Additionally, I conducted coalescence experiments at equilibrium coverage to determine the concentration of surfactant at which a stable interfaces was obtained. I produced two aqueous interfaces in a microfluidic channel with a plug of a fluorous phase (as above) with concentrations of surfactant between 0.01 mM and 0.10 mM (as above). After a minimum of 5 min, I brought the two interfaces into contact (with the help of syringe pumps) to determine the time for coalescence to take place. Videos were recorded with a frame rate of 100 fps.

3.5 Synthesis of surfactant

The synthesis protocol was adapted from Holtze *et al.*[143][10] and Scanga *et al.*[184] and published by us in P. Gruner, B. Riechers *et al.*[61] (in press 2015). The synthesis was

---

[10]I did the original synthesis with Jean-François Bartolo in the group of Dr. Valerie Taly, Translational Research and Microfluidics, UMRS 1147, Paris Descartes University.

Figure 3.12: Synthesis of the PFPE-PEG-PFPE (KryCO-Jeffa-COKry) surfactant.

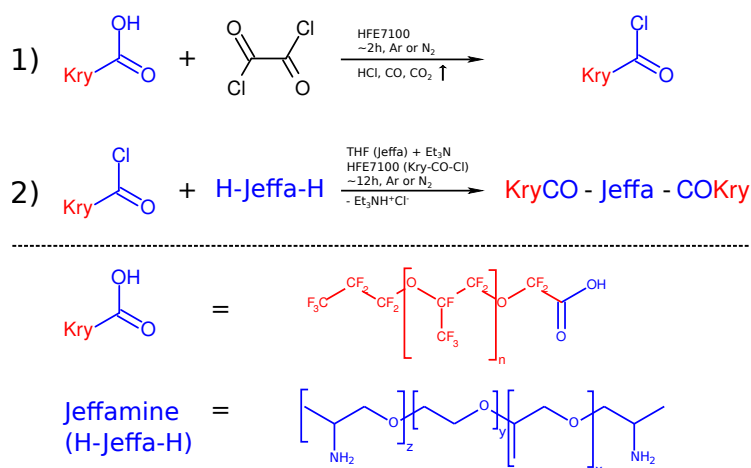improved[11] to overcome the difficulties of the surfactant being non-biocompatible and inducing leaking microreactors. In leaking droplets, the contents partition towards the oil phase or exchange with neighbouring droplets. I determined the molecular weight of the Krytox used by ^{1}H-NMR spectroscopy using a 1:1 mixture with Novec7500 (3M), and integrating the peak intensities of the protons of the ethoxy- and carboxylic acid groups (Sec. 3.2.1).

I used the following improved synthesis recipe following the scheme in Figure 3.12. The following steps were performed under inert atmosphere (Nitrogen or Argon, Fig. 3.13): I dissolved the Krytox 157 FSH (10.0 g, 2.50 mmol (1 eq), DuPont) in Novec7100 (30 mL, 3M; dried with 4 Å molecular sieves beads 8-12 mesh for one week) before injecting oxalylchloride (2.1 mL, 25 mmol (10 eq), Sigma Aldrich, reagent grade 98%) and one drop of dimethylformamide into the solution while cooling with ice. I stirred the reaction mixture until there was no further gas development. I evaporated all solvents and redissolved the product in Novec7100 (dried, 30 mL). I dissolved the O,O'-Bis(2-aminopropyl) polypropylene glycol-block-polyethylene glycol-block-polypropylene glycol 500 (Jeffamine, Sigma Aldrich, amounts see Table 3.3) in anhydrous Tetrahydrofurane (distilled, THF, 30 mL, Sigma Aldrich, ≥ 99.9%) and added Triethylamine (1.73 mL, 12.5 mmol (5 eq), Sigma Aldrich, ≥ 99%) to the solution. P_0 was synthesized using a similar scheme although without the drop of dimethylformamid (E. Mayot, private communication). Then, I injected the Novec7100 solution into the THF solution while stirring. The solution was

---

[11]I acknowledge the chemistry facility at the Max Planck Institute for Biophysical Chemistry, Göttingen, Germany, for letting me use their lab to perform the synthesis.
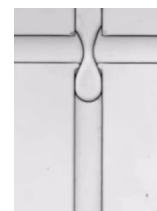
Figure 3.13: Schlenck line for the work under inert atmospheric conditions (contrast, colors enhanced, sharpened).

Table 3.3: Amounts of Jeffamine used for the different synthesis. P_0 was performed by E. Mayot with the same conditions as $P_{4,5}$.

Synthesis	mass	volume	amount	equivalents to KrytoxFSH
P_1, P_2	0.40 g	0.38 mL	0.67 mmol	0.27 eq
P_3	0.85 g	0.82 mL	1.42 mmol	0.57 eq
P_4, P_5	0.75 g	0.73 mL	1.25 mmol	0.50 eq

stirred overnight. At the end, the product was stable to be handled under atmospheric conditions.

I performed a control synthesis according to the previous protocol, where the THF solution was briefly opened to air before it was added to the Oxalylchloride which had reacted with the Krytox (C_1). This has shown the crucial role of the inert atmosphere and the dry solvents on the synthesis.

For the purification, I evaporated all solvents and redissolved the product in FC3283 (30 mL, 3M). I filtrated (1x (2x does not increase the purity)) and washed (3 x 25 mL) it over Celite® 545 (Sigma Aldrich) using a glass frit (porosity 2) before I dried it under vacuum. I obtained the final milky semi-solid product with yields of 50-90%. The variation is due to the filtering, as product is being trapped in the frit. This is seen in the fact that filtering twice reduced the yield by about 30 % as the product is trapped in the frit. However, this does not increase the purity. Furthermore, the yield depends on the

amount of Novec7500 used to wash with 3 x 25 mL being a rough estimate for high yield and good purity.

3.5.1 Further purification

Additional to the purification of the surfactant using Celite® 545, I used silica beads functionalised with an amine group.[12] I produced them as follows. I cleaned silica beads (diameter 30 μm, AEROPERL®, Evonik) using 100 mL Piranha Etch (80 mL H_2SO_4 with 20 mL H_2O_2) for 20 min. Then, I introduced these beads into H_2SO_4 (95-98%, ACS reagent, Sigma Aldrich) before adding H_2O_2 (30 w%, ACS reagent, Sigma Aldrich). For neutralisation, I added 2 L of water to the solution. After sedimentation, I discarded the supernatant and I centrifuged the sediment layer at 3500 rpm (rounds per minute) (Thermo Megafuge 16R, rotor falcon size) for 10 min. I removed the supernatant and dried the beads over night. I added the beads to a solution of 1% (v:v) (3-Aminopropyl)triethoxysilane (≥ 98%, Sigma Aldrich) in Toluene (≥ 99%, Merck KGaA) and stirred them for one hour before decanting the supernatant and washing the beads three times with 50 mL of Ethanol (Uvasol for sepctroscopy, Merck KGaA). I recovered the sediment layer and centrifuged as mentioned above before drying the beads in an oven over night (80°C, Dry-Line DL53, VWR).

Finally, I mixed these beads (2 g) with the surfactant solution (6 mL of 1 w% in FC40 (Iolitec)) before adding further FC40 (1 x or 2 x 6 mL). I filtered (Whatman® Grade1, Sigma Aldrich) this mixture before performing ^{1}H-NMR for quantitative analysis[13] [185].

3.5.2 Infrared spectroscopy

To characterise the surfactant purity, I measured infrared spectra on a Fourier-transform infrared (FT-IR) spectrometer (Nicolet 6700 FT-IR, software OMNIC 8.2, Thermo scientific) with a resolution of 1 cm^{-1} and an average of 16 scans in a range of 4000 - 400 cm^{-1} using a KBr cell and the surfactants without any solvents.

---

[12]The functionalisation was done with the help of Julie Murison at the Max Planck Institute for Dynamics and Self-Organization.

[13]NMR analysis performed by Philipp Gruner, Max Planck Institute for Dynamics & Self-Organization.
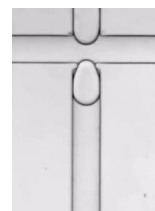
3.5.3 Partitioning experiments

I used all synthesised surfactants including the KrytoxFSL for partitioning experiments. I prepared 500 µL of 0.5 w% or 1 w% of surfactant solution and 500 µL of 100 µM of Rhodamine 6G (95%, Sigma Aldrich) and layered the two phases keeping them in contact for a minimum of 72 h. I measured the absorbance spectra of both phases in the visible region (VIS) using the microplate reader SpectraMax (1P-Tune 4 SpectraMax Paradigm, software SoftMaxPro 6.2.2, Molecular Devices). I detected the absorbance (Absorbance Monochromatic Illumination, Absorbance Photo Diode Detection Cardridge) of 100 µL of solution in the range of 350 - 750 nm with steps of 1 nm using a 96-well microplate (black, clear bottom, Microtest™, Optilux™, BD Falcon™, BD Biosciences).

Summary of Chapter 3 – Technical Aspects

I adapted a protocol to manufacture PMMA devices in complement to the PDMS devices typically used. For a full control of the surfactant quality, I have performed and improved the synthesis of the surfactant PFPE-PEG-PFPE. I have characterised the physical-chemistry of the surfactant-oil-system applying standard techniques. Finally, I have developed a method for miniaturised pH measurements at the millisecond time scale adapted to the kinetics of surfactant adsorption in droplets.

Chapter 4

Surfactants and Adsorption Kinetics

Parts of this chapter are included in P. Gruner, B. Riechers *et al.*[61] (in press 2015) and B. Riechers *et al.*[43] (in preparation 2015).

4.1 Surfactant chemistry

In this section, I characterise the surfactants, which I use for the different experiments, using bulk methods. In a first step, I obtain the molecular weight of Krytox (FSL, FSH) from nuclear magnetic resonance spectroscopy and mass spectrometry. In the second step, I determine the interfacial tensions in relation to the concentration of the surfactants (Krytox FSL, oleic acid) from which I identify the value of the CMC.

4.1.1 Determination of the molecular weight

As stated in the literature[143], the molecular weight of the KrytoxFSL (Krytox FSH see Sec. 4.3.1) varies from the value given the supplier. For my experiments, it is crucial to know the molecular weight. I use ESI-MS[1] and ^{1}H-NMR spectroscopy for its determination (Sec. 3.2.1). Assuming, all the peaks visible in the mass spectrum contain a carboxylic endgroup, the molecular mass of the KrytoxFSL is 1634 g/mol (see Fig. 4.1(a)). To confirm

---

[1]This measurement was performed by Uwe Pleßmann, member of the research group of Henning Urlaub: Bioanalytical Mass Spectrometry from the Max Planck Institute for Biophysical Chemistry
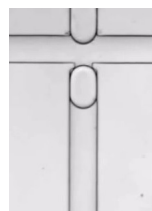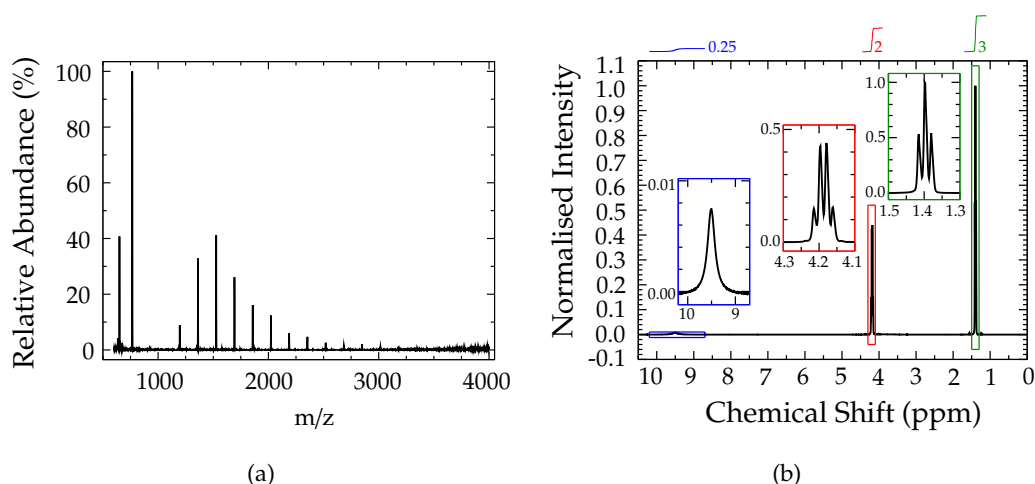
Figure 4.1: Determination of the molecular weight of the carboxylic acid KrytoxFSL used for the kinetics experiments. (a) ESI-MS spectrum of KrytoxFSL, (b) ^{1}H-NMR of a solution of 1:1 (w/w) of KrytoxFSL and Novec7500. To obtain the molecular weight, the integrals of the triplet and the quartet from the ethoxy group are put in relation to the integral of the singlet from the carboxylic endgroup.

Figure 4.2: The chemical structures of Krytox and Novec7500 for the determination of the number of repeating units, *n*, in Krytox.

this observation, I measured the ^{1}H-NMR spectrum[2] of a 1:1 mixture of KrytoxFSL with Novec7500 to elucidate the structure and determine the relative amount of carboxylic acid groups (Fig. 4.2). The proton of the carboxylic acid shows a sin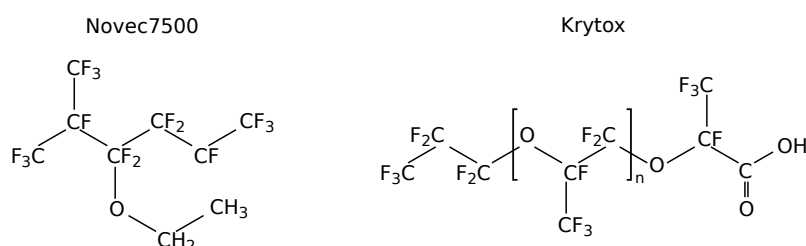glet with a chemical shift, δ, of 9.50 p.p.m. (parts per million)[155]. On the other hand, the ethoxy group of the Novec7500 shows a triplet and a quartet with a chemical shift centred at 1.40 and 4.18 p.p.m., respectively. The singlet has an integral of 0.25 ± 0.01 as compared to the triplet and quartet with integrals of 3 and 2 ± 0.03, respectively. Taking the molecular weight of the solvent Novec7500 (414 g/mol) and the weight ratio of the two components into account, the determined molecular mass is 1659 ± 67 g/mol (Fig. 4.1(b)). Thus, the mean value of the determined molecular mass by both methods (NMR and ESI) is

---

[2]This measurement was performed with the help of Elias Akoury within the research group of Markus Zweckstetter, Structure Determination of Proteins Using NMR, at the Max Planck Institute for Biophysical Chemistry.

1646 g/mol with 7.9 of the repeating units n (Fig. 4.2). I assume an error of 67 g/mol, referring to the error in the analysis of the NMR data.

4.1.2 Tensiometry

In this part, I describe the analysis of the surfactant with standard tensiometric techniques (Sec. 2.3). I am analysing interfacial tensions between a solution with a surfactant with a carboxylic headgroup and an aqueous phase consisting either of millipore water or of the PBS solution using the pendant drop and the Wilhelmy plate method.

For these two systems, I plot the change of the interfacial tensions γ with time in Figure 4.3 with millipore water in (a) and PBS in (b). The equilibrium interfacial tension is reached faster, the higher the surfactant concentration is. Furthermore, this equilibrium is lower for higher surfactant concentrations. Thus, the interfacial tension data show that increasing the concentration of surfactant in the bulk phase, increases the adsorption speed of surfactant to the interface and increases the number of molecules covering the surfactant molecules at equilibrium. The surfactant I use is a carboxylic acid, which can deprotonate upon the contact with water and becomes then a charged surfactant. If millipore water is used as the aqueous phase, there is electrostatic repulsion between the surfactant molecules upon adsorption and the adsorption cannot be seen as a simple Langmuir adsorption process[2,39]. Additionally, less molecules adsorb to the interface than in the case where the charge is screened with a counter ion, like in (b) with Na^+ from the PBS. Furthermore, I measured the interfacial tension using a droplet of the surfactant solution in the aqueous phase. This is of importance as the concentration of the surfactant inside the droplet can change upon adsorption, depending on the concentration of the surfactant solution and the size of the droplet. The droplet size for the pendant drop experiments at small concentrations is ~10 μL with a droplet interfacial area of ~5 mm^2. With a maximum interfacial coverage of 8 μmol/m^2 (see determination using the Wilhelmy plate method), the surfactant molecules at the inside of the droplet are completely depleted up to a concentration of 40 μmol/L. Even if the interfacial coverage is only one tenth of the maximum coverage, the measurement of the kinetics at low concentrations is deficient. This is due to the fact that the molecules need to diffuse from the tubing which leads to much higher equilibration times and different kinetics. Additionally, the
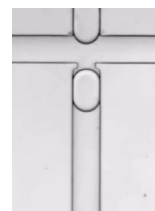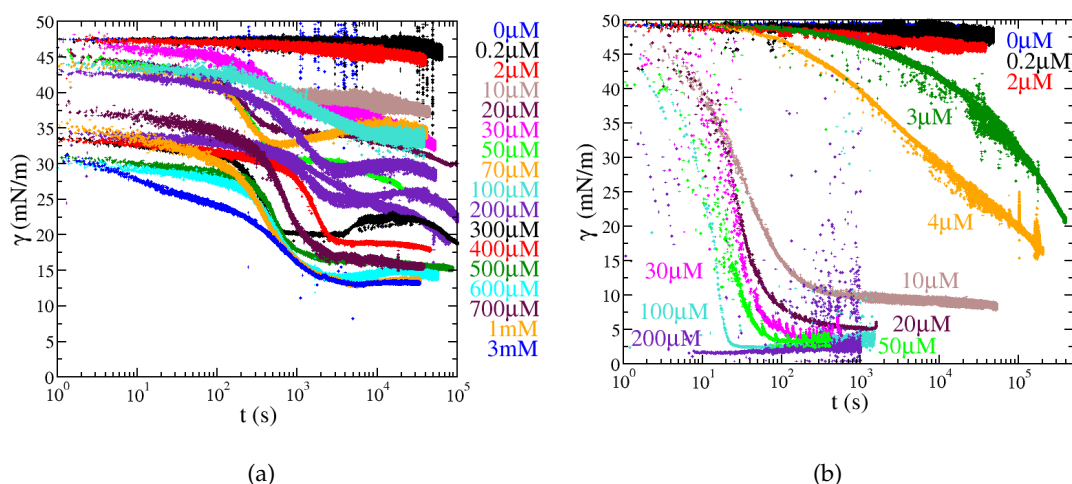
Figure 4.3: The interfacial tensions of the surfactant solutions (KrytoxFSL) with (a) millipore water or (b) PBS as the aqueous phases measured using the pendant drop method. The label shows the concentration of the surfactant inside the fluorous phase Novec7500.

assumption that the bulk surfactant concentration stays constant does not hold. Thus, no further analysis is performed for the pendant drop data.

In contrast, the Wilhelmy method, for which a planar interface is examined, gives more promising results (Fig. 4.4). Here, I show the change in interfacial tension with time using different concentrations including the plot of the equilibrium values in relation to the concentration. Upon fitting these data (Fig. 4.4(b), Eq. 2.22), I obtain the interfacial tension without surfactant, γ_0, the maximum interfacial coverage, Γ_∞, as well as the critical micellar concentration (CMC) and the value κ described in Section 2.4.2.

The variation of interfacial tension of this surfactant spans almost two orders of magnitude, making it difficult to study. Additionally, a great disadvantage of both tensiometric measurements is the long equilibration times due to the large volumes used[40] which means that the classical methods are not convenient. Furthermore, surfactant adsorption at these big length scales is diffusion limited and does not provide information on the adsorption kinetics of small length scales (Sec. 2.4)[41]. Thus, I analyse the adsorption kinetics using droplet-based microfluidics (see Section 4.2).
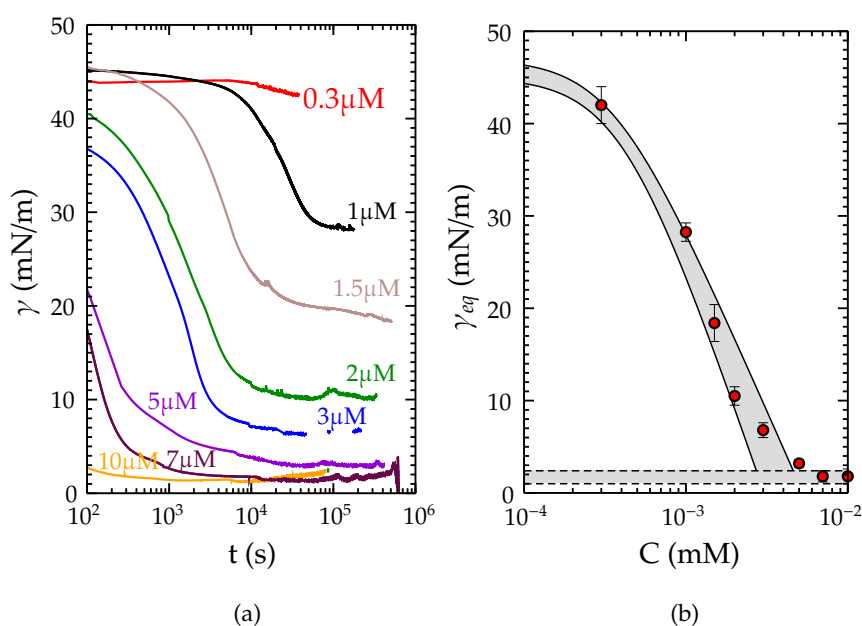
Figure 4.4: The interfacial tension of different concentrations of the surfactant solutions (KrytoxFSL) in contact with a PBS solution, measured using the Wilhelmy plate method. (a) Time traces of the interfacial tension of different surfactant concentrations (see label). (b) Fit of the data using Eq. 2.22 to obtain $\gamma_0 = 46 \pm 1$ mN/m; $\Gamma_\infty = 8 \pm 1$ μmol/m^2 ; $\kappa = 7 \pm 1 \times 10^6$ m^6/mol^2; CMC = 4 ± 1 μmol/L.

Summary of Section 4.1 – Surfactant Chemistry

I used mass spectrometry and nuclear magnetic resonance spectroscopy to determine the molecular mass of a carboxylic acid surfactant. Additionally, I characterised the surfactant by measuring the interfacial tensions between aqueous phases and fluorous phases in which the surfactant was dissolved. These measurements show (i) the importance of buffer conditions on adsorption kinetics, (ii) the importance of charge screening for the effective adsorption of surfactants with charged headgroups and (iii) the long equilibration times of the interfacial tension using standard bulk methods (Wilhelmy plate, pendant drop).

In the following, I will be using aqueous solutions containing buffers. Charges from surfactants at the interface will be screened by the ions dissolved in the bulk. Electrostatic barriers for adsorption will therefore be neglected and the surfactant (charged and uncharged) will be treated as a neutral surfactant as long as adsorption is considered.
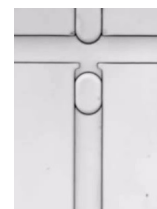
4.2 Adsorption kinetics at the micron scale

To obtain information on the kinetics of adsorption to droplets in microfluidics, I used an acidic surfactant which adsorbs to the interface upon droplet production (Sec. 3.3). Upon adsorption, it deprotonates changing the pH inside the aqueous droplets. I use a fluorescence setup to measure the fluorescence of a pH sensitive dye inside the droplets which displays the amount of protons added. A long microfluidic channel serves for a good time resolution of the pH change.

In the first part, I describe the calibration of the system which includes the titration of the buffer solution and the determination of the pH in droplets inside microfluidic channels. I describe the analysis of the data in a second step before obtaining the change of the proton concentration with time and with surfactant concentration. The data differ from a simple first order Langmuir adsorption model. Thus, I develop a new second order adsorption model which I then test for the description of the bulk equilibrium data and on the impact on coalescence.

In the experiments, which I will describe in the following, I used a PMMA device with long microfluidic channels. In contrast to PMMA, PDMS cannot be used as it delaminates due to the high pressures which build up inside these long microfluidic channels. Moreover, I could not obtain a stable droplet production without the use of surfactants when using PDMS, due to the deformation of the channels (Sec. 3.1).

4.2.1 Calibration of the setup

For the determination of the kinetics of the adsorption of surfactants to the interface, I measure the change of fluorescence due to the change in pH. Furthermore, I am interested in the amount of protons added to the aqueous phase upon a measured pH change. In the following section, I calibrate these two relations.

First, I determine the change of pH upon titrating the buffer solution with HCl (black points in Fig. 4.5, Sec. 3.2.2). I calculate the change of pH (black line) using the equilibration constants of the three equilibria of the triprotic phosphoric acid from PBS (Appendix B). The theoretical and experimental data are in very good agreement. Therefore, I use the
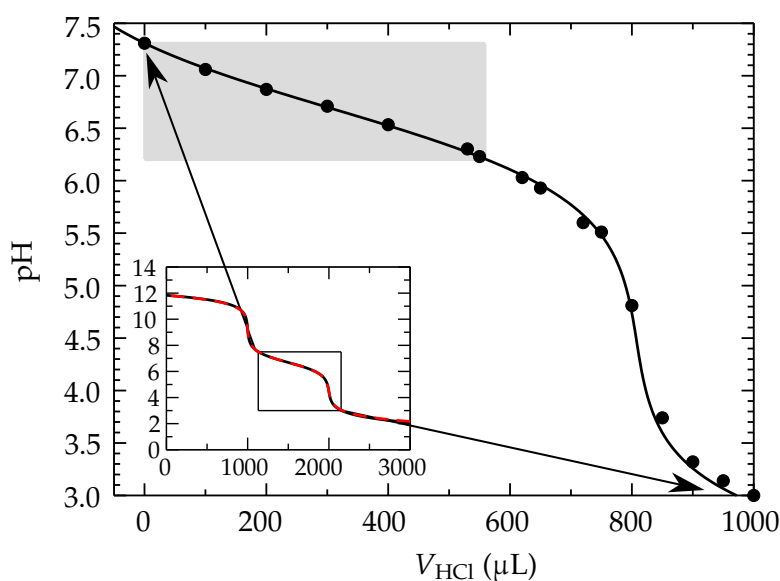
Figure 4.5: pH change with addition of HCl (titration (black circles) and calculation with (black line) and without dilution (red line)).

theoretical calculation in the following. When a titration is performed, it is never possible to only add protons which means the solution is always diluted. Within the microfluidic pH experiment, only protons are added to the aqueous phase and no dilution of the droplets takes place. Thus, I calculate the change of pH assuming that no dilution takes place (red line in Fig. 4.5, Eq. B.40)[186,187]. I then use these values (grey shaded area in Fig. 4.5) to determine the amount of protons added to the droplets in relation to the change in pH (Fig. 4.10), even though there is only a small difference between the amount of protons with and without dilution.

Second, I use a pH-sensitive dye to determine the pH inside the droplets at different positions inside the microfluidic channel using a fluorescence setup (Sec. 3.3).
At slow velocities, the fluorescence inside a microfluidic channel is influenced by the droplet's speed as bleaching can take place[22]. Directly after production, the droplet accelerates to a terminal velocity[22]. The calibration is performed where the droplets have reached this terminal velocity (9.8 mm ≡ 0.5 s after production) known from the time the droplet passes the laser spot. I use the same flow rates for all experiments to make sure this does not influence the results[22]. The velocity is calculated using the flow rates and the channel dimensions to be 19.6 mm/s (see Sec. 5.1.2).
In the experiment, I measure the ratio, *Rat*, of the fluorescence at two wavelengths changing with pH (Fig. 4.6). This ratio does not depend on the concentration of the dye (6 to
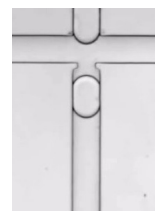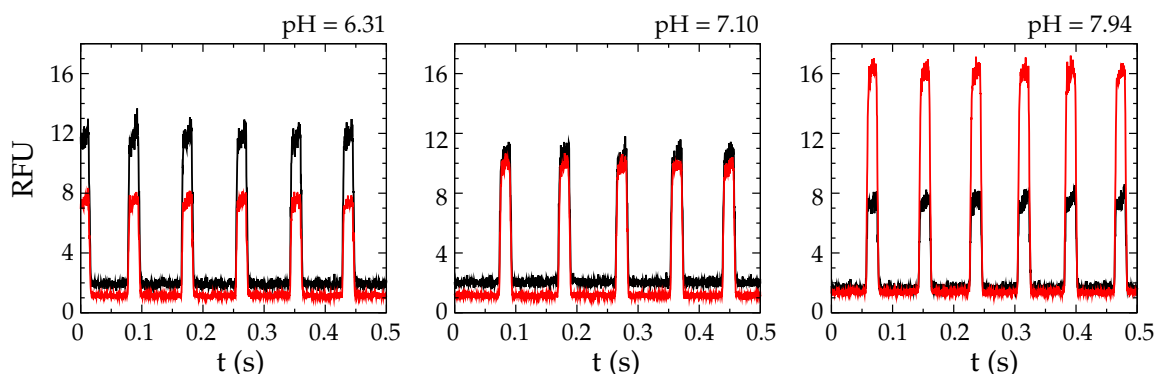
Figure 4.6: Fluorescence intensity (relative fluorescence units, RFU) of the different photomultipliers (PMTs) at higher (647 nm, red line) and lower (580 nm, black line) wavelength for different pH values of the aqueous phase.
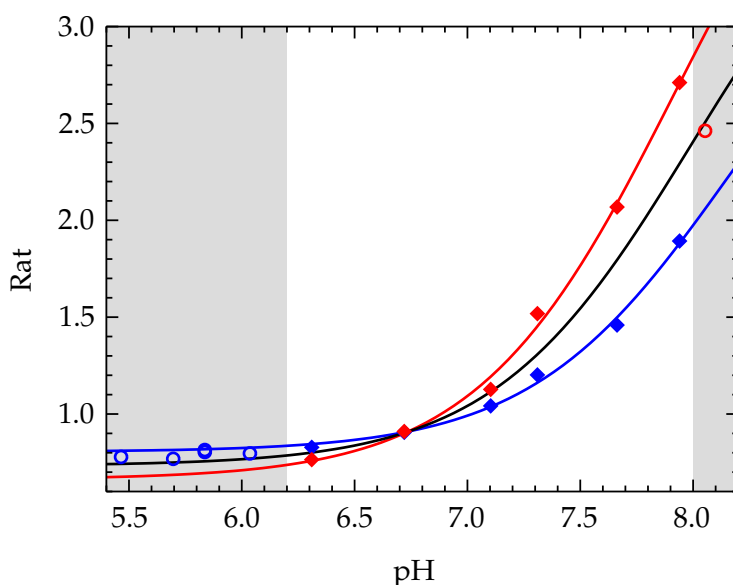
Figure 4.7: Calibration of the ratio of the fluorescent signals (high/low wavelength) in relation to the pH of the original solution (repetitions (red diamonds, blue circles) and mean (black)). Values for the fit not considering the open symbols: black: $A_0 = 4.1$, $A_1 = 0.73$, $A_2 = 0.33$; blue $A_0 = 3.6$, $A_1 = 0.80$, $A_2 = 0.23$; red $A_0 = 4.6$, $A_1 = 0.66$, $A_2 = 0.38$.

10 µM). Thus, the small leakage of the dye towards the oil phase does not change the results. I calibrate this relation using PBS solutions including the dye at different pH values. The fluorous phase contains a non-zero surfactant concentration of 0.02 mM of surfactant. The pure fluorous phase cannot be used as the dye has a slight interfacial activity leading to an adsorption of the dye to the interface when the surfactant concentration is too low. The ratio of the fluorescence intensities (signal at higher divided by signal at lower wavelength) increases with increasing pH (Fig. 4.6, 4.7) and the pH measurement is sensitive and reliable in the range between 6.2 and 8.0 (Fig. 4.7)[183]. I obtain the dependence between the Ratio and the pH by fitting with $Rat = (A_1 \cdot 10^{pK_a - pH} + A_0 \cdot A_2)/(A_2 + 10^{pK_a - pH})$

using the dissociation constant for SNARF-1[3] pK_a = 7.5. For the small concentration of surfactant which I used for the calibration, no pH change is detectable. Additionally, a non-ionic surfactant does not show a change in pH. As I use the ratio of the fluorescence, my measurements are independent on small variations in absolute intensity as well as on a small leakage of the dye towards the fluorous phase.

4.2.2 Data processing

I show the raw data of the PMTs in Figure 4.6. I process these data (using MATLAB) to obtain the calibration curve (Sec. 4.2.1). In the pH measurements, I invert this curve to obtain the pH from the measured ratio. For the processing of the data for the calibration and the pH experiment, I use the mean of the droplet signal to obtain the ratio of the two PMTs. The threshold above which I define the droplets is at 35% of the difference between the maximum and the minimum value per experiment of each PMT. Due to the small leakage of the dye, the measured fluorescence of the continuous phase (which should be non-existent) increases slightly with the age of the continuous phase. As the baseline changes with this value, it is not subtracted during data treatment. I obtain a ratio of the fluorescence signal which I convert into a pH using the three calibration curves (Fig. 4.7). The error bars for the pH in Fig. 4.8 are due to this calibration. I relate the pH to a concentration of protons inside the droplet using the theoretical calculation developed in Section 4.2.1. I obtain the age of the droplet from the distance to the production, the channel dimensions and the flow velocity. The time frame for the determination of the kinetics from these experiments is between 0.8 and 30 s due to the acceleration of the droplet to a final velocity (Sec. 4.2.1) and the length of the microfluidic channel (Fig. 3.3).

4.2.3 Change in proton concentration

I determine the change in pH with time (position on chip) for the different concentrations of surfactants used (Fig. 4.8). For a given surfactant concentration (C = 0.49 mM), the pH decreases from 7.5 to 6.8. The typical timescale of the process is ~2 seconds. Qualitatively, this variation of pH corresponds to the transfer of 4 mmol/L protons from the fluorous

---

[3]Obtained from $pH = pK_a - log\left((Rat - A_0)/(A_1 - Rat) \cdot A_2\right)$, information from Molecular Probes.
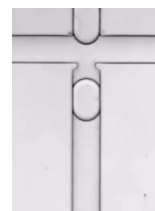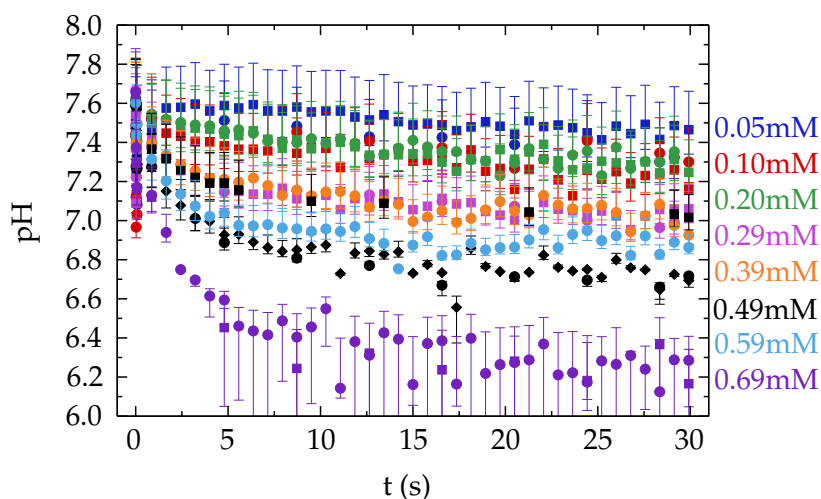
Figure 4.8: pH change with time for surfactant concentrations of 0.05 mM (blue), 0.10 mM (red), 0.20 mM (green), 0.29 mM (pink), 0.39 mM (orange), 0.49 mM (black), 0.59 mM (light blue) and 0.69 mM (purple). The errorbars show the uncertainty due to the calibration of the ratio of the signals versus the pH.

towards the aqueous phase. Increasing the surfactant concentration in the fluorous phase has two effects: the pH decreases to a smaller equilibrium value and the timescale of the process is shorter. The error bars result from the calibration of the change in ratio with pH (Sec. 4.2.1). These errors become less relevant for the following analysis as I only need to consider changes of pH and not absolute values.

All the concentrations, I use here, are above the CMC (Sec. 4.1.2) meaning that the equilibrium coverage is constant for all concentrations. But as the equilibrium pH is a function of the surfactant concentration, I can conclude that it is not limited by the adsorption of the first monolayer to the interface. Indeed in such a case I expect that the surfactant maximum coverage would determine the pH variation. Therefore, the additional exchange of protons occurs while the interface is at equilibrium coverage, through the desorption of the surfactant and the subsequent adsorption of other surfactant molecules. The surfactant desorption involves the extraction of a counter ion from the aqueous phase. The overall process can therefore be modelled as:

$$KryCOOH_{fl} \rightleftharpoons KryCOO^-_{int} + H^+_{aq}$$

$$KryCOO^-_{int} + Na^+_{aq} \rightleftharpoons KryCOONa_{fl}$$
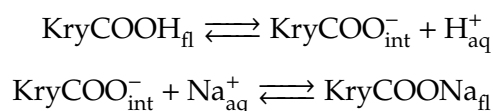
with the assumption that the dissociation of the carboxylic acid and the diffusion of the protons inside the aqueous phase are instantaneous compared to the adsorption of the

surfactant[188]. *fl* refers to the oil phase, *int* to the interface and *aq* to the aqueous phase. Considering the typical ion concentration in the droplets and KrytoxFSL being a strong acid, the extraction of the Na^+ ions is the most likely event.

4.2.4 Failure of the Langmuir adsorption model

I now quantitatively analyse the reaction rate, the equilibrium of the reaction and the order of the reaction. With this, I fully analyse the kinetics of proton transfer from the fluorous phase to the aqueous phase.
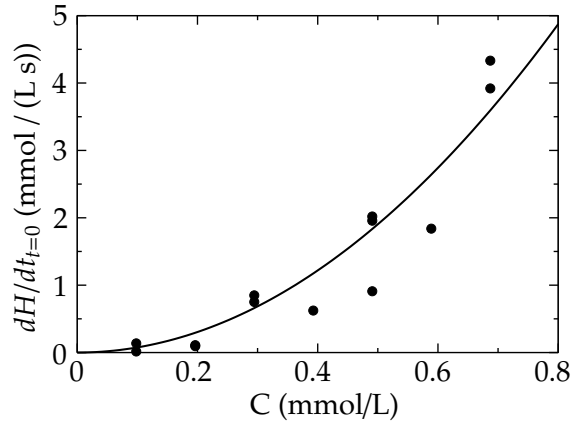

Figure 4.9: Speed of the reaction at time zero for all different concentrations of surfactant used.

The initial reaction rate is not linear with concentration (Fig. 4.9). This result is not compatible with the Langmuir process. I assume in a first step, though, that the adsorption of surfactant follows a standard Langmuir process. The rate of adsorption $\partial \Gamma / \partial t$ is proportional to the concentration of surfactant in the bulk C_0, the density of the available sites at the interfaces $\Gamma_\infty - \Gamma$, and the adsorption constant k_{ads}. The desorption process is proportional to the density of occupied sites Γ and the desorption constant k_{des}.

$$\frac{\partial \Gamma}{\partial t} = k_{ads} C_0 (\Gamma_\infty - \Gamma) - k_{des} \Gamma \tag{2.20}$$

This relationship leads to an exponential relaxation of the interfacial coverage as $\Gamma(t) = \Gamma_{eq} (1 - \exp(-t/\tau))$ with $\tau^{-1} = k_{ads} C_0 + k_{des}$, and to an equilibrium interfacial coverage of $\Gamma_{eq} = \Gamma_\infty \kappa C_0 / (1 + \kappa C_0)$ (Eq. 2.21, Appendix C.1) with $\kappa = k_{ads}/k_{des}$. In this model, one proton is released in the bulk for each surfactant molecule adsorbing. At short timescales, when the coverage is much smaller than the equilibrium coverage, mass conservation implies that $\partial_t \Gamma \cdot S = \partial_t [H^+] \cdot V$, where S and V are the surface and volume of the droplet,
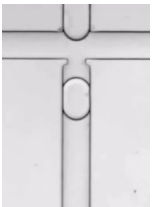
respectively. At longer times, the concentration of the acidic surfactant in the oil decreases. Thus, the full rate equation for the proton concentration in the droplet reads:

$$\frac{V}{S}\frac{\partial[H^+]}{\partial t} = k_{ads}(C_0 - \frac{1}{q}[H^+]) \cdot (\Gamma_\infty - \Gamma) \,. \tag{4.1}$$

q is the volumetric ratio between the fluorous and the aqueous phase which accounts for dilution effects. If all H^+ are transferred from the oil to the water, the concentration in the water is simply qC_0. In the desorption process, the counter-ion that leaves the droplet from the bulk is likely the most abundant positive ion. In this case, a Na^+ ion is transferred to the oil. Hence, the rate equation for the H^+ in the droplet does not take into account the desorption process.

Solving the equation requires the knowledge of $\Gamma(t)$. However, when the timescales for surfactant adsorption and pH change are well separated, one can assume that the interface is at equilibrium coverage Γ_{eq} at all times of the pH change. Only the knowledge of Γ_{eq} is required to solve Eq. 4.1. In this case, the relaxation is again exponential and the timescale of pH change is simply

$$\tau_{pH} = \frac{q\,R}{3k_{ads}(\Gamma_\infty - \Gamma_{eq})} \tag{4.2}$$

with R being the radius of the droplets. The initial velocity of the decay of the H^+ concentration $\partial H^+/\partial t|_{t=0}$ in the droplet is thus expected to be linear in surfactant concentration (Eq. 4.1).

Experimentally, I find a square dependence of the initial rate indicating that the adsorption process does not follow a simple Langmuir process. The dependence of the initial reaction rate with the concentration requires that the adsorption is of second order and is therefore described accordingly. I construct a consistent model for the adsorption process and for the pH variation process based on my experimental observations. I will show that the model captures quantitatively the dynamics of pH variation and of the adsorption process. I infer from the pH kinetics the interfacial parameters required to quantitatively determine the adsorption process.

4.2.5 Second order adsorption model

The first approach to describe the second order kinetics is to assume that the rate of proton transfer is proportional to the concentration of surfactant to the square. In addition, it is still necessary to have empty sites at the interface for adsorption to take place. Hence, I propose a rate equation of the form:

$$\frac{1}{2}\frac{V}{S}\frac{\partial[H^+]}{\partial t} = k_{ads}(C_0 - \frac{1}{q}[H^+])^2 \cdot (\Gamma_\infty - \Gamma) \tag{4.3}$$

with k_{ads} in relation to the increase of proton concentration. For consistency in the model, and because there is no physical reason to assume that the H^+ transfer is independent on the adsorption of surfactant, the straightforward model for adsorption is:

$$\frac{1}{2}\frac{\partial\Gamma}{\partial t} = k_{ads}C_0^2 \cdot (\Gamma_\infty - \Gamma) - k_{des}\Gamma \ . \tag{4.4}$$

Using the assumption that I have a separation of timescales between the adsorption process and the pH change in the droplet, the interface is quickly reaching equilibrium while the pH is slowly changing. Therefore as previously, the pH change occurs for $\Gamma = \Gamma_{eq}$. Eq. 4.3 is a second order kinetic law leading to the $[H^+]$ variation as (Appendix C.2):

$$\Delta[H^+] = \Delta[H^+]_{eq}\left(1 - \frac{1}{1 + t/\tau_{pH}}\right) \tag{4.5}$$

with

$$\tau_{pH} = \frac{q\,R}{6k_{ads}C_0(\Gamma_\infty - \Gamma_{eq})} \ . \tag{4.6}$$

To quantitatively check the validity of the model, I have fitted all experimental values (Fig. 4.10(a)-(h)) with Eq. 4.5 using the $\Delta[H^+]_{eq}$ and τ_{pH} as fitting parameters. Firstly, I find that the equilibrium value $\Delta[H^+]_{eq}$ scales linearly with the concentration of the surfactant (Fig. 4.10(i)). This result implies that there is a full release of protons from the oil to the droplet, even if the interface is at equilibrium. Second, I find that the timescale of the process scales as $1/C_0$ as expected for a second order process. Combining these results, I recover that the initial speed of the reaction scales as C_0^2. In principle, for a full transfer of protons from the oil to the droplet, I expect $\Delta[H^+]_{eq} = qC_0$ where q is the ratio of the oil to water volume fractions. Experimentally, I find that this ratio is ~8 while I impose a ratio of flow rates of 5. The error might come from the difficulty to determine accurately the concentration of the carboxylic acid polymer. However, the experimental data are in good quantitative agreement with my model.
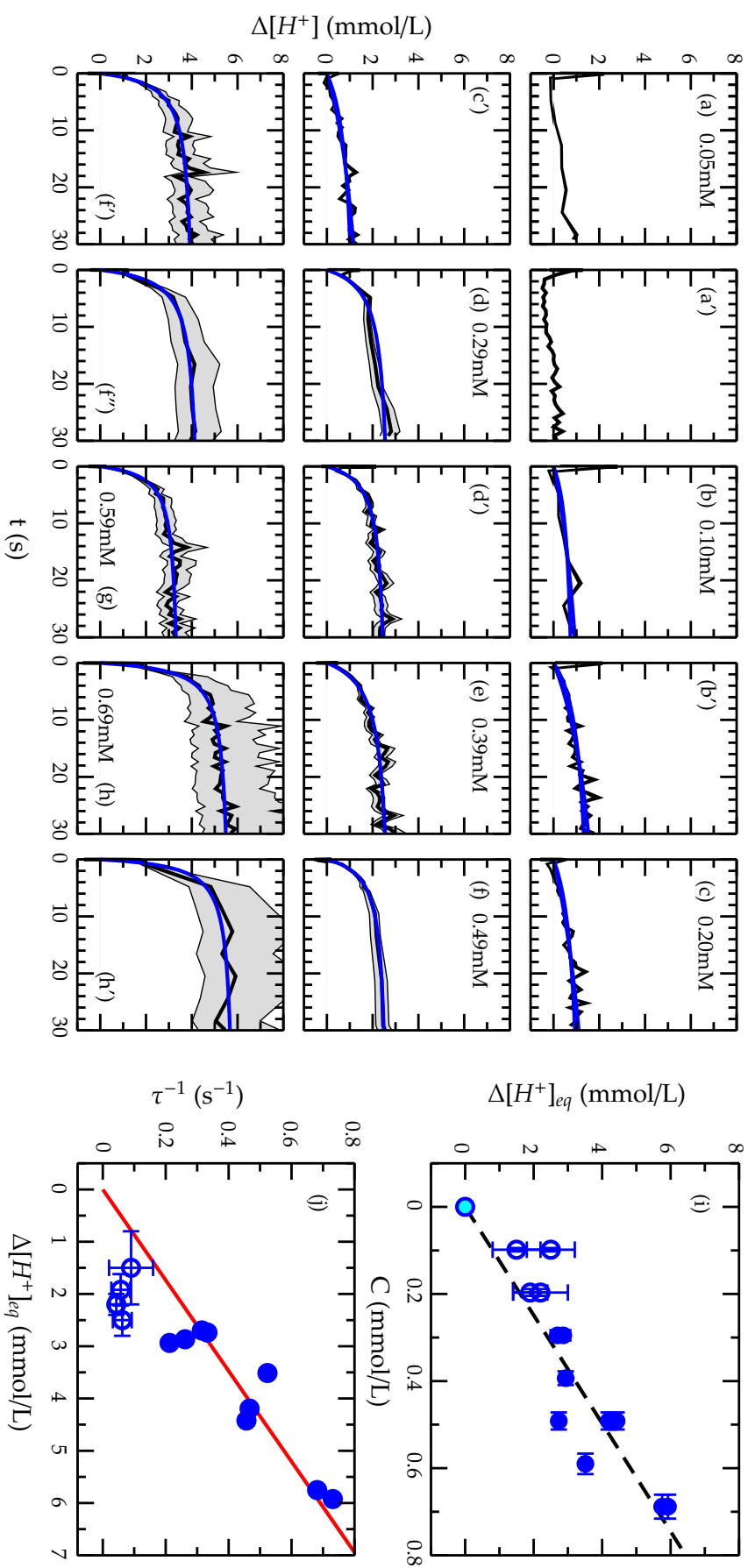
Figure 4.10: (a)–(h) Change of proton concentration inside the aqueous droplet in function of the time, using different concentrations of surfactant (carboxylic acid, Krytox) in the fluorous phase: (a) 0.05 mM, (b) 0.10 mM, (c) 0.20 mM, (d) 0.29 mM, (e) 0.39 mM, (f) 0.49 mM, (g) 0.59 mM and (h) 0.69 mM (as indicated) with ' and '' being repetitions of the same experimental condition. The black lines show the data calculated from the mean calibration curve with the grey shaded areas relating to the maximum and minimum calibration curves (Fig. 4.7). (i) Equilibrium change of proton concentrations ($\Delta[H^+]_{eq}$, fitted values) and (j) fitted τ^{-1} for all concentrations of surfactant. The fitting of the data of the small concentrations (b)–(c) is less confident as the pH change is very small. Thus, the fitting value of $\Delta[H^+]_{eq}$ was adjusted manually to obtain a range of fits. The light blue symbol is set to zero as no pH change takes place when no acidic surfactant is present.

4.2.6 Bulk equilibrium data

The measurement of τ_{pH} as a function of C_0 provides means to determine k_{ads}, provided that both quantities Γ_∞ and Γ_{eq} are known. These two quantities are equilibrium quantities and are measurable using standard characterisation techniques. I use a Wilhelmy plate tensiometer to measure interfacial tension as a function of surfactant concentration (Sec. 3.2.3). Using the standard Gibbs isotherm, these measurements provide the values of $\Gamma_{eq}(C)$, Γ_∞ and in addition the value of the CMC, above which the interfacial coverage stays constant (Sec. 4.1.2). Based on the developed second order adsorption model, I fit the experimental data (Fig. 4.4) with the form (Appendix A.2):

$$\Gamma_{eq} = \Gamma_\infty \frac{\kappa C^2}{1 + \kappa C^2} \tag{4.7}$$

$$\gamma_{eq} = \gamma_0 - \frac{1}{2} RT\Gamma_\infty \ln(1 + \kappa C^2) . \tag{4.8}$$

I here obtain $\Gamma_\infty = 8 \pm 1$ µmol/m^2, $\kappa = 7 \pm 1 \times 10^6$ (m^{6}mol^{-2}) and a critical micellar concentration of $C_{CMC} = 4 \pm 1$ µmol/L with the coverage at the CMC of $\Gamma_{eq}^{CMC} = 7.93$ µmol/m^2 (Appendix C.2.1). These values lead to the determination of $k_{ads} = 1.4 \pm 1 \times 10^3$ s^{-1}m^{6}mol^{-2} (Appendix C.2.2). The value of Γ_∞ corresponds to a value obtained for small headgroups, compatible with this molecule and other data from the literature for fluorinated surfactants[2,189]. It should be noted that I use my model for consistency. However a standard Langmuir isotherm provides the same value for Γ_∞ (see Eq. 2.22).

It also shows that – contrary to my microfluidic method – equilibrium measurements do not provide means to discriminate possible isotherm models. I obtain the adsorption constants from these experiments, provided that the equilibrium is independently determined through standard measurements. I use the same adsorption model to describe the equilibrium and the kinetics of pH change in the droplet, which enables the straightforward use of the equilibrium constants in the microfluidic experiments in a consistent manner.

4.2.7 Impact on coalescence

To finally validate this model, I show that the kinetics of proton transfer provides a value for k_{ads} compatible with the stabilisation of emulsions against coalescence. Indeed, it
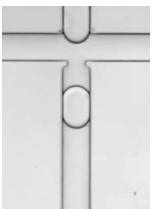
is known that the formation of the surfactant layer affects droplet stabilisation[110]. In the following, I describe the experiment conducted for the measurement of coalescence (Sec. 3.4) to determine the stabilisation of the interface[4] (t < 200 ms) and the experiments at equilibrium surfactant coverage (> 5 min). For these experiments, the same fluorous and aqueous phases as for the pH measurements were used[110]. The three parameters (1) surfactant concentration, (2) length of the channel L and (3) droplet speed U were independently varied to change the incubation time of the droplets ($t = L/U$). The droplet production is defined as stable if less than 1.5% of the droplets coalesce. The critical parameter that controls the separation between stable and unstable emulsions is the parameter LC^2[110]. Here, this parameter is proportional to the speed of the droplet U (Fig. 4.11).

These experiments on coalescence determine the transition between stable and unstable emulsions in flow. The transition towards a stable droplet production leads to a timescale for stabilisation of the interface of the form $\tau \sim 1/(kC^2)$ where $k \sim 909$ s^{-1}m^{6}mol^{-2} (Fig. 4.11). Hence, I can reuse the rate equation for the interfacial coverage Γ (Eq. 4.4) to predict the stabilisation time of the interface during microfluidic emulsification. The incubation of a droplet in a channel before coalescence favours the stabilisation at low surfactant concentration. This kinetic stabilisation results from the time dependent adsorption of the surfactant in flow. I use the rate equation of Γ (Eq. 4.4) to compare the stabilisation time of the interface during microfluidic emulsification to the adsorption process obtained from the pH measurements:

$$\frac{1}{2}\frac{\partial \Gamma}{\partial t} = k_{ads}C_0^2\left(\Gamma_\infty - \Gamma\right) - k_{des}\Gamma \; . \tag{4.4}$$

Through integration (Appendix D), I obtain:

$$\frac{\Gamma}{\Gamma_\infty} = \frac{k_{ads}C_0^2}{k_{ads}C_0^2 + k_{des}} \cdot \left(1 - e^{-2\left(k_{ads}C_0^2 + k_{des}\right)\cdot t}\right) \; . \tag{4.9}$$

The kinetics of coverage is an exponential relaxation to the equilibrium coverage with a timescale of

$$\tau = \frac{1}{2\,k_{ads}C^2 + 2\,k_{des}} \tag{4.10}$$

for the range of concentration used for the coalescence experiments. In the coalescence experiments, $t = L/U$ and thus,

$$\frac{L}{U}C_0^2 = -\frac{1}{2 \cdot k_{ads}} \cdot \frac{\Gamma_{eq}}{\Gamma_\infty} \ln\left(1 - \frac{\Gamma}{\Gamma_{eq}}\right) \; . \tag{4.11}$$

---

[4]Experiment conducted by Jean-Christophe Baret; Analysis performed by me and Jean-Christophe Baret.
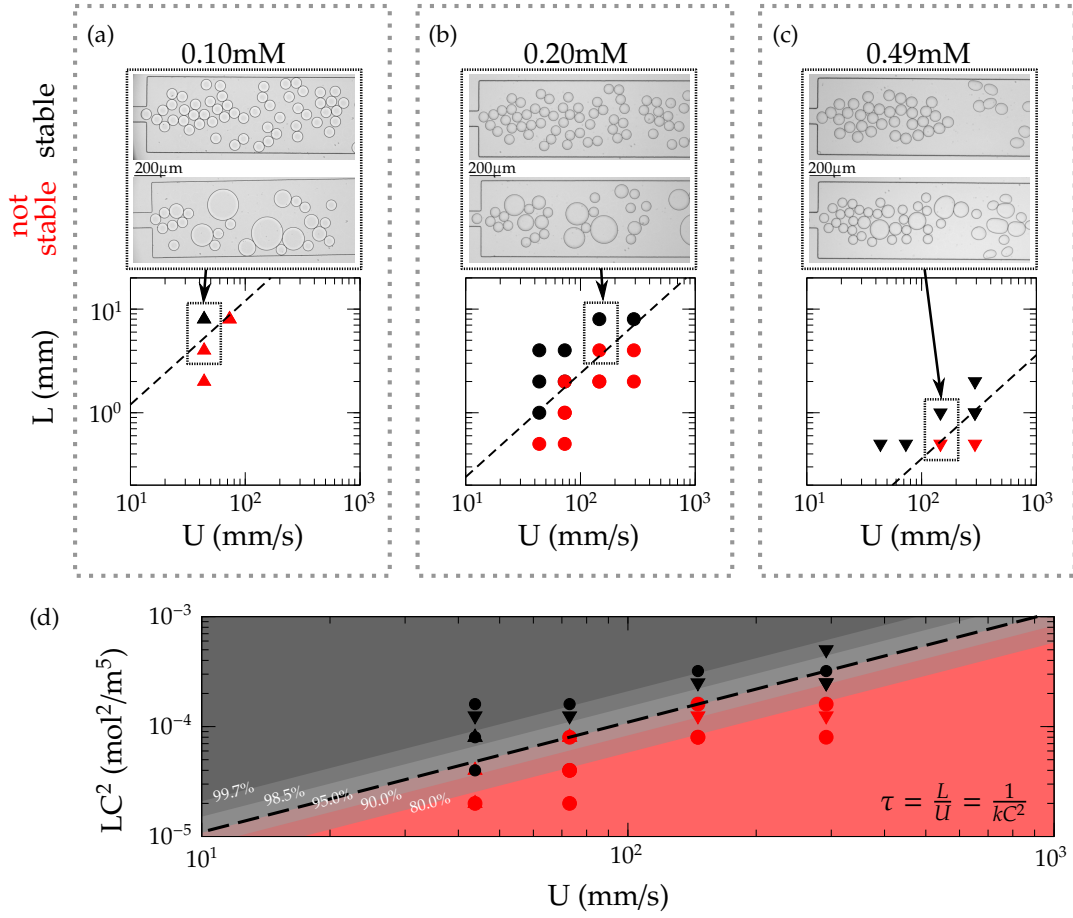
Figure 4.11: Coalescence experiment at different distances from the droplet production area on chip L and different speeds U with stable (black) and unstable (red) droplets against coalescence at different concentration, C, of surfactant ((a) 0.10 mM, (b) 0.20 mM, (c) 0.49 mM) with the corresponding images. The transition from stable to unstable droplets takes place at different timescales τ depending on the concentration of surfactant (dashed lines: (a) $\tau = L/U = 0.12$ s, (b) $\tau = 0.024$ s, (c) $\tau = 0.0036$ s). (d) The data from (a), (b), (c) scale linear with $LC^2 = 0.0011$ s mol^2/m$^6 \cdot U$ (dashed line). The different symbols refer to the different concentrations (related to the symbols in (a), (b), (c)). The coverage Γ/Γ_{eq}^{CMC} of the interface for different values between 80.0% and 99.7% is represented by the lines of iso-Γ (Eq. 4.13).

Above the CMC, the coverage is constant:

$$\frac{\Gamma_{eq}}{\Gamma_\infty} \sim 1 \, . \tag{4.12}$$

Therefore, I obtain:

$$\frac{L}{U}C_0^2 = -\frac{1}{2 \cdot k_{ads}} \ln\left(1 - \frac{\Gamma}{\Gamma_{eq}^{CMC}}\right) \tag{4.13}$$

with the equilibrium coverage for the CMC: Γ_{eq}^{CMC}. I obtain the value LC_0^2/U (Eq. 4.13) from the coalescence experiments. It is the slope of the transition from unstable to stable droplets (Fig. 4.11(d)) which leads to the determination of the interfacial coverage Γ. Fig. 4.11(d) shows the lines of iso-Γ superimposed to the coalescence data: The stabilisation of the emulsion occurs when the coverage of the interface is close to its
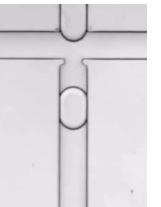
equilibrium coverage (in the range 90-95%) which is close to the maximum coverage for concentrations above the CMC (as for these experiments).

To confirm these results, I performed stabilisation measurements bringing two interfaces, which are at equilibrium coverage, into contact (Fig. 4.12(a)). The aim is to define the equilibrium coverage needed for the stabilisation of an interface. From the video, the stacks of lines in the x and the y direction as a function of time (Fig. 4.12(b)-(c)) clearly show the first contact and the coalescence events. Comparing the stacks of the line in the y direction for different concentrations (Fig. 4.12(c)-(k)), the contact time before coalescence occurs increases with increasing surfactant concentration. For the smallest surfactant concentration of 0.01 mM, the interfaces are only stable for up to 1.5 s (Fig. 4.12(c)-(e) with repetitions) whereas the interfaces start to stabilise for higher concentrations (Fig. 4.12(f)-(k)). An interface in equilibrium with a surfactant solution of 0.10 mM is stable for more than 7 min (not shown). These concentrations are above the CMC (C_{CMC} = 4 μmol/L, $\Gamma_{eq}^{CMC}/\Gamma_{\infty}$ = 99.1%, see Sec. 4.2.6). This confirms the result that an interface is only stable when the interface is nearly fully covered.

In conclusion, the values extracted from the pH measurements on chip provide a quantitative description of the kinetics of stabilisation and of transfer across the interface in a unified picture. I show that the stabilisation of the interface needs a minimum concentration close to the CMC leading to a nearly complete coverage of the interface.
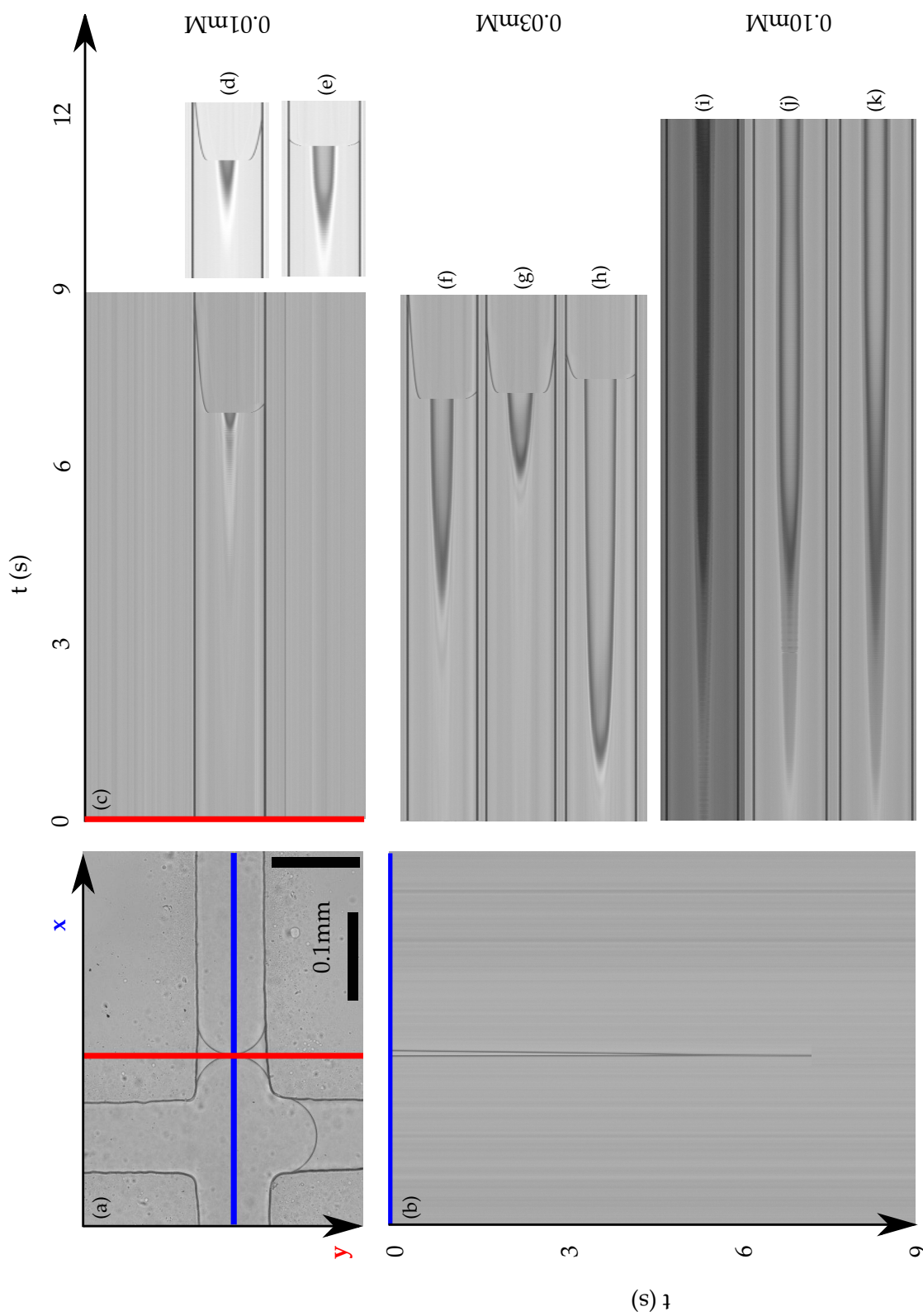
Figure 4.12: Coalescence of two interfaces at equilibrium with the surrounding surfactant solution. A snapshot of the video (a) of a solution with 0.01 mM. The x and y lines for the stacks in blue and red, respectively (0.01 mM): (b) x, time; (c) y, time; (d),(e) y, time, repetitions; (f)-(h) y, time for 0.03 mM; (i)-(k) y, time for 0.10 mM).
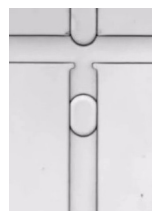
Summary of Section 4.2 – Adsorption kinetics

I used fluorescence measurements to determine the pH change due to the adsorption of an acidic surfactant to the interface. The typical timescale for the pH change is in the order of seconds for surfactant concentrations between 0.10 mM and 0.69 mM. For the highest concentrations, the pH decreases upon adsorption from an initial pH of ~7.3 to a pH of ~6.2.

Additionally, I analysed coalescence experiments to obtain a dependence of the stability of an interface with its age and the surfactant concentration.

Using these experiments, I describe the kinetics of the transfer of protons across the interface and the stabilisation of an interface due to surfactant adsorption using one single model. The speed of the reaction is second order in the concentration of surfactant. Standard interfacial methods do not distinguish between this model and a typical Langmuir adsorption model where the speed is first order with the concentration. Combining the adsorption experiments with the coalescence experiments, I show that an interface is only stable if it is nearly fully covered by surfactants (minimum 90-95%).

## 4.3 Consequence to improve surfactant synthesis

I have shown, that the presence of a carboxylic acid as surfactant has a great influence on the pH of the droplets. The PFPE-PEG-PFPE surfactant commonly used in droplet-based microfluidics, is synthesised from the carboxylic acid KrytoxFSH. I expect a full transfer of H^+ from traces of Krytox inside the PFPE-PEG-PFPE surfactant towards the droplet, which makes the purity of the synthesised surfactant an essential factor. Therefore, I improved the synthesis of the PFPE-PEG-PFPE surfactant (Sec. 3.5). In this chapter, I analyse the quality of this synthesised product and quantify its impurities using IR spectroscopy and partitioning experiments. I also used ^{19}F-NMR spectroscopy, but due to very low intensities of the relevant signals no quantitative statement of the purity can be obtained from such spectra (Appendix E).
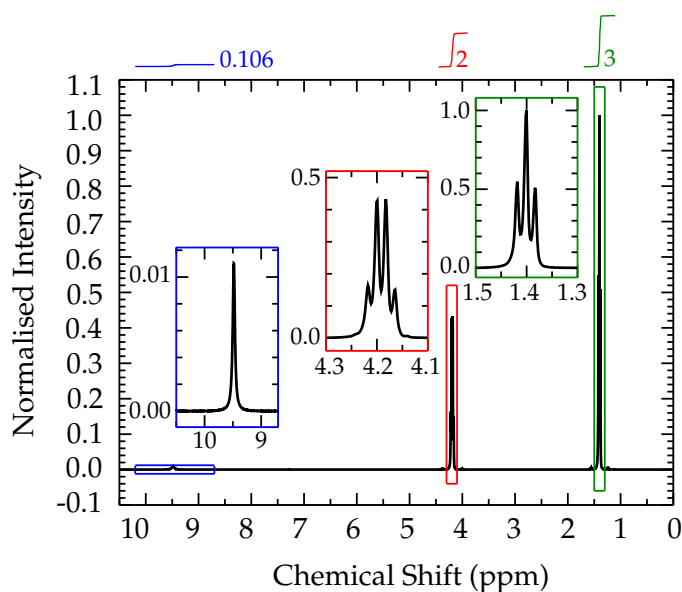
4.3.1 Determination of the molecular weight

For the synthesis, it is a prerequisite to know the molecular weight of the KrytoxFSH or the amount of carboxylic acid groups per weight. In the literature[158,160] and similar to the KrytoxFSL (Sec. 3.2.1), it is stated that the molecular weight varies tremendously from the molecular weight given by the supplier.

I use ^{1}H-NMR spectroscopy to determine the relative amount of carboxylic acid groups inside a 1:1 mixture with Novec7500 (Fig. 4.13). I proceed the same way as for the determination of the molecular mass of the KrytoxFSL (Sec. 3.2.1, 4.1.1). I could not use ESI-MS because the maximum molecular weight for this spectrometer is 4000 g/mol.

The NMR spectrum shows a singlet for the proton of the carboxylic acid end group with a chemical shift, δ, of 9.50 p.p.m.[155] (Fig. 4.13). The triplet and the quartet of the ethoxy group are obtained with a chemical shift centred at 1.40 and 4.19, respectively. The integrals of the singlet, triplet and quartet are measured to be 0.106 ± 0.010, 3 and 2 ± 0.03, respectively. Using the molecular mass of the solvent, I obtain a weight ratio of the compounds, and a molecular weight of 3938 ± 257 g/mol with 22 of the repeating units, n.
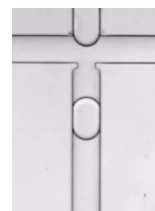
Figure 4.13: ^{1}H-NMR of a solution of 1:1 (w/w) of KrytoxFSH and Novec7500. The integrals of the triplet and the quartet from the ethoxy group are put in relation to the integral of the singlet from the carboxylic endgroup to obtain the molecular weight of KrytoxFSH.

4.3.2 Analysis using infrared spectroscopy

To determine the purity of the surfactant, I use IR spectroscopy (Sec. 3.5.2). The analytical protocol is based on IR bands[190,191] according to Doan *et al.*[155], Dejournette *et al.*[161], Loeker *et al.*[192] and Matochko *et al.*[162].

I normalise the IR spectra (P_{0-5}) to the band of the alkane group of the Jeffamine between $3000\,\mathrm{cm}^{-1}$ and $2800\,\mathrm{cm}^{-1}$ (R_2). I treat the other spectra (R_1, C_{1-2}) normalising their product peaks to the height of the peak at $1700\ \mathrm{cm}^{-1}$ of R_1 (Fig. 4.14). From the reaction scheme (Fig. 3.12), I expect two side products. As described previously, two possible impurities are the carboxylic acid and the carboxylate salt, which arises from a triethylamine salt or from a Jeffamine salt[161]. The product should display both an amide bond and the characteristic Jeffamine bonds. Small variations exist between the different batches of Jeffamine. The product P_0 was synthesised by E. Mayot and is used as a reference as the analysis of this surfactant has shown very good performances for the use in droplet-based microfluidics[61]. I conduct the analysis and compare the presence of the alkane CH stretch bands and the different product bands (CO stretch vibration between ~1775 - $1650\ \mathrm{cm}^{-1}$).
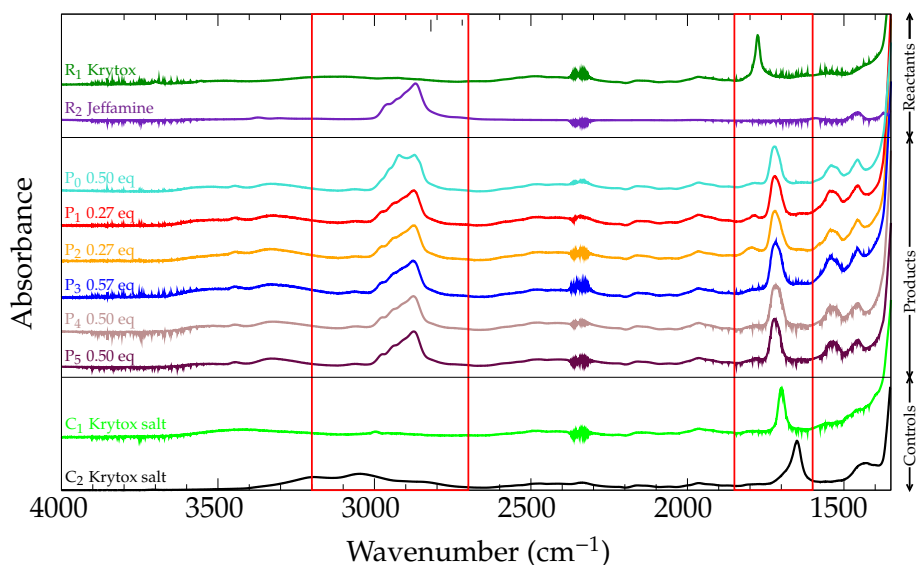
(a)
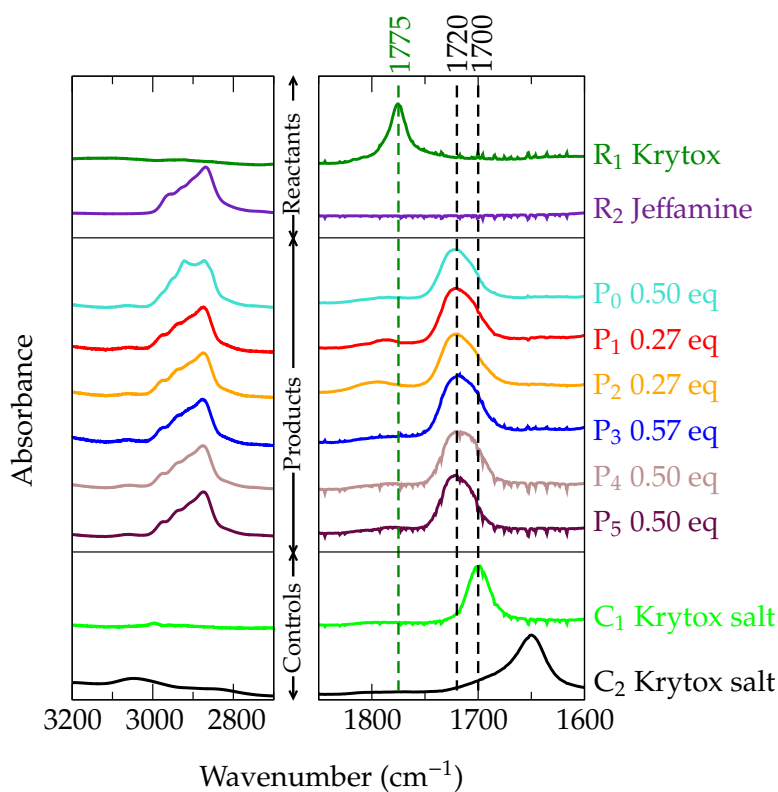
(b)

Figure 4.14: Analysis of the reaction products from the surfactant synthesis. (a)-(b) Infrared spectra of the reagents R_{1-2}, products P_{0-5} (with equivalents to KrytoxFSH used) and control C_{1-2} synthesis (C_1: Jeffamine-Krytox salt; C_2: Krytox-ammonium salt, synthesised by E. Mayot[193]): the covalent binding of the Jeffamine and the PFPE is revealed by an IR band at 1720 cm^{-1}. The Jeffamine-PFPE salt corresponds to a band at 1700 cm^{-1} (see also Dejournette *et al.*[161]). The carboxylic acid band of the reactant is at 1775 cm^{-1} and is barely visible indicating traces of reactants in the final product. P_0 is the surfactant synthesised by E. Mayot with a similar synthesis. (b) Zoom of the alkane CH stretch bands (~3000 cm^{-1}) for the normalisation and the carbonyl stretch bands (~1775 - 1650 cm^{-1}) for the qualitative analysis.
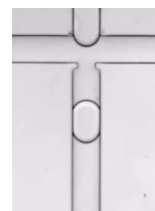
The Krytox (R_0) does not show strong bands in the range of 3000 cm^{-1} to 2800 cm^{-1}. The OH stretch vibration in the range of 3300 - 2800 cm^{-1} and the NH stretch vibration of the amide and amine (R_1) between 3500 - 3000 cm^{-1} are very broad. Thus, they cannot be used for any quantitative analysis and they are easily distinguishable from the alkane bands. The carboxylate groups have peaks in the range of 1800 - 1600 cm^{-1} where the Jeffamine (R_1) does not show any band.

The Krytox (R_0) shows a clear band at 1775 cm^{-1}, as previously reported by Doan *et al.*[155] and Loeker *et al.*[192] (Fig. 4.15(a)-(b)). For all products (P_0 to P_5), I measure a band related to the amine bands which is systematically shifted (compared to the Krytox band) indicating that the reaction occurred (Fig. 4.14).

For the control reaction (reaction opened to air, C_1), no sharp band is present in the range of 3000 - 2800 cm^{-1}: the Jeffamine is not covalently bound to the Krytox, the reaction did not occur. The product is however different than the reagent (product band at 1700 cm^{-1}). In the literature, a shift of the band towards lower wavenumbers is attributed to a carboxylate ammonium salt (Fig. 4.15(d), blue trace)[161]. The 1700 cm^{-1} band is also present in Matochko *et al.* (Fig. 4.15(c))[162]. As a note, it is expected that the CO band of the salt shifts with the counterion: I observe for example a band at 1650 cm^{-1} for the ammonium salt of Krytox (control C_2, synthesised by E. Mayot[193]), as reported by Loeker *et al.* previously (Fig. 4.15(b))[192], while sodium salt leads to bands (eventually doublets) at 1665-1696 cm^{-1} (Fig. 4.15(a))[155] and the non-covalent Jeffamine-Krytox shows bands at 1702 (turquoise curve in Fig. 4.15(d))[161]. As the alkane band of the Jeffamine is not present (control C_1), I conclude, that the band at 1700 cm^{-1} corresponds to a salt of Krytox (likely with a triethylammonium counterion used in the synthesis).

Considering now the IR spectra of the products P_{0-5}, I systematically obtain a clear band at 1720 cm^{-1}. Additionally, for the product spectra (P_{0-5}), a new band appears at 1540 cm^{-1} being due to the NH bending vibration of amides typically appearing in the range of 1650-1450 cm^{-1} indicating if the reaction occurred. In Dejournette *et al.* (Fig. 4.15(d))[161], the band at 1720 cm^{-1} is recovered for the covalently bound Krytox-Jeffamine (black trace) but with a strong additional band at 1770 cm^{-1} where I found the reagent Krytox band. This means, the product of the reaction in Dejournette *et al.*[161] is highly contaminated with Krytox. The 1720 cm^{-1} band is also present in Matochko *et al.* (Fig. 4.15(c))[162], but
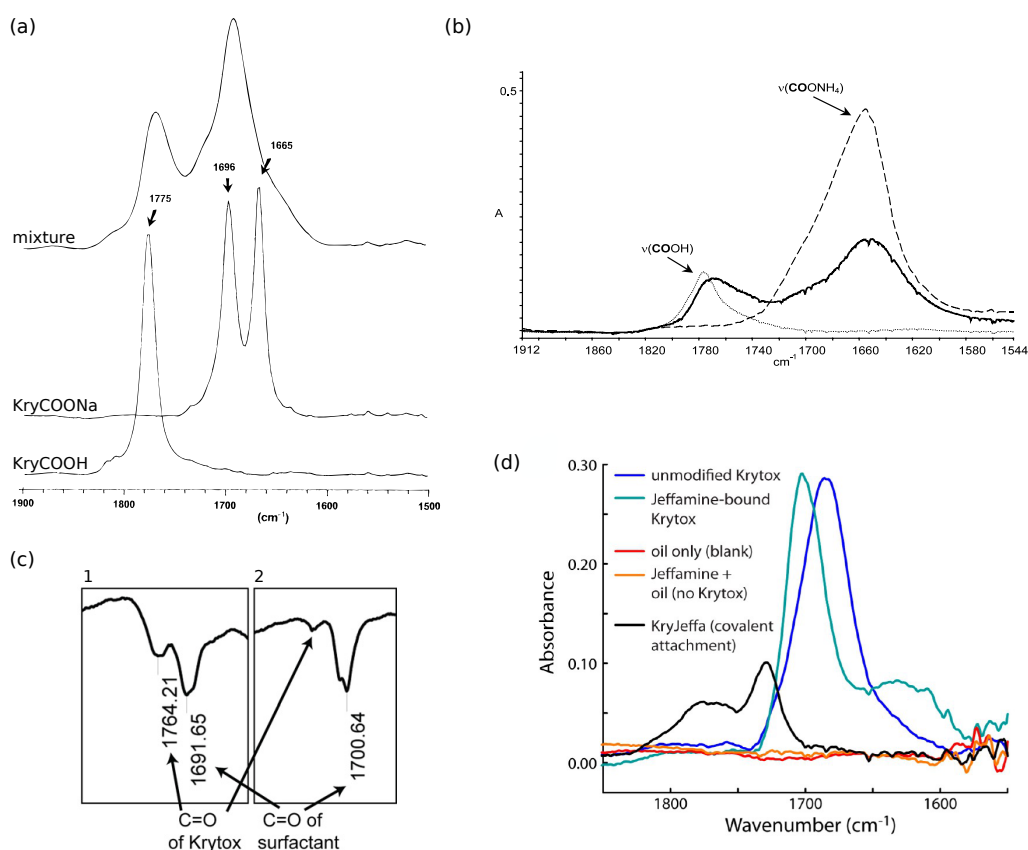
Figure 4.15: Infrared spectra from the literature. (a) The carbonyl region for the Krytox carboxylic acid (KryCOOH), the Krytox sodium salt (KryCOONa) and a 1:1 mixture of the salt and the acid (Reprinted with permission from V. Doan, R. Köppe, P. H. Kasai, *Journal of American Chemical Society* **1997**, *119*, 9810-9815. Copyright (1997) American Chemical Society. [155]). (b) Krytox carboxylic acid (dotted line), Krytox ammonium salt (dashed line) and a mixture of the two (full line) (Reprinted from Colloids and Surfaces A: Physicochemical and Engineering Aspects, 214 (1-3), F. Loeker, P. C. Marr, S. M. Howdle, FTIR analysis of water in supercritical carbon dioxide microemulsions using monofunctional perfluoropolyether surfactants, 143-150, Copyright (2003), with permission from Elsevier. [192]). (c) (1) Incomplete and (2) complete reaction of the Krytox carboxylic acid towards the surfactant PFPE-PEG-PFPE (Reprinted from Methods, 58, W. L. Matochko, S. Ng, M. R. Jafari, J. Romaniuk, S. K. Y. Tang, R. Derda, Uniform amplification of phage display libraries in monodisperse emulsions, 18-27, Copyright (2012), with permission from Elsevier. [162]). (d) Ammonium carboxylate of Krytox ('unmodified'), ionic binding between carboxylic acid and Jeffamine ('Jeffamine-bound-Krytox'), oil only, Jeffamine in oil, PFPE-PEG-PFPE surfactants ('KryJeffa covalent') (Reprinted with permission from C. J. Dejournette, J. Kim, H. Medlen, X. Li, L. J.Vincent, C. J. Easley, *Analytical Chemistry* 2013, 85, 10556-10564. Copyright (2013) American Chemical Society. [161]).
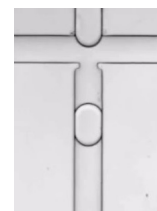
is a shoulder of the peak at 1700 cm^{-1}: the product of the reaction in Matochko *et al.*[162] is therefore likely to be contaminated with the Krytox salt.

In contrast, all of my products show minor bands at 1775 cm^{-1} and – possibly – a very weak shoulder around 1700 cm^{-1}. Hence, the purity of my surfactant is much higher than that of previous publications. I also recover that when the reaction is performed with an excess of Krytox (P_1, P_2), the side product is mainly the Krytox (bump at 1780-1790 cm^{-1}). In contrast, when the reaction is performed with larger amounts of Jeffamine (2:1 ($P_{0,4,5}$) or excess of Jeffamine (P_3)), the side product is mainly the Jeffamine-Krytox salt.
In my synthesis, the amount of Krytox left over (in the form of acid or salt) is small, in the order of a couple of percent from an estimate based on the spectra and better than previous claims[143,162].

4.3.3 Analysis using partitioning

In order to estimate this amount quantitatively, I use the partitioning experiment with Rhodamine 6G[5] (Fig. 4.16, Sec. 3.5.3). It was shown[61] that Krytox binds to Rhodamine
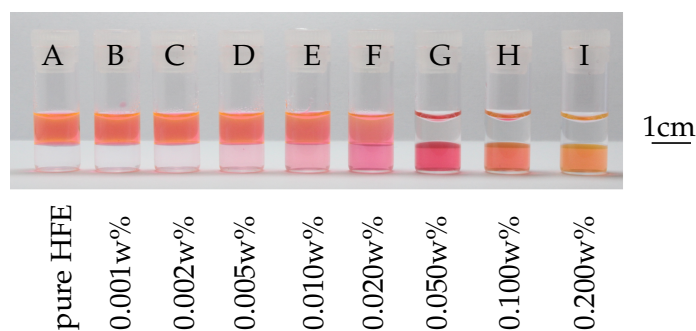
Figure 4.16: Partitioning experiments for the calibration of the leakage of Rhodamine 6G towards the fluorous phase. At time zero, the top phase consists of 100 μM of Rhodamine 6G in millipore water and the bottom phase contains the indicated concentrations of KrytoxFSH.

6G as a 1:1 complex leading to extraction towards the oil. In this study, I use a calibration curve to obtain the amount of Krytox inside the oil phase (Fig. 4.16, 4.17). The partitioning measured from the fluorous phase, is more sensitive to small changes of absorbance close to zero and, thus, more sensitive to small impurities. However, the use of the aqueous calibration curve gives similar results (data not shown). I obtain the calibration curve as

---

[5]I perform these experiments according to the partitioning experiments by Philipp Gruner, Max Planck Institute for Dynamics & Self-Organization
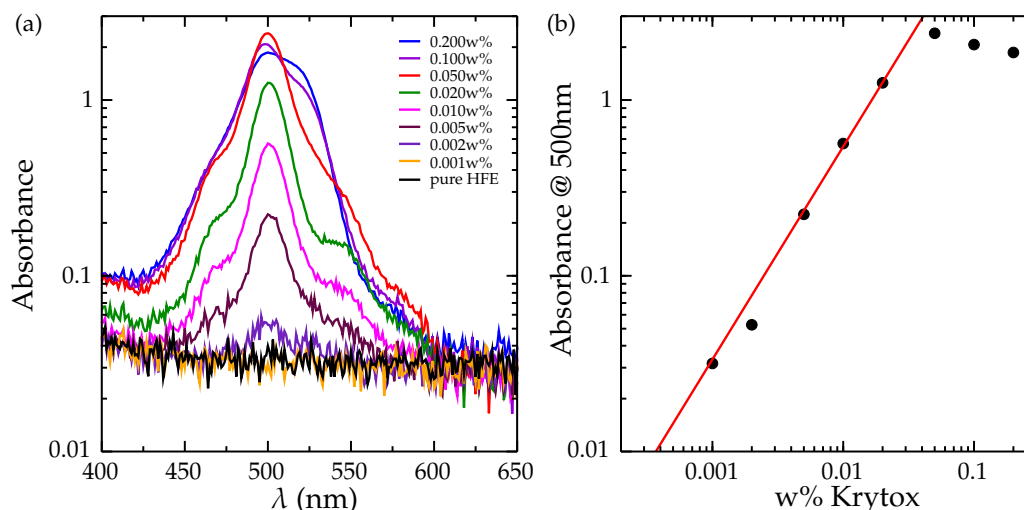
Figure 4.17: (a) The absorbance spectra of the fluorous phase (Fig. 4.16) including the value of absorbance of the maxima at 500 nm (shown in (b)). The red line corresponds to the calibration curve obtained upon fitting the data with $y = 144x^{1.2115}$.

previously done by Gruner *et al.* [61,185] (Sec. 3.5.3).

For the samples P_{0-5}, I use a 1 w% and 0.5 w% PEG-PFPE surfactant solution and measure the fluorescence in the oil phase[6] (Fig. 4.18). I compare the amount of extracted Rhodamine 6G to the amount upon extraction with a known amount of carboxylic acid (Fig. 4.17). The error bars in the amount of impurity inside the sample show the measurements of the two concentrations. From this, I conclude that all surfactant solutions show a partitioning to the oil corresponding to less than 1 w% contamination with Krytox. The purity of my end product is therefore of the order of 99 w%.

4.3.4 Further analysis and purification

I obtain ^{19}F-NMR spectra of the fluorinated solvents (C_6F_6, Novec7100, FC3283), the reactant (KrytoxFSH), the control (C_1) and the product (P_5). I present and discuss the spectra and the signals in the appendix E. Upon comparing these spectra with literature values, I show that they do not give any further information in terms of purity of the synthesised surfactants. This is mainly due to the low intensities of the relevant signals.

As seen by the IR and partitioning experiments (Sec. 4.3.2, 4.3.3), further purification steps of the product from the surfactant synthesis would be of great help to make sure that the

---

[6]Sample P_0 was measured by Philipp Gruner.
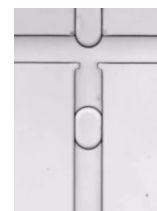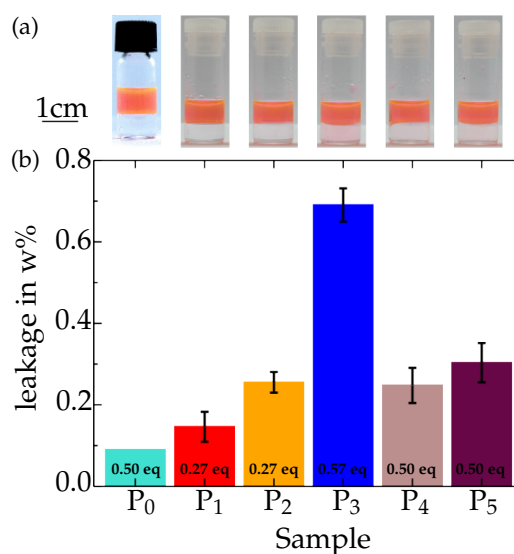
Figure 4.18: Partitioning experiments for the synthesised surfactants with different samples: $P_{0,4,5}$ 2:1 Krytox:Jeffamine, $P_{1,2}$ excess of Krytox, P_3 excess of Jeffamine (equivalents to KrytoxFSH indicated in (b)). (a) Photos of the 0.5 w% partitioning experiments. (b) The leakage is the amount of dye extracted using the molecular weight of KrytoxFSH. The error bars show the values for the 0.5 w% and 1 w% experiments.

product is free of Krytox and the salt of the Krytox. These two molecules interact well with organic molecules and lead to extraction (Sec. 4.3.3). Thus, I grafted a silane with an amine headgroup onto silica beads (Sec. 3.5.1). ^{1}H-NMR analysis[7] has shown, though, that all surfactant is removed and not just the Krytox.

Summary of Section 4.3 – Surfactant synthesis

I improved the synthesis of the PFPE-PEG-PFPE surfactant. I qualitatively analysed the surfactant using infrared spectroscopy for the detection of residual carboxylic acid (Krytox) and its salt inside the synthesised product. I quantified the left over carboxylic acid using partitioning experiments and have shown that the surfactant synthesis can be optimised to less than 1w% of residual carboxylic acid.

---

[7]Performed by Philipp Gruner, Max Planck Institute for Dynamics & Self-Organization

Summary of Chapter 4 – Surfactants and Adsorption Kinetics

I characterised the surfactant using bulk interfacial experiments such as the Wilhelmy and the pendant drop method. I have shown the importance of buffer conditions for the effective adsorption of a charged surfactant to the interface and the inconvenience of long equilibration times using these methods.

Thus, I used miniaturised pH experiments to quantify the adsorption kinetics of an acid surfactant to the interface. I have shown that a full transfer of protons takes place from the acidic surfactant inside the oil phase towards the aqueous phase. At the same time, the measured kinetics of pH change can be used to explain the stabilisation of the interface as well. I used this information to explain the implications of left over carboxylic acid from the synthesis of the PFPE-PEG-PFPE surfactant. And finally, I used these principle to improved the synthesis of the PFPE-PEG-PFPE surfactant to obtain less than 1w% left over carboxylic acid.

I show that the transfer of ions and small molecules from one phase to the other is controlled by surfactants. These results could have implications on designing new ways for liquid / liquid extraction in chemical engineering or on developing systems for the control of communication through chemical exchange in an assembly of droplets.
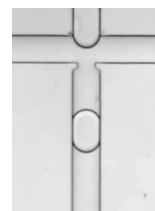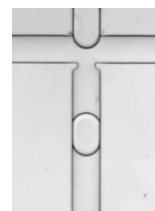
Chapter 5

Follow-Up Experiments

In this chapter, I discuss ongoing experiments on the behaviour of surfactants at interfaces as well as surfactant applications in droplet-based microfluidics.

5.1 Alternative measurement of adsorption

So far, I have measured the adsorption kinetics using pH measurements and coalescence experiments at the micronscale. This approach is limited to an acidic surfactant. An alternative approach to obtain information on adsorption kinetics can be to measure the change of the velocity of droplets inside channels upon surfactant adsorption. The change in speed is of interest, as surfactant adsorption to the interface of flowing droplets and change the rheological properties (Sec. 2.5). Thus, the speed of the droplets inside a microfluidic channel is prone to changes with the age of the droplet. This can lead to a Marangoni effect slowing the droplets down. In the following sections, I describe the methods and the preliminary results obtained.

5.1.1 Materials and methods

In order to investigate the change of the velocity of droplets with surfactant laden interfaces on chip over a large time frame, I used a long microfluidic channel made from PMMA. The PMMA device had the same dimensions as the device for the pH mea-

surements (Sec. 3.1.2) apart from the width of the channel. In this case, the microfluidic channels had a diameter of 150 µm. I used a fluorous phase which contained 0.10 mM KrytoxFSL in Novec7500 and an aqueous phase with PBS (and SNARF-1, pH=7.10, Sec. 3.3). I set the flow rates to 7.5 and 1.5 µL/min for the fluorous and the aqueous phase, respectively. To record high speed videos (Sec. 3.4) of 8 different areas on chip, I used a microscope (IX71, Olympus, objective 2x) and recorded 2000 frames with a sample rate of 1500 fps, an exposure time of 6 µs and a resolution of 1152 x 800 pixels.

5.1.2 Results and discussion

For these experiments, microfluidic channels made from PMMA have advantages over PDMS devices because PMMA channels withstands higher pressures and do not deform significantly (Sec. 3.1). Due to the stability of PMMA against higher flow rates, a droplet production without the use of surfactants becomes feasible. These properties make it possible to obtain information on the evolution of the speed of the droplets over time and to relate a change of velocity to the concentration of surfactant inside the continuous phase. I determine the speed of the droplets at different positions on chip (Fig. 5.1) using a surfactant solution with a concentration (0.10 mM) above the CMC. This means that full coverage occurs in the order of a couple of seconds (Sec. 4.1.2, Fig. 4.3(b)). For each position, I measured the velocity of three droplets and compared the differences of the velocity at the two sides of the chip (A-C in comparison to D-F in Fig. 5.1) as well as the differences of the speed at the production and at the end of the microfluidic channel (A, D in comparison to C, F in Fig. 5.1). The speed of the droplet changes more pronounced from one side to the other side of the channel than from the production to the end of the channel. This means, a contribution from the Marangoni effect cannot be extracted. Thus, I use the average speed due to the flow rates to determine the age of the droplets in the pH experiments (Sec. 4.2.1).
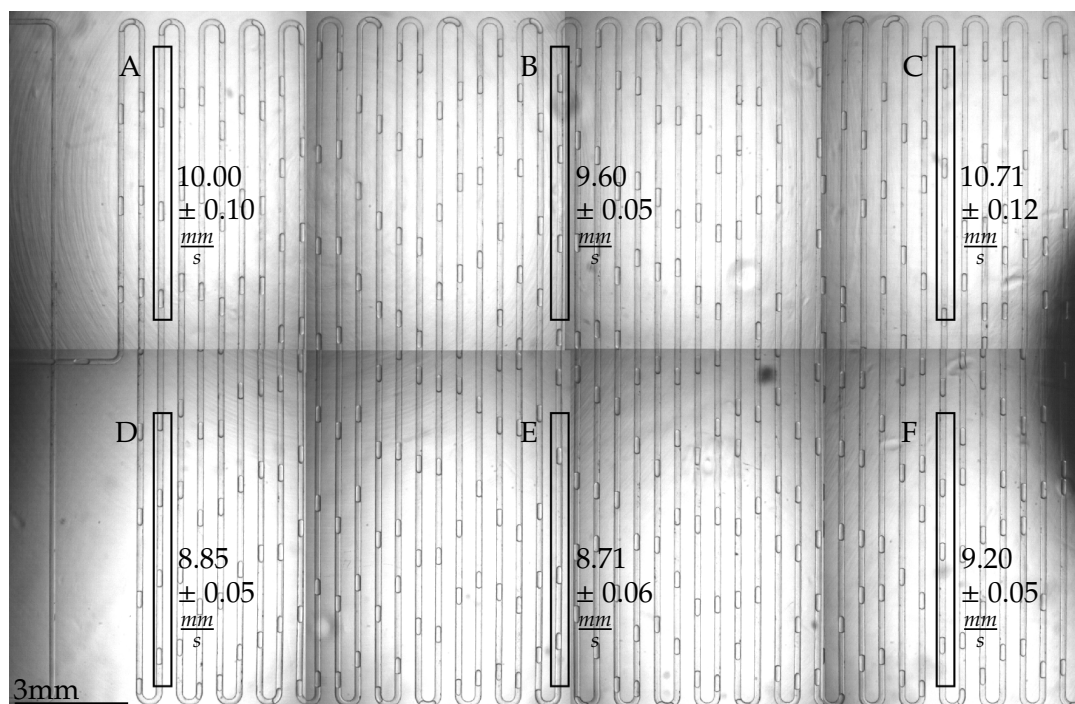
Figure 5.1: Video frames capturing the microfluidic PMMA device to obtain the speed of the droplets at different droplet ages. The speed is given for the positions A-F and depends on the side of the device rather than the age of the droplet.

Summary of Section 5.1 – Alternative adsorption experiments

Due to the variation of the height of the channels, no information on the Marangoni effect was obtained so far. This does not pose a problem for the pH measurements as the average velocity can be used. The improvement of the uniformity of the height of the microfluidic channels could make the developed measurement successful.
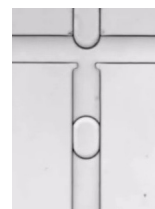
5.2 The role of pH in the self-propulsion of droplets

Adsorption kinetics of surfactants play a crucial role in self-propulsion as well[7,90]. Such a movement can be due to the Marangoni effect, which results from an inhomogeneous surfactant distribution at the interface. The maintenance of this inhomogeneity is directly related to the rate of adsorption and desorption of surfactants (Sec. 2.5). Thus, the study of adsorption kinetics can provide further insight into the effect of self-propulsion. Additionally to the perfluorinated acid (Krytox) used in the adsorption experiments, a wide variety of organic carboxylic acids exist, which are soluble in organic oils. I can apply the knowledge, I gained on the dynamics of pH change to other interfacial effects. Using oleic acid and squalane, a simple water-in-oil emulsion system showing biomimetic behaviours was developed.[1] Interfacial properties control the different behaviours of movement of the droplet through the oil phase. My contribution to this project was the characterisation of the surfactant, oleic acid, in the continuous phase, squalane (Sec. 3.2).

5.2.1 Materials and methods

In short, this system, studied in a millifluidic setup was composed of squalane and oleic acid at different concentrations as the continuous phase. This phase was placed into a plastic or glass petri dish and 2 µL of the aqueous phase were slowly injected. The latter consisted of a variety of concentrations of TrisHCl and $CaCl_2$. The pH of the aqueous droplet decreases with decreasing concentration of the buffer TrisHCl due to the fact that the buffer is diluted. A phase diagram of the droplet's behaviour in relation to the components of the aqueous phase and the surfactant was obtained.

I characterised the surfactant oleic acid in squalane using interfacial tension measurements (Sec. 3.2.3).

5.2.2 Results and discussion

Another interfacial phenomenon is the movement of a droplet due to surfactant adsorption. Depending on the concentration of solutes in the aqueous phase and of surfactant

---

[1]The experiments were conducted by Florine Maes and Deniz Pekin.

(a)

(b)

1cm

1cm
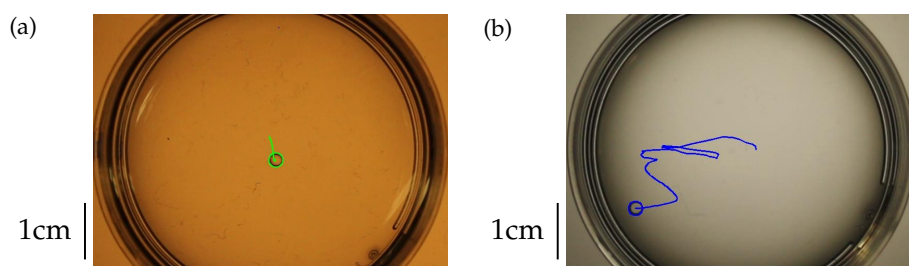
Figure 5.2: Example of aqueous droplets in a surfactant solution of 100 mM oleic acid in squalane showing (a) no movement and (b) self-propulsion. (a) A pure water droplet without displacement during 179 s. The only movement seen (green trace) is due to the initial deposition of the droplet into the solution. (b) An aqueous droplet containing 10 mM TrisHCl and 10 mM $CaCl_2$ shows self-propulsion (blue trace corresponds to 58 s). (a)-(b) These experiments were performed by F. Maes and D. Pekin and the image analysis by J. Vrignon.

in the continuous phase, the droplets show different behaviours of movement, such as self-propulsion by swimming or (ameoba-like) deformation, the formation of a shell, division or microemulsification. An example of a stationary and a self-propelled droplet is shown in Fig. 5.2. For the understanding of the behaviour, I characterise the interface of the surfactant, oleic acid, in squalane (CMC, interfacial tension $\gamma(t)$) in contact with millipore water (Fig. 5.3). I perform the measurement using the platinum Wilhelmy plate. Two issues have to be solved: First, the wetting properties of the aqueous phase are not homogeneous on the platinum plate. Thus, I use a paper Wilhelmy plate to attempt this problem. Second, the interfacial tension of the pure squalane with water decreases over time. The filtration with Celite® or Alumina (Fig 5.3) gives slightly better results, but a decrease of the interfacial tension is still visible over a time of more than 10^5 s. The interfacial tension between pure squalane and millipore water is roughly between 41 and 48 mN/m (grey shaded area in Fig. 5.3). These data suggest a CMC around 40 mM but further measurements are necessary using very pure squalane to confirm this result.

The direct measurement of squalane without further purification shows a changing interfacial tension over time (Fig. 5.3). This means that surface active molecules are present as impurities inside the squalane. These impurities have to be removed to obtain the interfacial tension of pure squalane and information on the effect of oleic acid on the interfacial tension.

The impurities were not removed when filtering the squalane over Celite® (Fig. 5.3). While it was shown previously that Alumina proved to be successful to remove the impurities and obtain a stable interfacial tension between squalane and water (52.5 ± 0.5 mN/m
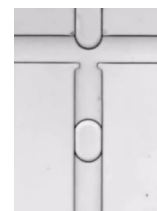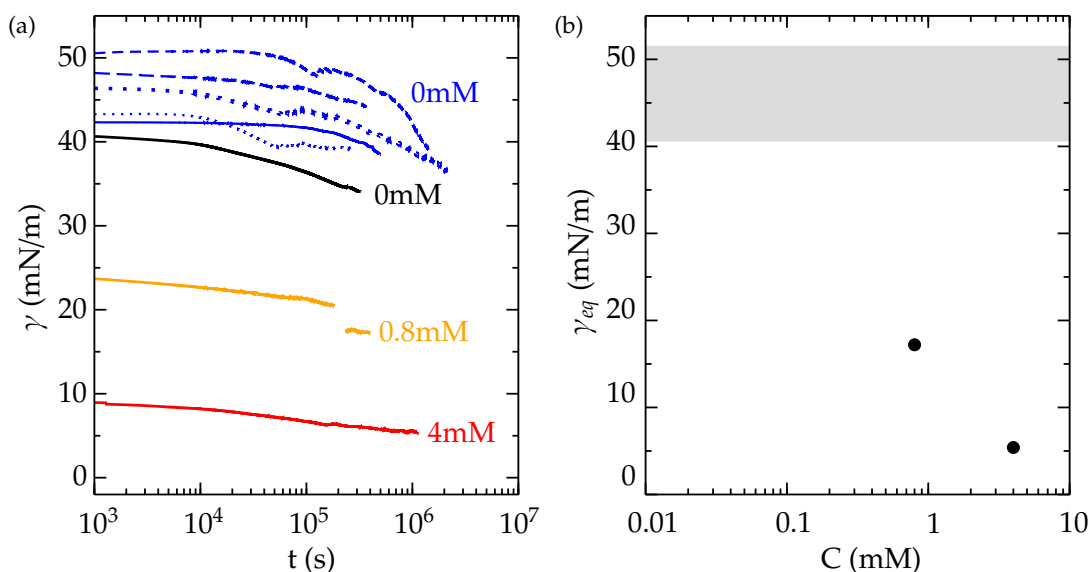
Figure 5.3: (a) The interfacial tension γ of oleic acid in squalane with millipore water. Continuous line: non-filtered, dotted lines: filtered with Celite®, dashed lines: filtered with Alumina, blue lines: paper Wilhelmy plate, other colours: platinum Whilhelmy plate. (b) Equilibrium interfacial tension (last values in time) with concentration of oleic acid. These measurements include an error due to non-filtered squalane also visible in the grey shaded area (interfacial tension for pure squalane and water falls roughly within the range of the grey area).

over 1000 s[80]), the purification using Alumina was not successful in my experiments. Further purification might be possible with the use of functionalised beads (Sec. 4.3.4).

The use of the Wilhelmy plate gives rise to additional difficulties. The wetting of the platinum Wilhelmy plate at the interface between water and squalane is not homogeneous (Fig. 3.7). This is improved slightly, if the plate is wetted with water before being brought to the interface. However, when experiments are performed in this way, it is unclear if the contact angle of the water on the platinum Wilhelmy plate is zero over the whole contact length or if it deviates from this value introducing errors. Experiments with the paper Wilhelmy plate were able to improve the homogeneous wetting (Fig. 3.8). But due to the impurity of the squalane, I was not able to make a conclusive measurement. In future experiments a pure squalane sample and paper plate could be used to obtain reliable results. Another possible method to test the quality of these measurements is the use of the pendant drop method as comparison.

Additionally, the experiments showing biomimetic behaviour show a dependence between the movement and the pH inside the droplet likely related to the acid dissociation constant of the surfactant (pK_a), oleic acid. If the pH in relation to the acid dissociation constant plays a role in self-propulsion, it would be possible to use the fluorinated acid,

Krytox, to obtain movement as well. We performed preliminary experiments of such a system and some movement was already observed.

Summary of Section 5.2 – pH and self-propulsion of droplets

For the understanding of our minimal system showing self-propulsion, a characterisation of the surfactant solution (oleic acid in squalane) is necessary. The determination of the exact critical micellar concentration of oleic acid in squalane remains challenging as the purification of squalane was not yet successful.

For studying interfacial properties it is of great relevance that the used solvents do not contain interface active contaminants. Such contaminants are present in the squalane used here. Further studies using squalane should thus systematically analyse impurities in commercially available solvents before concluding on interfacial properties.

The ongoing experiments to define the dependence of the buffer conditions and the surfactant on the movement of droplets could lead to a link between the kinetics of surfactant adsorption and other interfacial phenomena.
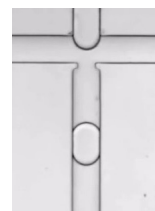
5.3 Monodisperse particle synthesis

I focussed so far on the transport of surfactants towards the interface. In other applications, droplets need to be stabilised against exchange as well. For example, microgels can be obtained through polymerisation of emulsion droplets. An exchange between droplets could lead to undesired cross-linking between them. As before, surfactant properties are of great relevance to stabilise these interfaces.

5.3.1 Materials and methods

Within the collaboration with Ramsia Sreij[2], I was involved designing the microfluidic chips for the on-chip production of monodisperse smart microgel particles. The collaboration included the chip-design, the production of the molds and the production of the PDMS devices. The chips contained several features, e. g. a flow-focusing geometry for proper droplet production, a delay line for longer reaction time, and an expansion chamber for droplet storage and analysis. The designs ranged from a basic 2-inlet (2 reactants) device to study polymerisation through diffusion, to a 3-inlet and a 4-inlet device to study polymerisation using water-in-oil droplet-based microfluidics (2 reactants + 1 oil and 2 reactants + 1 buffer + 1 oil, respectively). The droplets function as reaction vessels. They were stabilised by a fluorinated surfactant (PFPE-PEG-PFPE) which was synthesised and provided by me (Sec. 3.5). The first experiments of the synthesis of monodisperse Poly(N-isopropylacrylamide) (pNIPAM) particles were performed on-chip. The final aim is to determine the kinetics of polymerisation.

5.3.2 Results and discussion

The on-chip synthesis via water-in-oil droplet-based microfluidics leads to monodisperse microgels in the micrometer range. The production is stable using channels between 40 μm and 100 μm. The droplets are successfully stabilised with the synthesised PFPE-PEG-PFPE surfactant (Sec. 3.5). Upon transfer of the droplets into an aqueous phase, though, the droplets partially coalesce. This is due to the nature of the surfactant having

---

[2]From the group of Prof. Dr. Thomas Hellweg, Physical and Biophysical Chemistry, Faculty of Chemistry, Bielefeld University

suitable properties to stabilise water-in-fluorinated-oil emulsions only. Furthermore, cross-linking between droplets occurs. Adapting time and concentrations of the reactants is promising to solve these problems.

Summary of Section 5.3 – Particle synthesis

In this collaboration, we designed microfluidic devices for the production of monodisperse microgels. Using these microfluidic channels, the first monodisperse microgels were successfully produced. Ongoing experiments aim at stabilising the particles against cross-linking after transferring them from the continuous phase into an aqueous phase.
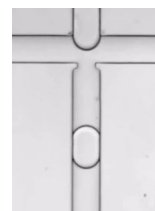
5.4 Ice nucleation in emulsion droplets

The stabilisation of emulsion droplets is of great relevance when utilising these droplets to study volume dependent properties. In such experiments, interfacial properties should not be dominant over the volume dependent properties. This is especially important when studying volume dependent ice nucleation rates. A prerequisite for these studies is the occurrence of the nucleation inside the volume and not at the interface. This depends on the interaction of the surfactant with the droplet phase. This project is a follow-up on my previous measurements on the dependence of the homogeneous ice nucleation rate on the volume of monodisperse droplets[194]. In the present work, the aim is to produce monodisperse droplets for the examination of not only homogeneous but also heterogeneous ice nucleation using different biological ice nuclei in collaboration with Katharina Dreischmeier[3].

5.4.1 Materials and methods

For these experiments we used a continuous phase of squalene or mineral oil with Span® 65, Span® 80 or Tween® 80 as surfactants tuning the concentrations and flow rates for stable droplet production on-chip. For the surface treatment of the channels, we used Nanoprotect, Aquapel or dichlorodimethylsilane.

I designed and fabricated the microfluidic chips to aim at slow droplet throughput for a camera using 25 fps. I produced a flow focussing geometry with channel width of 20 μm to 100 μm and varying nozzles sizes to obtain droplet sizes between ~15 μm and ~200 μm. 6 mm after droplet production, I added an expansion of a width of 1 mm into the chip to slow down the droplets.

5.4.2 Results and discussion

Within this work, we use different combinations of surfactants and oils including different treatments of the channels to obtain a stable droplet production including a stability upon

---

[3]From the group of Prof. Dr. Thomas Koop, Atmospheric and Physical Chemistry, Faculty of Chemistry, Bielefeld University.

the handling of these droplets off-chip. The latter includes the use of an oil phase which can be cooled down to below $-40°C$ to access the homogeneous ice nucleation temperature of pure water. Additionally, the freezing of neighbouring droplets has to be independent for the measurement of nucleation temperatures[194]. To cool down the droplets, they are placed inside a cryo-microscope. Thus, it is of advantage if the oil phase is lighter than the aqueous phase preventing the droplets from evaporation and obtaining a better contact with the cooling system. Squalene is not suitable for this, as the melting point is around -5°C[195]. For the squalene, though, the best combination of surfactant and channel treatment is found with 1.3 w% of Span® 80 with Nanoprotect, in comparison to the other combination of surfactants and oil phases. With mineral oil, the best production is obtained using 1.3 w% Span® 80. Upon freezing these droplets, the interfaces of the droplets become turbid being likely due to the behaviour of Span® 80 at the interface of mineral oil and water at these low temperatures. The future work aims towards the optimisation of the formulation of the oil-surfactant mixture before investigating ice nucleation.

Summary of Section 5.4 – Ice nucleation

In this collaboration, monodisperse droplets were produced using different organic continuous phases and different surface coatings for the microfluidic channels to find a suitable combination for the use in ice nucleation experiments. We used a cryo-microscope for the observation of the freezing events of the different emulsion droplets. In ongoing experiments, the combination of the oil phase, the surfactant and the surface coating will be optimised.
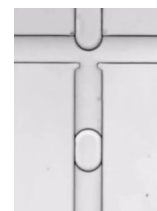
Summary of Chapter 5 – Follow-up Experiments and Collaborations

In this chapter, I have described ongoing experiments. I have developed an experiment to determine the adsorption kinetics of surfactants using the velocity of droplets in microfluidic channels. Additionally, I studied interfacial properties of a surfactant to understand self-propulsion of aqueous emulsion droplets. And finally, I initiated two collaborations with groups at the Bielefeld University to study the production of monodisperse microgels as well as homogeneous and heterogeneous ice nucleation using droplet-based microfluidics.

Chapter 6

Discussion

In this study, I investigate surfactant induced interfacial phenomena within water-in-oil emulsions. Surfactants play a crucial role in the stabilisation of emulsion droplets against coalescence[110,196]. Both at the same time, they can effect the exchange of solutes between droplets due to the intermolecular interactions with the solute[28]. Furthermore, surfactants interact with the exterior oil phase which can lead to self-propulsion of the droplet[31,86–88]. In all these processes, adsorption and desorption processes are of relevance. In my thesis, I study three aspects of surfactants: (1) emulsion stabilisation (adsorption kinetics, Sec. 4.1, 4.2, 5.1), (2) stabilisation of droplets against exchange of solutes (surfactant synthesis, Sec. 4.3, 5.3, 5.4) and (3) surfactant induced self-propulsion (properties of surfactants at interfaces, Sec. 5.2).

6.1 Kinetics of surfactant adsorption

With the use of microfluidics, I describe an efficient tool for the analysis of adsorption kinetics of surfactants to interfaces. I present a unified model for the transport of molecules across the interface and the stabilisation of interfaces (Sec. 4.2). This method overcomes the problems often encountered by standard interfacial techniques like the pendant drop or Wilhelmy plate method: inflexibility, long equilibration times, large amount of fluids[37,40,69,80] and different kinetics due to the size of the droplet[33,41] (Sec. 2.4).
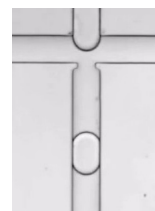
The results of the droplet-based microfluidic experiments show a direct relation between the adsorption kinetics, the transfer of molecules across interfaces and the stabilisation of emulsions (paper in preparation[43]). These results have several implications on the use of droplet-based microfluidics for the implementation in biotechnology. Aside from the stabilisation of the droplets against coalescence, biotechnological applications require the conditions inside the droplets to be constant[7,8,18,25,55,56] (Sec. 2.1). I have shown that interfacial stabilisation against coalescence by surfactants is only achieved for almost completely covered interfaces. Additionally, I demonstrated that stable conditions inside droplets are not always achieved: Depending on the surfactant, a pH change and a loss of ions take place within the order of seconds.

In fact, not only do surfactants influence droplet stability, but they also act on the droplet composition[28]. The composition change is seen with different surfactants such as tri-block copolymers[28,61]. In my study, I used an acidic surfactant which changes the pH inside the buffered aqueous emulsion droplets drastically, due to a deprotonation of all surfactant molecules present in the fluorous phase. This results in a conversion of all carboxylic acid molecules to their salt. This conversion can only take place if the surfactant molecules adsorb to the interface and subsequently desorb with another ion from the aqueous phase. This leads to the drastic pH change and a depletion of salt from the emulsion droplets.

A pH change to this extent can lead to an environment which is not suitable for encapsulated biological material. This applies also to the loss of salt from the droplets in which biological material is encapsulated[7]. One can argue, that a pure carboxylic acid, such as the KrytoxFSL in this study, is rarely used as surfactant. It has to be noted, though, that when working with a fluorinated continuous phase the surfactant is usually synthesised from this acid. Only traces of such an acid can already be an issue as seen by the following thought experiment. In common droplet-based microfluidic experiments, the amount of surfactant used is around 2 w%[14,99,197], whereas the maximum concentration of the carboxylic acid surfactant used for the pH measurements was only 0.07 w% (Fig. 4.10). Hence, an impurity (carboxylic acid) of less than 4 w% is enough to achieve this outcome in equilibrium. Furthermore, this transfer can be completed in less than 10 s, depending on the concentration of the impurity and the competition of all surface active molecules.

As a consequence, the purity of the surfactant is a crucial parameter to consider when using droplet-based microfluidics.

The effect of pH change might also be used as an advantage. To trigger a reaction inside a droplet, a conventional method is selective droplet fusion[16,115,116,198] with the disadvantage of a volume change of the droplets[198]. To overcome this, Mashaghi *et al.*[198] used an acid soluble in the aqueous and the oil phase to externally control the pH of the droplets. They achieved a pH change in the order of seconds. In principle, such a pH change should also be obtainable using my system, but further work is needed here to tune the surfactant concentrations and compositions. With the system I developed here, a pH change is induced upon exchanging an ion from the aqueous phase with a proton from the surfactant in the oil phase. In contrast to the previous study[198], no other molecule is added to the aqueous phase. This is advantageous as my system does not introduce additional molecules into the aqueous phase triggering no additional side products or interactions with the reactants inside the aqueous phase. The pH change only reduces the amount of positive ions inside the droplets. Controlling the pH change or pH stability is only possible with the quantitative information I gain from the adsorption measurements.

Now, with a qualitative sense of the importance of surfactant adsorption in mind, I will quantify the pH change by examining the adsorption isotherms. Adsorption kinetics on the micron scale are highly discussed in the literature since the 1930s[40]. Many studies explain the adsorption kinetics with two limiting cases either limited by diffusion or by adsorption with an adsorption barrier. These studies are often only empirical and introduce large errors[40]. To overcome these difficulties, a recent approach consists of predicting surface tension data using inputs of experimental data[38]. The identification of an adsorption barrier is very complex as the kinetics are often very similar to the diffusion limited regime[40]. However, it was shown, that the kinetics of surfactant adsorption on emulsion droplets change with the size of the droplets[41]. Upon reducing the droplet size, the diffusion limited regime for the adsorption kinetics crosses over to the limiting regime including an adsorption barrier[41]. Reducing the size of emulsion droplets and measuring the kinetics in flow gives rise to the kinetic limited adsorption of surfactants[33,41]. Therefore, I used small scale pH measurements in flowing droplets
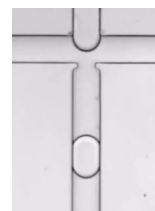
to obtain information on the kinetic limited adsorption. To obtain absolute values, I implemented equilibrium interfacial tension data.

These kinetic measurements have shown, that the adsorption of the surfactant to the interface is not a simple first order Langmuir adsorption process (Sec. 4.2.4, 4.2.5). The speed of adsorption rather scales quadratically with the concentration of the surfactant inside the oil phase (Fig. 4.9, 4.10), which might be related to dimerisation of the carboxylic acid molecules inside the fluorous phase[155]. Quantitatively, my model does not change the value of the maximum coverage of the interface obtained from large volume interfacial tension data (Fig. 4.4, Eq. 4.7). In contrast to these bulk interfacial tension experiments, my microfluidic method can distinguish between possible isotherm models.

From the pH measurements, I extract a value for the adsorption constant k_{ads} for a process occurring at a timescale of several seconds. I can relate these kinetics to the short-time kinetics of the adsorption of surfactants to interfaces obtained from coalescence experiments even though the timescale for the stabilisation of the droplets' interfaces is one or two orders of magnitude smaller (of the order of tens of milliseconds). I find that for a stable emulsion, the coverage of the interface needs to be close to ($\geq$ 90% of) the equilibrium coverage. The equilibrium coverage for surfactant concentrations above the CMC, used in these experiments, is close to 100%. Thus, a stabilisation of the emulsion can only be achieved using surfactant concentrations very close to or larger than the CMC (Sec. 4.2.7). In previous coalescence experiments for a surfactant with the same tail as used in my study and with the hydrophilic group dimorpholino phosphate, the value above which stabilisation takes place was found to be around 10% of the maximum coverage[110]. Unlike my experiments, this value was obtained considering diffusion limited adsorption, whereas the adsorption limited kinetics were neglected.

The dynamic processes at the interfaces describe the equilibrium of the chemical potential across the interface leading to the extraction of counter ions from the aqueous phase upon transfer of protons towards this phase. Previously, it was shown that no barrier to partitioning is present for timescales of about 45 seconds, meaning that the timescale of such a barrier is smaller[61]. In my study, the equilibrium of the complete transfer of ions from one phase to the other is reached with timescales of the order of seconds (~5 s, Fig. 4.10). Due to the steady-state in equilibrium, the extraction of ions and the

pH variation have the same timescales (Eq. 4.4). Thus, I expect the extraction of small solutes (such as dyes and counter ions) to occur in a couple of seconds as well, as observed in other experiments[61]. The timescale of the extraction will depend on the affinity of the surfactant molecules with the different solutes available. The amount of molecules extracted depends on the chemical interactions and the stoichiometry of the surfactant molecules bound to the solutes[8,61].

In summary, the analysis of the adsorption kinetics of the surfactant, perfluoropolyether carboxylic acid (KrytoxFSL), towards the water-fluorinated-oil interface shows that the speed of adsorption scales quadratically with the concentration. Additionally, the adsorption of the acid surfactant gives rise to a pronounced pH change and loss of ions from the aqueous phase.

6.2 Surfactant synthesis

The analysis of the kinetics of surfactant adsorption and pH change show the importance of the control of surfactant purity and contents. For water-in-fluorinated-oil emulsions, PFPE-PEG-PFPE surfactants are often used[7]. These surfactants are generally synthesised from the PFPE carboxylic acid and a primary PEG-diamine[143,161,162,184,199]. As mentioned in the last section, already 4 w% of residual PFPE-carboxylic acid inside the synthesised surfactant are enough to obtain a pH change of the order of 1. Thus, a high purity of the surfactant is of great relevance.

The aim of this study was to improve the surfactant synthesis and develop a method to determine the purity (Sec. 4.3). In previous studies, the occurrence of the reaction was proven, using ^{19}F-NMR[143,161,184,199] or IR spectroscopy[161,162]. Only in the study of Holtze *et al.*[143], the purity was given to be 80 w%. As discussed in Appendix E, the relevant signals in the ^{19}F-NMR spectra and their chemical shifts can hardly give accurate quantitative information. This is mainly due to the low intensities of the relevant signals. The IR spectra qualitatively show if the synthesis product still contains the reactant carboxylic acid (Fig. 4.14). Big differences in impurities are visible as well. It is challenging to obtain highly quantitative information using the IR spectra as the signals
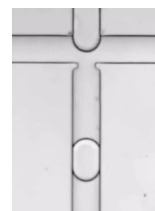
of the impurity and product overlap. The partitioning experiments developed before[185], give further information on the amount of left-over carboxylic acid.

I measured the amount of carboxylic acid using the interaction with a dye Rhodamine 6G and the extraction of this dye from the aqueous phase towards the oil phase (Fig. 4.16, 4.17). Using the partitioning, I have shown that the synthesised products have low amounts of residual carboxylic acid (KrytoxFSL) of less than 1 w% (Fig. 4.18). The obtained surfactant is biocompatible as shown in preliminary experiments to culture bacteria (E. coli Rosetta DE3) and to perform reverse transcription. The analysis of my products has shown the same properties and impurities than the product synthesised by E. Mayot included in our paper P. Gruner, B. Riechers *et al.*[61] (in press 2015). The latter being usable for on-chip manipulation of droplets (sorting, trapping, incubation, picoinjection). Even though the surfactant is of great purity, the exchange of dyes between droplets still takes place and depends on the surfactant concentration[61,185]. The exchange is described with one parameter being the partitioning of the dye[61,185]. This partitioning depends on the concentration of the carboxylic acid inside the surfactant, and thus, the impurity due to the synthesis (Sec. 4.3.3). Additionally, the dye also interacts with other functional groups such as the amine of the PEG affecting the partitioning of the dye towards the fluorous phase as well.

Further purification of the synthesised surfactant could lead to an even higher quality surfactant. Filtering the surfactant twice only decreases the yield and does not improve the purity. The purification with functionalised beads is promising (Sec. 4.3.4). Up to now though, I only achieved the complete removal of all surfactants from the solution with these beads.

With the improved synthesis of the PFPE-PEG-PFPE surfactant, non-leaking microreactors can be obtained and used for more extensive biotechnological applications.

Summary of Chapter 6 – Discussions

In general, I have demonstrated here, that microfluidics is an essential tool to analyse interfacial processes with capabilities being way beyond standard techniques.

A better knowledge on molecular transport, on interfacial stabilisation and on surfactant induced self-propulsion using one single surfactant, KrytoxFSL, paves the way towards a more complete understanding of the effect of surfactants at interfaces. Further experiments on different surfactants will facilitate the use of emulsion droplets as single microreactors and support the advancement of microfluidics for industrial biotechnological, pharmaceutical and medical applications.
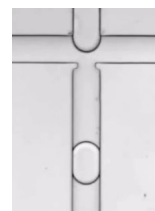
Chapter 7

Conclusions and Outlook

In this work, I studied the impact of surfactants on interfacial phenomena out of equilibrium. I investigated three different effects, (1) the stabilisation of interfaces upon surfactant adsorption (adsorption kinetics), (2) the interaction of the surfactant with the interior of the droplet (surfactant synthesis) and (3) the interaction of the surfactant with the exterior of the droplet (interfacial flows). Parts of this chapter are included in the papers P. Gruner, B. Riechers *et al.*[61] (in press 2015) and B. Riechers *et al.*[43] (in preparation 2015).

7.1 Conclusions

Adsorption kinetics of surfactants are of relevance for the stabilisation of interfaces against coalescence and transport. I investigated the adsorption kinetics of the acidic surfactant KrytoxFSL to the interface of water-in-fluorinated-oil emulsions using droplet-based microfluidics. The surfactant, which is soluble inside the fluorous continuous phase, adsorbs to the interface of the aqueous droplet after droplet production. Upon adsorption the surfactant deprotonates causing a change in the pH inside the aqueous phase containing a buffer. I measured this pH change with a pH dependent dye using a fluorescence setup. The age of the droplet can be related to the distance from the production unit on chip. The pH change provides information on the adsorption kinetics of the surfactant.
The pH change is faster and more pronounced the higher the initial surfactant concentra-

tion inside the fluorous phase. This relation was determined for surfactant concentrations above the CMC (4 ± 1 µmol/L). For the highest concentration investigated in this study ($C = 0.69$ mM $\equiv 0.07$ w% in oil), the pH change induced through the adsorption is even larger than 1 and is obtained within the order of seconds. The equilibrium change in proton concentration inside the aqueous phase equals the surfactant concentration that was initially inside the fluorous phase. The pH change results from the adsorption of the acidic surfactant to the interface, its deprotonation, the subsequent formation of the salt with a counter ion from the aqueous phase (Na^+) and the desorption of this surfactant from the interface. Thus, the transfer of protons and other ions across the interface is related to their partitioning between the two phases. The adsorption / desorption process is quantitatively linked with the kinetics of partitioning.
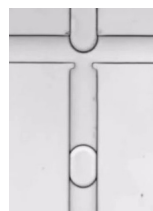
At small length scales, the adsorption process of the surfactant to the interface is slower than the diffusion of surfactant molecules towards the interface, causing the adsorption process to be rate limiting[33,41]. Thus, the kinetics of the adsorption process of surfactants are accessible using droplet-based microfluidic experiments. To measure the adsorption kinetics, I used the pH change as an indicator for the amount of adsorbed acidic surfactant to the initially empty, and at a later stage partially and then fully, covered interface. Describing the surfactant adsorption with a simple first order Langmuir model fails, because the rate of adsorption does not scale linearly, but rather quadratically with the surfactant concentration. The adsorption rate constant can be obtained applying the second order adsorption model developed here with the proviso that the equilibrium surfactant coverage is independently determined through standard measurements. Additionally, the adsorption model gives information on the timescale of the adsorption process. The pH change and the partitioning take place with a timescale of the order of one second. Therefore, phase partitioning across the interface is always in equilibrium for any process occurring at larger timescales. At smaller timescales the dynamics of surfactants at the interface have to be taken into account. The timescale of partitioning (and pH change, Eq. 4.6) increases with the radius of the droplet R and decreases with the typical speed $k_{ads}C_0(\Gamma_\infty - \Gamma_{eq})$, which depends on the adsorption constant k_{ads}, the concentration of the surfactant C_0 and the free sites at the interface $\Gamma_\infty - \Gamma_{eq}$. The timescale of partitioning is at least one or two orders of magnitude larger than the timescale for the stabilisation of the interface $(k_{ads}C^2 + k_{des})^{-1}$ obtained from coalescence experiments. Combining these results it is found that the stabilisation of two interfaces against coalescence is only possible for

surfactant concentrations close to or larger than the CMC.

The maximum interfacial coverage is accessible from standard bulk interfacial tension measurements by applying a model for the adsorption kinetics. The Langmuir and the second order adsorption model provide the same value for the maximum interfacial coverage ($\Gamma_\infty = 8 \pm 1\ \mu mol/m^2$). Hence, bulk interfacial tension techniques cannot distinguish between different adsorption isotherms which is in contrast to the microfluidic method developed in this study.

As demonstrated, the pH change is due to an acidic surfactant (Krytox) adsorbing to the interface at any time during the experiment. Small amounts of residual acid in another surfactant lead to a pH change of the droplet (e. g. a pH change of the order of one with 4w% of residual acid). Accordingly, acid free surfactants are crucial for the use in emulsion stabilisation. The typical surfactant used in droplet-based microfluidics is usually synthesised from such an acidic surfactant[143,161,162,184]. Hence, a high purity of the synthesised surfactant is required. The product quality depends on the residual acidic surfactant. Additionally, this impurity (acidic surfactant) needs to be quantified for a reliable use of the synthesised surfactants for the stabilisation of emulsions. In this work, I improved the synthesis showing the crucial role of inert atmospheric conditions[61]. I characterised the purity of the synthesised surfactant using infrared spectroscopy and partitioning experiments between an aqueous phase and a fluorous phase. The partitioning experiments are bulk measurements and determine the amount of water soluble dye (Rhodamine 6G) extracted towards a fluorous phase in which the surfactant is dissolved. The amount of extracted dye correlates directly with the amount of residual carboxylic acid (acidic surfactant) present inside the surfactant. I found that my synthesised surfactants show a partitioning corresponding to less than 1 w% contamination of carboxylic acid. The purity of the final product is therefore of the order of 99 w%. With the improvement of the synthesis and the possibility to characterise the amount of residual carboxylic acid, a more reliable production of surfactants for emulsion stabilisation becomes feasible.

Adsorption of surfactants to interfaces influence the behaviour of droplets in emulsions. Out-of equilibrium dynamics at interfaces can lead to the Marangoni effect, which couples inhomogeneities of the surfactant distribution at the interface to interfacial flows and can lead to self-propulsion of droplets. The self-propulsion of droplets is directly linked to the dynamics of surfactants at interfaces and thus to the adsorption kinetics of surfactants.
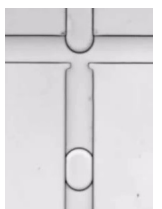
To obtain further insight into the relation between self-propulsion and surfactant adsorption, I studied interfacial properties of aqueous droplets in a squalane continuous phase. These droplets show biomimetic behaviours (ongoing experiments) such as swimming, deformation (ameoba-like), division or microemulsification of the droplet or formation of a shell around the droplet. These different behaviours depend on the concentration of the solutes inside the aqueous phase (of TrisHCl, Ca^{2+}) and on the concentrations of the surfactant oleic acid inside the oil phase. In this system, the movement of the droplet is likely related to the pH of the droplet (due to TrisHCl) and the pK_a of the oleic acid. The characterisation of the temporal evolution of the interfacial tension and its dependence on the concentration of the oleic acid, including the determination of the CMC, is of great relevance for the understanding of these behaviours. These measurements are challenging, due to the impurity present in the oil from the supplier. Purifications upon filtering over Celite® or Alumina do not remove all impurities. Therefore, the determination of the CMC, 40 μmol/L, is only a rough estimate on the preliminary data.

In additional experiments, I developed a microfluidic device to study the evolution of the droplet velocity upon surfactant adsorption. Due to height variations of the microfluidic channels, no final conclusion on the Marangoni effect was obtained so far.

These two ongoing experiments are promising to gain insight into the interplay of the interfacial flow and the adsorption kinetics of surfactants.

7.2 Outlook

I determined the adsorption kinetics of the surfactant KrytoxFSL using pH measurements at the micron scale. This method can now be employed to systematically explore the kinetics of homologous surfactants where the size of the molecular tail can be investigated (e. g. KrytoxFSH instead of KrytoxFSL) while retaining the same headgroup (the carboxylic acid). This can lead to a direct measurement of the influence of the chain length on the adsorption dynamics including the influence on the adsorption rate and the interfacial equilibrium coverage.

The self-propulsion of droplets depends also on the timescale of surfactant adsorption. Furthermore, the movement correlates with the pH inside the droplet and potentially with the pK_a of the oleic acid used as surfactant. Thus, the utilisation of other acids might

also induce self-propulsion. Preliminary results using KrytoxFSL as the acidic surfactant and a droplet at low pH are promising and need further investigation.

The amount of residual carboxylic acid in the synthesised surfactant is relevant for the equilibrium value of partitioning and pH change. The timescale of adsorption of these two surfactants will depend on the competition between the synthesised surfactant and the acidic surfactant. The adsorption of the pure acidic surfactant will be the lower boundary for the timescale of pH change occurring with a surfactant mixture. The pH change of a mixture of the synthesised surfactant with different amounts of carboxylic acid should give further insight into the adsorption kinetics of surfactant mixtures.

At equilibrium each carboxylic acid molecule leads to the partitioning of one counter ion or one Rhodamine 6G molecule towards the fluorous phase. Less partitioning would occur, if the interaction was less pronounced. Thus, the interactions with other functional groups, such as amines, present in the synthesised surfactant have to be considered as well. Any interaction will lead to the transfer of small molecules from the aqueous phase towards the fluorous phase. To obtain further information on the strength of the interactions a surfactant containing only one type of functional group should be analysed. To the best of my knowledge, the simple perfluorocarbon amine is not commercially available. Thus, a more suitable approach could be to synthesise the same PFPE-PEG-PFPE surfactant as before, but using a stoichiometric ratio which leads to free amine groups. From this, a mixture of the di-functionalised and mono-functionalised PEG should be obtained. Using the pH measurements information on the interaction strength of the amine and small organic molecules should be accessible.

In my thesis, I have shown the role of surfactants in droplet-based microfluidics. These surfactants play a key role in the transport of molecules across interfaces, in the stabilisation of interfaces as well as in self-propulsion of droplets. Controlling these interfacial processes can lead to the development of new and more extensive biotechnological applications using emulsion droplets.
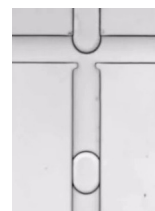
Appendix A

Maximum interfacial coverage

In this chapter, I show that the slope of the equilibrium interfacial tension with $\ln C$ is given by $-RT\Gamma_\infty$ for the Langmuir adsorption process as well as for the second order process. I derive Equation 2.22 from Equation 2.4 and 2.21 for the Langmuir adsorption process[39] (Sec. A.1) and Equation 4.8 from Equation 2.4 and 4.7 for the second order process (Sec. A.2).

A.1 Langmuir adsorption model

$$\Gamma_{eq} = -\frac{1}{RT}\frac{d\gamma_{eq}}{d\ln C} \tag{2.4}$$

$$\Gamma_{eq} = \Gamma_\infty\frac{\kappa C}{1 + \kappa C} \tag{2.21}$$

$$\Gamma_\infty\frac{\kappa C}{1 + \kappa C} = -\frac{1}{RT}\frac{d\gamma_{eq}}{d\ln C} \tag{A.1}$$

Using $d\ln C/dC = 1/C$ leads to:

$$\Gamma_\infty\frac{\kappa C}{1 + \kappa C} = -\frac{C}{RT}\frac{d\gamma_{eq}}{dC} \tag{A.2}$$

$$d\gamma_{eq} = -\Gamma_\infty\frac{\kappa}{1 + \kappa C}RTdC \tag{A.3}$$

With $d\ln(1 + \kappa C)/dC = \kappa/(1 + \kappa C)$, I obtain:

$$d\gamma_{eq} = -\Gamma_\infty RTd\ln(1 + \kappa C) \tag{A.4}$$

$$\gamma_{eq} = -\Gamma_\infty RT\ln(1 + \kappa C) + \text{const} \tag{A.5}$$
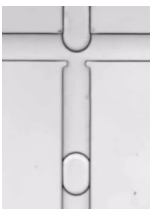
For $C = 0$, $\gamma_{eq} = \gamma_0.$, Therefore,

$$\gamma_{eq} = \gamma_0 - \Gamma_\infty RT \ln(1 + \kappa C) \tag{2.22}$$

If $\kappa C \gg 1$,

$$\gamma_{eq} \sim \gamma_0 - \Gamma_\infty RT \ln \kappa C \tag{A.6}$$

A.2 Second order adsorption model

The derivation for the second order adsorption process is analogue to the Langmuir adsorption process.

$$\Gamma_{eq} = -\frac{1}{RT} \frac{d\gamma_{eq}}{d \ln C} \tag{2.4}$$

$$\Gamma_{eq} = \Gamma_\infty \frac{\kappa C^2}{1 + \kappa C^2} \tag{4.7}$$

$$\Gamma_\infty \frac{\kappa C^2}{1 + \kappa C^2} = -\frac{1}{RT} \frac{d\gamma_{eq}}{d \ln C} \tag{A.7}$$

Using $d \ln C/dC = 1/C$ gives:

$$\Gamma_\infty \frac{\kappa C^2}{1 + \kappa C^2} = -\frac{C}{RT} \frac{d\gamma_{eq}}{dC} \tag{A.8}$$

$$d\gamma_{eq} = -\frac{1}{2} RT\Gamma_\infty \frac{2\kappa C}{1 + \kappa C^2} dC \tag{A.9}$$

Substituting $d \ln(1 + \kappa C^2)/dC = 2\kappa C/(1 + \kappa C^2)$ gives:

$$d\gamma_{eq} = -\frac{1}{2} RT\Gamma_\infty d \ln(1 + \kappa C^2) \tag{A.10}$$

$$\gamma_{eq} = -\frac{1}{2} RT\Gamma_\infty \ln(1 + \kappa C^2) + const \tag{A.11}$$

At $C = 0$, $\gamma_{eq} = \gamma_0$. Thus,

$$\gamma_{eq} = \gamma_0 - \frac{1}{2} \Gamma_\infty RT \ln(1 + \kappa C^2) \tag{4.8}$$

If $\kappa C^2 \gg 1$:

$$\gamma_{eq} \sim \gamma_0 - \frac{1}{2} \Gamma_\infty RT \ln \kappa C^2 \tag{A.12}$$

$$\sim \gamma_0 - \Gamma_\infty RT \ln \kappa C \tag{A.13}$$

Appendix B

Titration curves

In the following, I calculate the titration curves of monoprotic and triprotic acids and bases. The calculations are based on Dick[186] and Bliefert *et al.*[187].

B.1 Monoprotic substance

I calculate the change of pH when titrating a monoprotic acid HAc or base Ac^-.
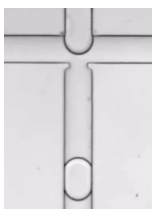
B.1.1 Monoprotic acid

The monoprotic acid HAc is titrated by a strong base, NaOH, to obtain the base Ac^-:

$$HAc + H_2O \rightleftharpoons Ac^- + H_3O^+ \qquad (K_1)$$

$$NaOH \rightarrow Na^+ + OH^-$$

$$H_2O \rightleftharpoons H_3O^+ + OH^- \qquad (K_w)$$
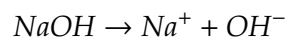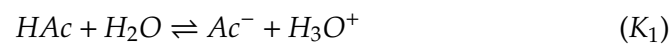
The auto-dissociation constant of water K_w and the acid dissociation constant K_1 are defined as:

$$K_1 = \frac{[Ac^-][H_3O^+]}{[HAc]} \qquad (B.1)$$

$$K_w = [H_3O^+][OH^-] \qquad (B.2)$$

with [x] denoting the concentration of x. Additionally, charge and mass conservation lead to:

$$[OH^-] + [Ac^-] = [H_3O^+] + [Na^+] \tag{B.3}$$

$$[HAc]_s = [HAc] + [Ac^-] \tag{B.4}$$

with the subscript s as the new 'starting' concentration for each titration step. The relative amount of each species α is given by:

$$\alpha_{Ac^-} = \frac{[Ac^-]}{[HAc]_s} \tag{B.5}$$

$$\alpha_{HAc} = \frac{[HAc]}{[HAc]_s} \tag{B.6}$$

$$\alpha_{Ac^-} \overset{B.4}{=} \frac{[Ac^-]}{[Ac^-] + [HAc]} \overset{B.1}{=} \frac{[Ac^-]}{[Ac^-] + \frac{[Ac^-][H_3O^+]}{K_1}} = \frac{K_1}{K_1 + [H_3O^+]} \tag{B.7}$$

$$\alpha_{HAc} = \frac{[H_3O^+]}{K_1 + [H_3O^+]} \tag{B.8}$$

Inserting Equations B.2, B.5, B.7 into Equation B.3 gives:

$$\frac{K_w}{[H_3O^+]} + [HAc]_s \frac{K_1}{K_1 + [H_3O^+]} - [H_3O^+] = [Na^+]_s \tag{B.9}$$

Solving this equation, leads to:

$$[H_3O^+]^3 + [H_3O^+]^2([Na^+]_s + K_1) + [H_3O^+](K_1([Na^+]_s - [HAc]_s) - K_w) - K_wK_1 = 0 \tag{B.10}$$

With this equation, the concentration of protons in relation to the amount of base NaOH used for the titration is obtained.

B.1.2   Monoprotic base

The same approach as for the monoprotic acid (Appendix B.1.1) applies for the monoprotic base Ac^-, titrated with a strong acid HCl

$$Ac^- + H_2O \rightleftharpoons HAc + OH^- \qquad (K_{1b})$$

$$HCl + H_2O \rightarrow H_3O^+ + Cl^-$$

$$H_2O \rightleftharpoons H_3O^+ + OH^- \qquad (K_w)$$
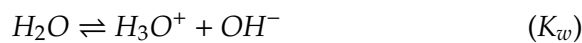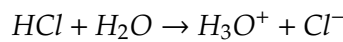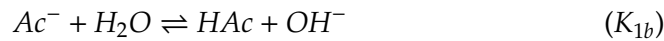
with the base dissociation constant:

$$K_{1b} = \frac{[HAc][OH^-]}{[Ac^-]} \tag{B.11}$$

Using the exact same approach as above:

$$\alpha_{Ac^-} = \frac{[Ac^-]}{[Ac^-]_s} \tag{B.12}$$

$$\alpha_{HAc} = \frac{[HAc]}{[Ac^-]_s} \tag{B.13}$$

$$\alpha_{Ac^-} \overset{B.4}{=} \frac{[Ac^-]}{[Ac^-]+[HAc]} \overset{B.11}{=} \frac{[Ac^-]}{[Ac^-]+\frac{[Ac^-]K_{1b}}{[OH^-]}} = \frac{[OH^-]}{[OH^-]+K_{1b}} \tag{B.14}$$

$$\alpha_{HAc} = \frac{K_{1b}}{K_{1b}+[OH^-]} \tag{B.15}$$

Charge and mass conservation gives:

$$[H_3O^+] = [Ac^-] + [OH^-] + [Cl^-] \tag{B.16}$$

$$[H_3O^+] - [Ac^-] - [OH^-] = [Cl^-] \tag{B.17}$$

$$[H_3O^+] - [Ac^-]_s\alpha_{Ac^-} - [OH^-] = [Cl^-] \tag{B.18}$$

$$[H_3O^+] + [Ac^-]_s\alpha_{HAc} - [OH^-] = [Cl^-] \tag{B.19}$$

Inserting Equations B.2 and B.15 into Equation B.19 gives:

$$\frac{K_w}{[OH^-]} + [Ac^-]_s\frac{K_{1b}}{K_{1b}+[OH^-]} - [OH^-] = [Cl^-]_s \tag{B.20}$$

This leads to an equation analogue to Equation B.10:

$$[OH^-]^3 + [OH^-]^2([Cl^-]_s + K_1b) + [OH^-](K_{1b}([Cl^-]_s - [HAc]_s) - K_w) - K_wK_{1b} = 0 \tag{B.21}$$

This equation gives the relation between the concentration of OH^- and the amount of acid added during titration.

From the concentration of OH^- and the pOH, the pH is obtained as follows:

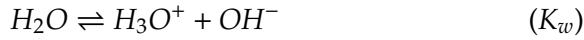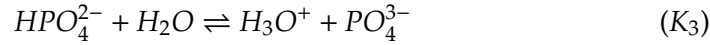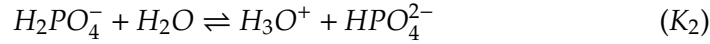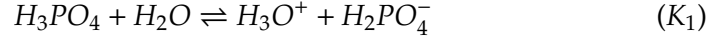$$pOH = -log_{10}[OH^-] \tag{B.22}$$

$$14 = pH + pOH \tag{B.23}$$

B.2 Triprotic substance

In the following, I calculate the change in pH for the titration of a triprotic substance, here, phosphoric acid H_3PO_4 or its salt PO_4^{-3}.
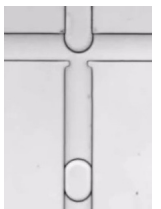
B.2.1 Triprotic acid

I use the same approach as for the monoprotic acid (Appendix B.1) using the triprotic phosphoric acid H_3PO_4 with the dissociation constants K_{1-3} of the following reactions:

$$H_3PO_4 + H_2O \rightleftharpoons H_3O^+ + H_2PO_4^- \qquad (K_1)$$

$$H_2PO_4^- + H_2O \rightleftharpoons H_3O^+ + HPO_4^{2-} \qquad (K_2)$$

$$HPO_4^{2-} + H_2O \rightleftharpoons H_3O^+ + PO_4^{3-} \qquad (K_3)$$

$$H_2O \rightleftharpoons H_3O^+ + OH^- \qquad (K_w)$$

$$NaOH \rightarrow Na^+ + OH^-$$
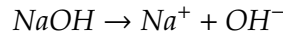
$$K_w = [H_3O^+][OH^-] \qquad (B.24)$$

$$K_1 = \frac{[H_3O^+][H_2PO_4^-]}{[H_3PO_4]} \qquad (B.25)$$

$$K_2 = \frac{[H_3O^+][HPO_4^{2-}]}{[H_2PO_4^-]} \qquad (B.26)$$

$$K_3 = \frac{[H_3O^+][PO_4^{3-}]}{[HPO_4^{-2}]} \qquad (B.27)$$

Charge conservation leads to:

$$[OH^-] + 3[PO_4^{3-}] + 2[HPO_4^{2-}] + [H_2PO_4^-] = [H_3O^+] + [Na^+] \qquad (B.28)$$

The relative amount α of the different species (H_3PO_4, $H_2PO_4^-$, HPO_4^{2-}, PO_4^{3-}) in solution is:

$$\alpha_{H_3PO_4} = \frac{[H_3O^+]^3}{[H_3O^+]^3 + [H_3O^+]^2K_1 + [H_3O^+]K_1K_2 + K_1K_2K_3} \qquad (B.29)$$

$$\alpha_{H_2PO_4^-} = \frac{[H_3O^+]^2K_1}{[H_3O^+]^3 + [H_3O^+]^2K_1 + [H_3O^+]K_1K_2 + K_1K_2K_3} \qquad (B.30)$$

$$\alpha_{HPO_4^{2-}} = \frac{[H_3O^+]K_1K_2}{[H_3O^+]^3 + [H_3O^+]^2K_1 + [H_3O^+]K_1K_2 + K_1K_2K_3} \qquad (B.31)$$

$$\alpha_{PO_4^{3-}} = \frac{K_1K_2K_3}{[H_3O^+]^3 + [H_3O^+]^2K_1 + [H_3O^+]K_1K_2 + K_1K_2K_3} \qquad (B.32)$$

Using the same procedure as for the monoprotic acid/base leads to the relation between
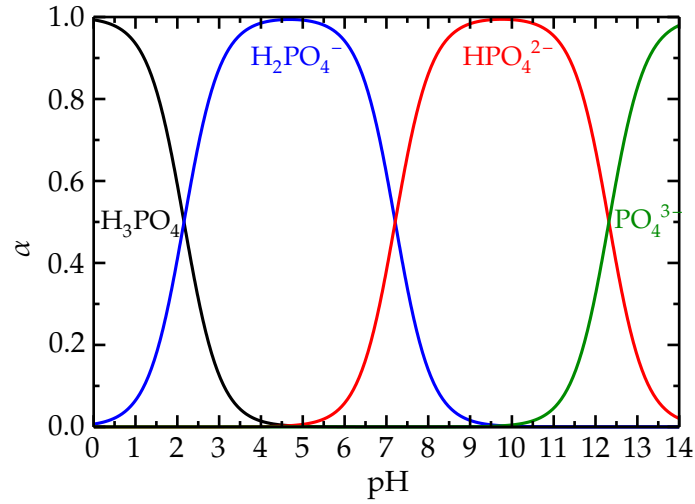
Figure B.1: The fractional composition α of the species of the triprotic acid (see colours) at a pH between 0 and 14, calculated using Equations B.29 - B.32.

the $[H_3O^+]$ and $[Na^+]_s$:

$$
\begin{aligned}
0 =& [H_3O^+]^5 \\
&+ [H_3O^+]^4(K_1 + [Na^+]_s) \\
&+ [H_3O^+]^3(K_1([Na^+]_s - [H_3PO_4]_s) + K_1K_2 - K_w) \\
&+ [H_3O^+]^2(K_1K_2([Na^+]_s - 2[H_3PO_4]_s) + K_1K_2K_3 - K_wK_1) \\
&+ [H_3O^+](K_1K_2K_3([Na^+]_s - 3[H_3PO_4]_s) - K_wK_1K_2) \\
&- K_wK_1K_2K_3
\end{aligned}
\tag{B.33}
$$

If the change in proton concentration is accompanied by a dilution of the solutes (as with titration), the concentration of the different species with subscript s changes in relation to the start concentration denoted as subscript 0 with the start volume V_0 and the volume added upon titration V_t:
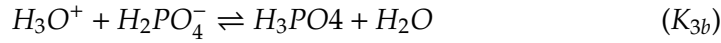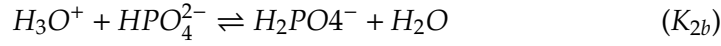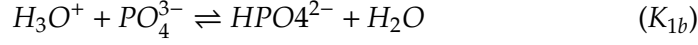
$$
[Na^+]_s = \frac{V_t[Na^+]_0}{V_t + V_0}
\tag{B.34}
$$

$$
[H_3PO_4]_s = \frac{V_0[H_3PO_4]_0}{V_t + V_0}
\tag{B.35}
$$
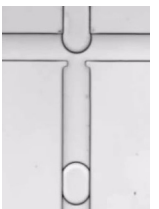
B.2.2   Triprotic base

The tripotic base PO^{3-} gives the dependence of the OH$^-$ concentration upon titration analogous to the triprotic acid (Appendix B.2.1) with the base dissociation constants K_{1b-3b}:

$$H_3O^+ + PO_4^{3-} \rightleftharpoons HPO4^{2-} + H_2O \qquad (K_{1b})$$

$$H_3O^+ + HPO_4^{2-} \rightleftharpoons H_2PO4^- + H_2O \qquad (K_{2b})$$

$$H_3O^+ + H_2PO_4^- \rightleftharpoons H_3PO4 + H_2O \qquad (K_{3b})$$

$$H_2O \rightleftharpoons H_3O^+ + OH^- \qquad (K_w)$$

$$HCl + H_2O \rightarrow Cl^- + H_3O^+$$
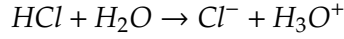
$$K_{1b} = \frac{K_w}{K_1} \qquad (B.36)$$

$$K_{2b} = \frac{K_w}{K_2} \qquad (B.37)$$

$$K_{3b} = \frac{K_w}{K_3} \qquad (B.38)$$

$$(B.39)$$

$$
\begin{aligned}
0 =& [OH^-]^5 \\
&+ [OH^-]^4 (K_{1b} + [Cl^-]_s) \\
&+ [OH^-]^3 (K_{1b}([Cl^-]_s - [PO_4^{3-}]_s) + K_{1b}K_{2b} - K_w) \\
&+ [OH^-]^2 (K_{1b}K_{2b}([Cl^-]_s - 2[PO_4^{3-}]_s) + K_{1b}K_{2b}K_{3b} - K_wK_{1b}) \\
&+ [OH^-](K_{1b}K_{2b}K_{3b}([Cl^-]_s - 3[PO_4^{3-}]_s) - K_wK_{1b}K_{2b}) \\
&- K_wK_{1b}K_{2b}K_{3b}
\end{aligned}
\qquad (B.40)
$$

If dilution takes place, the concentration $[Cl^-]_s$ changes with each titration step:

$$[Cl^-]_s = \frac{V_t[Cl^-]_0}{V_t + V_0} \qquad (B.41)$$

$$[PO_4^{3-}]_s = \frac{V_0[PO_4^{3-}]_0}{V_t + V_0} \qquad (B.42)$$

I use Equation B.40 (without dilution) to calculate the pH inside the droplets upon 'titration' with the surfactant KrytoxFSL.

Appendix C

First and second order kinetics

In this chapter I derive the first (based on [2,39,40,84]) and second order kinetics used for the analysis of surfactant adsorption in more detail.

C.1   Langmuir adsorption model

In comparison to my model (Appendix C.2), the Langmuir model[2,39,40,84] is a model assuming a first order in the concentration of surfactant.

$$\frac{\partial \Gamma}{\partial t} = k_{ads} C_0 (\Gamma_\infty - \Gamma) - k_{des} \Gamma \tag{2.20}$$

The steady state at equilibrium gives:

$$\frac{\partial \Gamma}{\partial t} = 0 \tag{C.1}$$

and with $\kappa = k_{ads}/k_{des}$ leads to:

$$\Gamma_{eq} = \frac{\Gamma_\infty \kappa C_0}{1 + \kappa C_0} \tag{C.2}$$

$$\Gamma_\infty = \frac{(k_{des} + k_{ads} C_0)\, \Gamma_{eq}}{k_{ads} C_0} \tag{C.3}$$

To obtain the dependence of Γ_{eq} on the time, I integrate Equation 2.20 using Equation C.3 and substitution:

$$\frac{\partial \Gamma}{\Gamma_{eq} - \Gamma} = (k_{ads} C_0 + k_{des})\partial t \tag{C.4}$$
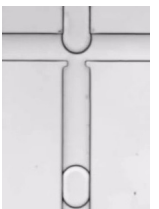
I substitute as follows:

$$x = \Gamma_{eq} - \Gamma \tag{C.5}$$

$$\frac{\partial x}{\delta \Gamma} = -1 \tag{C.6}$$

$$\frac{\partial x}{x} = -(k_{ads}C_0 + k_{des})\partial t \tag{C.7}$$

$$\ln x = -(k_{ads}C_0 + k_{des})t + \text{const}_1 \tag{C.8}$$

$$\Gamma_{eq} - \Gamma = e^{-(k_{ads}C_0 + k_{des})t} \cdot \text{const}_2 \tag{C.9}$$

$$\Gamma(t) = \Gamma_{eq} - e^{-(k_{ads}C_0 + k_{des})t} \cdot \text{const}_2 \tag{C.10}$$

At $t = 0$, $\Gamma(t) = 0$. Therefore the $\text{const}_2 = \Gamma_{eq}$. Thus, I obtain the integrated form of Equation 2.20

$$\Gamma(t) = \Gamma_{eq}(1 - e^{-\frac{t}{\tau}}) \tag{C.11}$$

with $\tau^{-1} = k_{ads}C_0 + k_{des}$.

C.2   Second order model

I integrate the following equation:

$$\frac{1}{2}\frac{V}{S}\frac{\partial [H^+]}{\partial t} = k_{ads}(C_0 - \frac{1}{q}[H^+])^2 \cdot (\Gamma_\infty - \Gamma) \tag{4.3}$$

with $V/S = R/3$:

$$\frac{\partial [H^+]_{aq}}{\partial t} = \frac{6}{R}k_{ads}(C_0 - \frac{1}{q}[H^+]_{aq})^2 \cdot (\Gamma_\infty - \Gamma) \tag{C.12}$$

Substituting as follows:

$$x = C_0 - \frac{1}{q}[H^+]_{aq} \tag{C.13}$$

$$a = \frac{6}{R}k_{ads} \cdot (\Gamma_\infty - \Gamma) \tag{C.14}$$

$$\frac{\partial x}{\partial [H^+]} = -\frac{1}{q} \tag{C.15}$$

$$-q\frac{\partial x}{\partial t} = a \cdot x^2 \tag{C.16}$$

$$-q\frac{\partial x}{x^2} = a\partial t \tag{C.17}$$

$$q\frac{1}{x} = a \cdot t + \text{const} \tag{C.18}$$

leads to

$$q\frac{1}{C_0 - \frac{1}{q}[H^+]_{aq}} = \frac{6}{R}k_{ads} \cdot (\Gamma_\infty - \Gamma) \cdot t + \text{const} \tag{C.19}$$

At $t = 0$, $[H^+] = 0$,

$$\text{const} = q\frac{1}{C_0} \tag{C.20}$$

Therefore,

$$\frac{1}{C_0 - \frac{1}{q}[H^+]_{aq}} = \frac{6}{qR}k_{ads} \cdot (\Gamma_\infty - \Gamma) \cdot t + \frac{1}{C_0} \tag{C.21}$$

$$C_0 - \frac{1}{q}[H^+]_{aq} = \frac{1}{\frac{6}{qR}k_{ads} \cdot (\Gamma_\infty - \Gamma) \cdot t + \frac{1}{C_0}} \tag{C.22}$$

$$qC_0 - [H^+]_{aq} = \frac{1}{\frac{6}{q^2R}k_{ads} \cdot (\Gamma_\infty - \Gamma) \cdot t + \frac{1}{qC_0}} \tag{C.23}$$

$$qC_0 = [H^+]_{eq} \tag{C.24}$$

$$[H^+]_{eq} - [H^+]_{aq} = \frac{[H^+]_{eq}}{\frac{6}{q^2R}k_{ads} \cdot (\Gamma_\infty - \Gamma) \cdot [H^+]_{eq} \cdot t + 1} \tag{C.25}$$

$$[H^+]_{aq} = [H^+]_{eq} - \frac{[H^+]_{eq}}{\frac{6}{qR}k_{ads} \cdot (\Gamma_\infty - \Gamma) \cdot C_0 \cdot t + 1} \tag{C.26}$$

The concentration change considered, here, is due to the transfer of protons from the oil phase, not considering the protons initially present inside the aqueous phase due to the initial pH. Thus, I rename the concentration as follows:
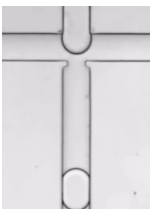
$$\Delta[H^+]_{aq} = [H^+]_{aq} \tag{C.27}$$

$$\Delta[H^+]_{eq} = [H^+]_{eq} \tag{C.28}$$

$$\Delta[H^+]_{aq} = \Delta[H^+]_{eq}\left(1 - \frac{1}{1 + \frac{6}{qR}k_{ads} \cdot (\Gamma_\infty - \Gamma) \cdot C_0 \cdot t}\right) \tag{C.29}$$

$$\Delta[H^+]_{aq} = \Delta[H^+]_{eq}\left(1 - \frac{1}{1 + \tau^{-1} \cdot t}\right) \tag{4.5}$$

$$\tau = \frac{qR}{6 \cdot k_{ads} \cdot (\Gamma_\infty - \Gamma) \cdot C_0} \tag{4.6}$$

C.2.1 Equilibrium interfacial coverage

Fitting the bulk equilibrium data using either Equation 2.22 or Equation 4.8, results in the following values:

$$\Gamma_\infty = 8 \pm 1 \cdot \mu mol \cdot m^{-2}$$

$$C_{CMC} = 4 \pm 1 \cdot mmol \cdot m^{-3}$$

$$\kappa = 7 \pm 1 \cdot 10^6 m^6 \cdot mol^{-2}$$

which leads to an equilibrium interfacial coverage Γ_{eq} of and an equilibrium interfacial coverage at the CMC Γ_{eq}^{CMC}:

$$\Gamma_{eq}^{CMC} = \Gamma_\infty \frac{\kappa C_{CMC}^2}{1 + \kappa C_{CMC}^2} \tag{4.7}$$

$$\Gamma_{eq}^{CMC} = 7.929 \cdot 10^{-6} mol \cdot m^{-2}$$

C.2.2 Adsorption rate constant

I calculate the adsorption constant k_{ads} from the slope, m (Fig. 4.10(j)), obtained from the pH experiments with a typical droplet size of $R = 80$ μm, $q = 8$ and $\Gamma_\infty - \Gamma_{eq} = 7.1 \cdot 10^{-8} mol \cdot m^{-2}$ from Equation 4.6:

$$\tau_{pH} = \frac{q\,R}{6k_{ads}C_0(\Gamma_\infty - \Gamma_{eq})} \tag{4.6}$$

$$\tau_{pH}^{-1} = \frac{6k_{ads}(\Gamma_\infty - \Gamma_{eq})}{q^2\,R}\Delta[H^+]_{eq}$$

$$m = \frac{6k_{ads}(\Gamma_\infty - \Gamma_{eq})}{q^2\,R}$$

$$= 115\frac{L}{mol\,s}$$

$$k_{ads} = 1386\frac{m^6}{mol^2\,s}$$

Appendix D

Coverage for interfacial stabilisation

In the following, I derive Equation 4.13 from Equation 4.4.

$$\frac{1}{2}\frac{\partial \Gamma}{\partial t} = k_{ads}C_0^2 \left(\Gamma_\infty - \Gamma\right) - k_{des}\Gamma \tag{4.4}$$

$$\frac{1}{2}\frac{\partial \frac{\Gamma}{\Gamma_\infty}}{\partial t} = k_{ads}C_0^2 \left(1 - \frac{\Gamma}{\Gamma_\infty}\right) - k_{des}\frac{\Gamma}{\Gamma_\infty} \tag{D.1}$$

$$\frac{\partial \frac{\Gamma}{\Gamma_\infty}}{\partial t} = 2 \cdot k_{ads}C_0^2 - 2 \cdot \frac{\Gamma}{\Gamma_\infty}\left(k_{ads}C_0^2 + k_{des}\right) \tag{D.2}$$

Substituting as follows,

$$a = 2 \cdot k_{ads}C_0^2 \tag{D.3}$$

$$b = 2\left(k_{ads}C_0^2 + k_{des}\right) \tag{D.4}$$

$$\frac{\partial \frac{\Gamma}{\Gamma_\infty}}{\partial t} = a - b \cdot \frac{\Gamma}{\Gamma_\infty} \tag{D.5}$$
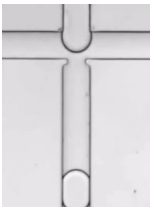
$$x = a - b \cdot \frac{\Gamma}{\Gamma_\infty} \tag{D.6}$$

$$\frac{\partial x}{\partial \frac{\Gamma}{\Gamma_\infty}} = -b \tag{D.7}$$

gives

$$-\frac{1}{b}\frac{\partial x}{\partial t} = x \tag{D.8}$$

$$\frac{1}{x}\partial x = -b\partial t \tag{D.9}$$

$$\ln x = -b \cdot t + \text{const} \tag{D.10}$$

and

$$\ln\left(2 \cdot k_{ads}C_0^2 - 2\left(k_{ads}C_0^2 + k_{des}\right)\frac{\Gamma}{\Gamma_\infty}\right) = -2\left(k_{ads}C_0^2 + k_{des}\right) \cdot t + \text{const} \tag{D.11}$$

for t = 0: $\Gamma/\Gamma_\infty = 0$

$$\text{const} = \ln\left(2 \cdot k_{ads}C_0^2\right) \tag{D.12}$$

$$\ln\left(2 \cdot k_{ads}C_0^2 - 2\left(k_{ads}C_0^2 + k_{des}\right)\frac{\Gamma}{\Gamma_\infty}\right) = -2\left(k_{ads}C_0^2 + k_{des}\right) \cdot t + \ln\left(2 \cdot k_{ads}C_0^2\right) \tag{D.13}$$

$$2 \cdot k_{ads}C_0^2 - 2\left(k_{ads}C_0^2 + k_{des}\right)\frac{\Gamma}{\Gamma_\infty} = 2 \cdot k_{ads}C_0^2 \cdot e^{-2\left(k_{ads}C_0^2 + k_{des}\right)\cdot t} \tag{D.14}$$

$$\frac{\Gamma}{\Gamma_\infty} = \frac{k_{ads}C_0^2}{k_{ads}C_0^2 + k_{des}} \cdot \left(1 - e^{-2\left(k_{ads}C_0^2 + k_{des}\right)\cdot t}\right) \tag{4.9}$$

$$\ln\left(1 - \frac{\Gamma}{\Gamma_\infty}\frac{k_{ads}C_0^2 + k_{des}}{k_{ads}C_0^2}\right) = -2\left(k_{ads}C_0^2 + k_{des}\right) \cdot t \tag{D.15}$$

In the coalescence experiments, the time $t = L/U$ is defined by the distance of the droplets to the production L and by the flow velocity U:

$$\frac{L}{U} = \frac{\ln\left(1 - \frac{\Gamma}{\Gamma_\infty}\frac{k_{ads}C_0^2 + k_{des}}{k_{ads}C_0^2}\right)}{-2\left(k_{ads}C_0^2 + k_{des}\right)} \tag{D.16}$$

$$\frac{L}{U}C_0^2 = -\frac{C_0^2}{2\left(k_{ads}C_0^2 + k_{des}\right)} \ln\left(1 - \frac{\Gamma}{\Gamma_\infty}\frac{k_{ads}C_0^2 + k_{des}}{k_{ads}C_0^2}\right) \tag{D.17}$$

with:

$$\kappa = \frac{k_{ads}}{k_{des}} \tag{D.18}$$

$$\frac{\Gamma_{eq}}{\Gamma_\infty} = \frac{\kappa C_0^2}{\kappa C_0^2 + 1} \tag{D.19}$$

$$= \frac{k_{ads}C_0^2}{k_{ads}C_0^2 + k_{des}} \tag{D.20}$$

$$\tag{D.21}$$

Thus:

$$\frac{L}{U}C_0^2 = -\frac{1}{2 \cdot k_{ads}} \cdot \frac{\Gamma_{eq}}{\Gamma_\infty} \ln\left(1 - \frac{\Gamma}{\Gamma_{eq}}\right) \tag{4.11}$$

Above the CMC, the coverage is constant and:

$$\frac{\Gamma_{eq}}{\Gamma_\infty} \sim 1 \tag{4.12}$$

$$\frac{L}{U} C_0^2 = -\frac{1}{2 \cdot k_{ads}} \ln\left(1 - \frac{\Gamma}{\Gamma_{eq}^{CMC}}\right) \tag{4.13}$$

$$\frac{\Gamma}{\Gamma_{eq}^{CMC}} = 1 - e^{-\frac{2 \cdot k_{ads} L C_0^2}{U}} \tag{D.22}$$

The rate constants from the pH data k_{ads} (Fig. 4.10) and from the coalescence experiments $k = \left(LC^2/U\right)^{-1}$ (Fig. 4.11), respectively, are:

$$k = 909 \frac{m^6}{s\ mol^2} \tag{D.23}$$

$$k_{ads} = 1400 \frac{m^6}{s\ mol^2} \tag{D.24}$$

Relating the adsorption constant from the transfer of protons k_{ads} to the coalescence experiments (Eq. D.22), the interface is stable against coalescence above a coverage of:

$$\frac{\Gamma}{\Gamma_\infty} = 95.4\% \tag{D.25}$$

Additionally, I assume a certain coverage and calculate the apparent adsorption constant of the transition from stable to unstable emulsions $k = (LC^2/U)^{-1}$ (Table D.1, Fig. 4.11).

Table D.1: Calculation of the adsorption constant, k, for different coverages, Γ/Γ_∞, of the interface using Equation D.22.

Γ/Γ_∞ in %	80.0	85.0	90.0	95.0	98.0	98.5	99.0	99.7
k in $s^{-1}m^6mol^{-2}$	1740	1476	1216	935	716	667	608	482
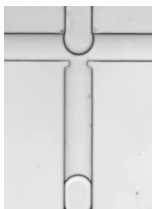
Appendix E

Analysis of the synthesis using NMR spectroscopy

E.1 Materials and methods

I used NMR spectroscopy for the analysis of the synthesised surfactants. I prepared a solution of 1:1 (w/w) of synthesised surfactant or reactant in hexafluorobenzene (99% Alfa Aesar). The locking was done using Benzene-d_6 (99.98%, euriso-top) as internal reference (within a thin tube inside the NMR tube). 1D ^{19}F-NMR experiments were recorded at 40°C on a Jeol Resonance 400 MHz spectrometer using 130k points and 6500 scans and a spectral width of 37899 Hz.[1]

E.2 Results

In this chapter, I present the NMR spectra of the reactant (Fig. E.2) and the products (Fig. E.3, E.4) and all fluorinated solvents (Fig. E.5-E.7) used for the synthesis. The signals between -70 and -150 p.p.m. are as follows.

The sum of the integrals for the reactant KrytoxFSH, the product P_5 and the control C_1 is set to 143 as this is the number of fluorine atoms present in the molecule (Sec. 4.3.1).

---

[1]These measurements were performed by Stéphanie Exiga at the Centre de Recherche Paul Pascal.
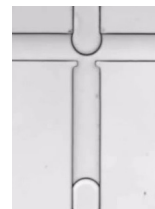
For the solvents, the sum of the integrals is arbitrary because only the chemical shifts in the region relevant for the reactant, control and product is considered. The signals * are discussed later on.
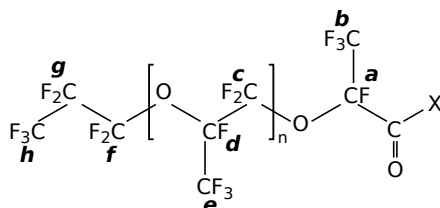

Figure E.1: The structure of the different products with different X. KrytoxFSH: X = OH, C_1: X = salt, PFPE-PEG(-PFPE): X = PEG.

^{19}F-NMR of **KrytoxFSH** (Fig. E.2) (400MHz, benzene-d_6): δ −80.5 - −83.5 (m, 115.8F, 'c,e,h'), −83.82 - −83.98 (m, 1.8, 'f'); −84.85 - −85.04 (m, 1.5F, 'b'); −131.55 - −131.68 (m, 0.9F, 'g'); −133.10 - −133.57 (s, 0.4F, 'a'); −145.25 - −146.75 (m, 22.5, 'd'). For the KrytoxFSH (Fig. E.1) the peaks were assigned previously [184,199,200]. The impurity of the solvent C_6F_6 is visible in the signal with the center at −142.77 (see Spectrum of C_6F_6: Fig. E.5).

^{19}F-NMR of sample **P_5** (**PFPE-PEG-PFPE**) (400MHz, benzene-d_6): δ −80.47 - −82.41 (m, 114.7F, 'c,e,h'); −83.70 - −83.93 (m, 2.8F, 'f'); −84.65 - −85.05 (m, 2.0F, 'b'); −131.52 - −131.67 (m, 1.3F, 'g'); −133.17 - −134.12 (m, 0.6, 'a'), −145.23 - −146.25 (m, 21.7F, 'd') are assigned in Fig. E.3. The peaks were assigned previously [143,184,199,200]. The signals from impurities of the solvent are as follows (see Spectrum of C_6F_6: Fig. E.5): −110.55 of C_6F_6, −119.68 *, −123.27 of FC3283, −128.26 of Novec7100*, −142.21 of C_6F_6.

^{19}F-NMR of Sample **C_1** (400MHz, benzene-d_6, Fig. E.4): δ −80.47 - −81.47 (m, 115.6F, 'c,e,h'); −83.81 - −83.97 (m, 2.1F, 'f'); −84.27 - −84.26 (m, 0.8F, 'b' of PEG-PFPE *); −86.83 - −87.00 (m, 1.2F, 'b' of salt *); −124.95 - −126.05 (m, 0.25, 'a' of salt *); −131.54 - −131.67 (m, 1.2F, 'g'); −145.22 - −146.30 (m, 21.8F, 'd'). The signals are assigned as previously [143,155,184,199,200]. The other signals are due to impurities in the solvent (see Spectrum of C_6F_6: Fig. E.5): −110.53, −142.3 from C_6F_6; −147.78 - −148.13 *.
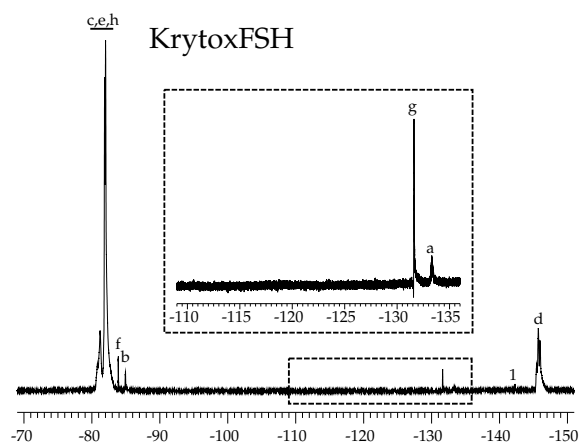
Figure E.2: ^{19}F-NMR spectrum of KrytoxFSH (Fig. E.1, X=OH) with the assigned peaks[184,199,200]. The number in the spectrum relates to the solvent.
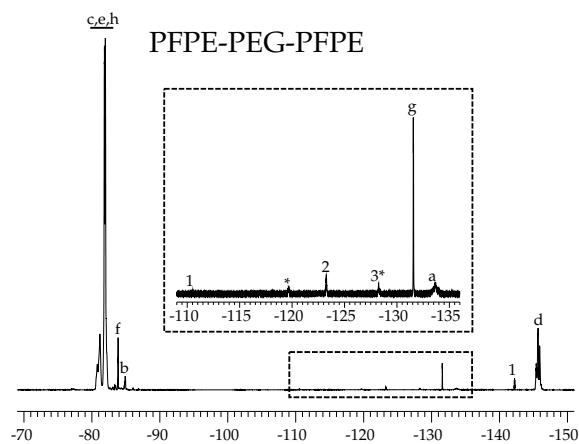
Figure E.3: ^{19}F-NMR spectrum of PFPE-PEG-PFPE (Fig. E.1, X=PEG(-PFPE)) with the assigned peaks[143,184,199,200]. The number in the spectrum relates to the solvent.
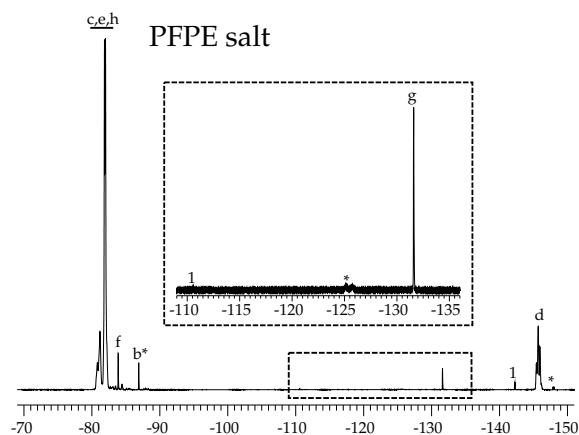
Figure E.4: ^{19}F-NMR spectrum of the PFPE salt (Fig. E.1, X=salt) with the assigned peaks[143,155,184,199,200]. The number in the spectrum relates to the solvent.

133
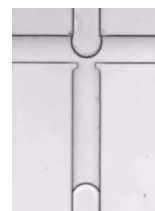
The solvents, I use for the synthesis as well as the impurities in the solvent used for the NMR spectroscopy show some peaks in the above named region as well.

^{19}F-NMR of $\mathbf{C_6F_6}$ (solvent #1, 400MHz, benzene-d$_6$, Fig. E.5): δ −110.52 - −110.64 (s, 1F); −135.53 - −135.56 (m, 1.7F); −142.12 - −142.39 (s, 29.4F).

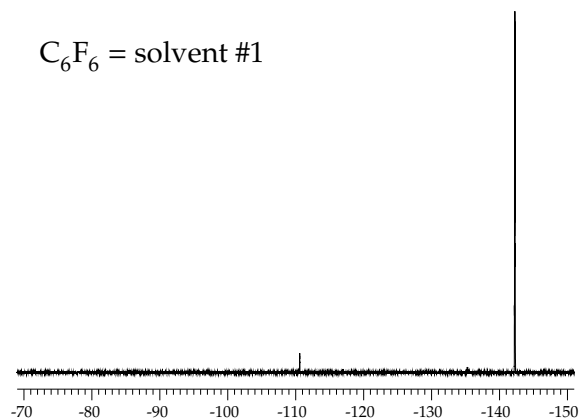**Figure E.5:** ^{19}F-NMR spectrum of C$_6$F$_6$ in the region used for the other spectra.

^{19}F-NMR of $\mathbf{FC3283}$ (solvent #2, 400MHz, benzene-d$_6$, Fig. E.6): −82.97 - −84.78 (m, 44.7F); −85.42 - −86.70 (m, 27.8F); −88.42 - −89.08 (m, 1.0F); −122.00 - −122.34 (m, 0.9F);−122.70 - −123.85 (m, 27.2F); −128.13 - −128.53 (m, 1.1F).
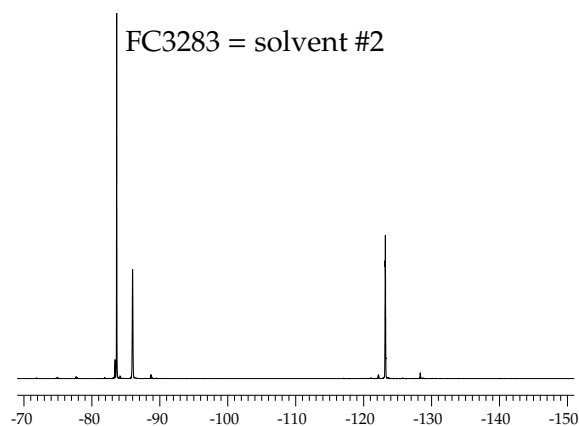

Figure E.6: ^{19}F-NMR spectrum of FC3283 in the region used for the other spectra.

^{19}F-NMR of $\mathbf{Novec7100}$ (solvent #3, 400MHz, benzene-d$_6$, Fig. E.7): −74.47 - −75.75 (m, 46.4F); −82.84 - −83.48 (m, 15.4F); −83.48 - −84.38 (m, 15.5F); −90.37 - −90.95 (m, 10.21); −127.42 - −127.95 (m, 9.9F); −127.95 - −128.26 (m, 9.8F).
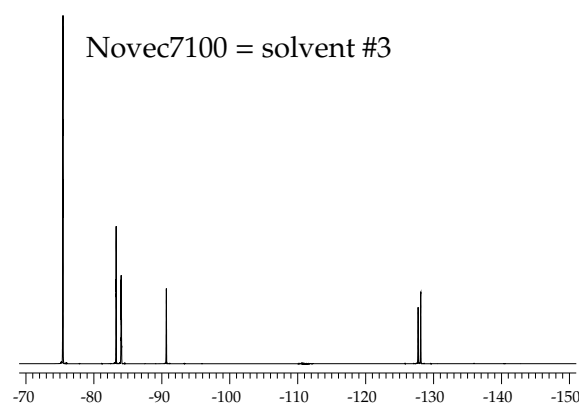
Figure E.7: ^{19}F-NMR spectrum of Novec7100 in the region used for the other spectra.

E.3 Discussion

In general, my ^{19}F-NMR spectra show the peaks cited in the literature. I relate the signals of the carboxylic acid (KrytoxFSH) to the studes by Li *et al.*[200,201] as they analyse the ^{19}F-NMR spectra using a 2D NMR study of a model compound of Krytox which is much shorter (Fig. E.8(b)-(c)). Thus, in this study all peaks are well assigned which is not possible using classical NMR methods[200]. This study confirms the results of the work of Temtem *et al.*[199] (Fig. E.9(e)). Only the NMR signals of the fluorine atoms which are in close proximity to the functional group, which undergoes reaction, differ from molecule to molecule ('a,b', in Fig. E.1 to Fig. E.4). None of the other signals are influenced ('c-h' in Fig E.1 to Fig. E.4, Fig. E.8(c))[201]. Thus, the CF 'a' and the CF_3 'b' have to be considered for further analysis. Other work by Holtze *et al.*[143] and Scanga *et al.*[184] on the product PFPE-PEG-PFPE molecule (P_5) has been done assigning these two groups to signals in the same range (Fig. E.8(a), E.9(f)). The study by Guo *et al.*[202] agrees with the finding that the chemical shift from the acid to the amide changes only slightly (-3 p.p.m.) including experiments on perfluoroheptanoic acid and perfluoroheptanoyl N-polyoxalate amide (Fig. E.9(a), (b)). They show that the salt (sodium perfluoroheptanoate) in relation to the acid does not influence the chemical shift either (-1 p.p.m.). More importantly, they show that an increase of the surfactant concentration in solution leads to merging of the relevant signals due to interactions and micellisation. The study on a similar molecule to the one I use in this study (linear perfluoropolyether chain) shows that the ionisation of the carboxylic acid group (to the salt) results in an only slightly higher (+2 p.p.m.) chemical shift (Fig. E.9(c), (d))[155]. Holtze *et al.* assign the signal of the chemical shift of the CF group in close proximity to the functional group ('a', fig E.1) of the PFPE-salt
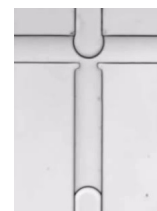
(C_1)[143] and the PFPE-PEG-PFPE using the integrated signals (Fig. E.9(f)). This results to an chemical shift which is a little bit higher (+6 p.p.m.).

The signals of my synthesised PFPE-PEG-PFPE surfactant are in good agreement with the above named literature values. I discuss the deviating signals in the following. The signal marked with 3* is likely due to the solvent, though it might be on overlay of more signals. The signal around −120 p.p.m. could not be assigned but is very low in intensity. Importantly, the signals for the PFPE salt are very similar to the PFPE-PEG-PFPE, apart from the signal 'a' and 'b'. In the literature, the signal 'b' was not shown to be shifted in contrast to the signal 'a' which is likely to be shifted to around −125 p.p.m. (Fig. E.9(f))[143]. Besides the difficulty, that the chemical shifts are very similar for the different species, I am characterising a polymer. This makes the quantitative analysis challenging because the integrals of the relevant signals are very low in intensity. Therefore, I do not use these NMR experiments for the quantification of impurities in the synthesised products, but rather IR spectroscopy and partitioning experiments (Sec. 4.3.2, 4.3.3).
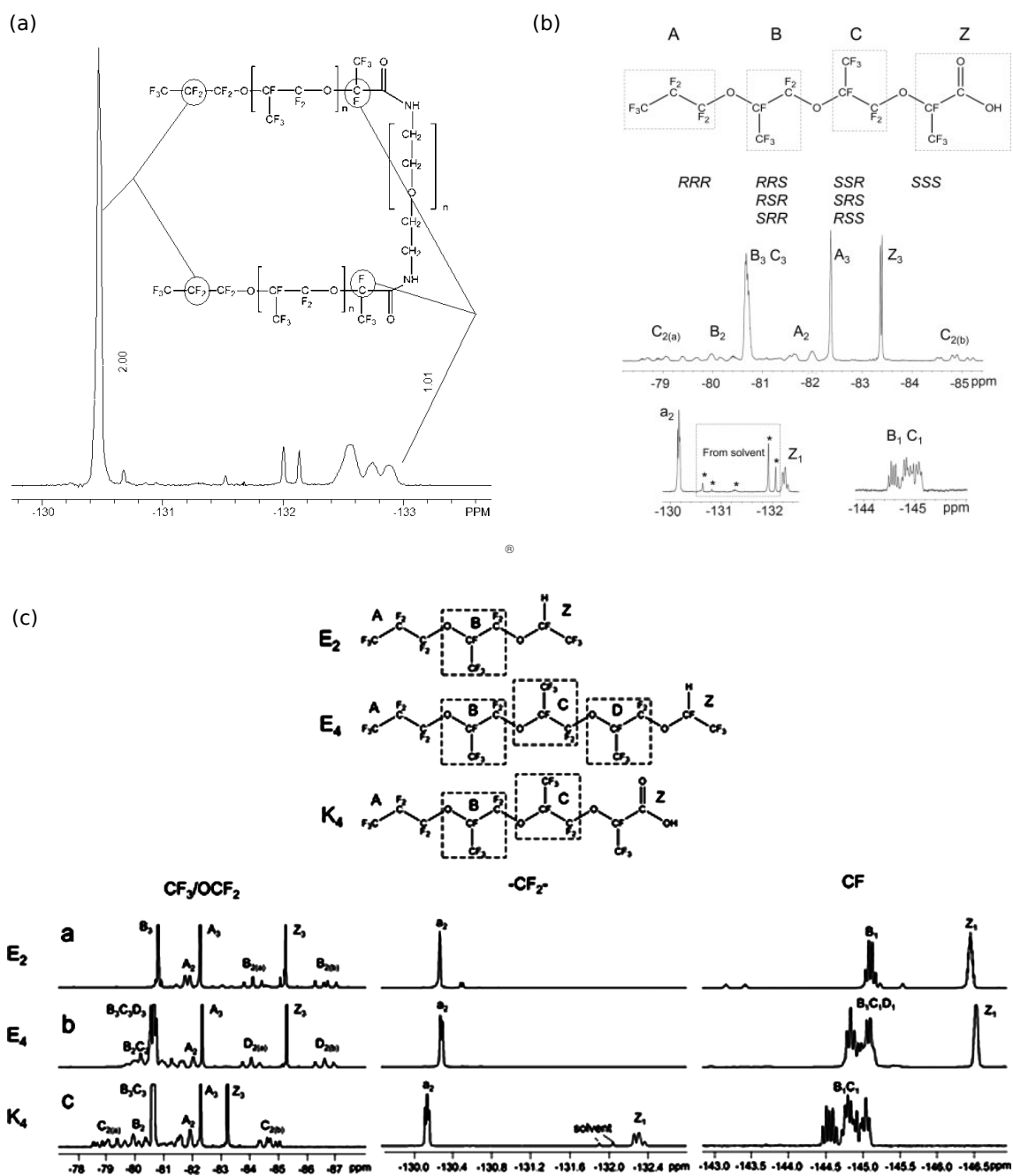
(a)

(b)

(c)

Figure E.8: ^{19}F-NMR spectra previously published with assigned peaks. (a) PFPE-PEG-PFPE surfactant [184]. (Reprinted with permissions from R. Scanga, R. Nassar, B. Miller, H. Gang, L. Xinyu, J. B. Hutchison, Fluorinated Amphiphilic Block Copolymers to Stabilize Water-in-Fluorocarbon Emulsions, *Polymer Preprints* **2009**, *50*, 148-149 [184]. Copyright (2009), the authors.) (b) The compound shown in the figure has two main-chain repeat units (B, C shown by the rectangles), which are similar to those in Krytox. The number indicates the amount of F-atoms in the group. In the A-region, there are two CF_2 groups. The one directly connected to the oxygen is called A_2 and the second one is a_2 [200]. (Reprinted with permissions from X. Li, E. F. McCord, S. Baiagern, P. Fox, J. L. Howell, S. K. Sahoo, P. L. Rinaldi, *Magnetic Resonance in Chemistry* **2011**, *49*, 413-24. Copyright (2011) John Wiley & Sons, Ltd. . [200]) (c) Assignments (compare to (b)) of the backbone of pure E_2, E_4 and 80 mg/ml of K_4 in hexafluorobenzene [201]. (Reprinted with permissions from X. Li, E. F. McCord, P. A. Fox, J. L. Howell, P. L. Rinaldi, *International Journal of Polymer Analysis and Characterization* **2012**, *17*, 161-188. Copyright (2012) Taylor & Francis. [201])
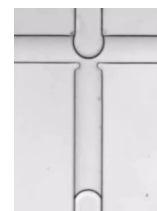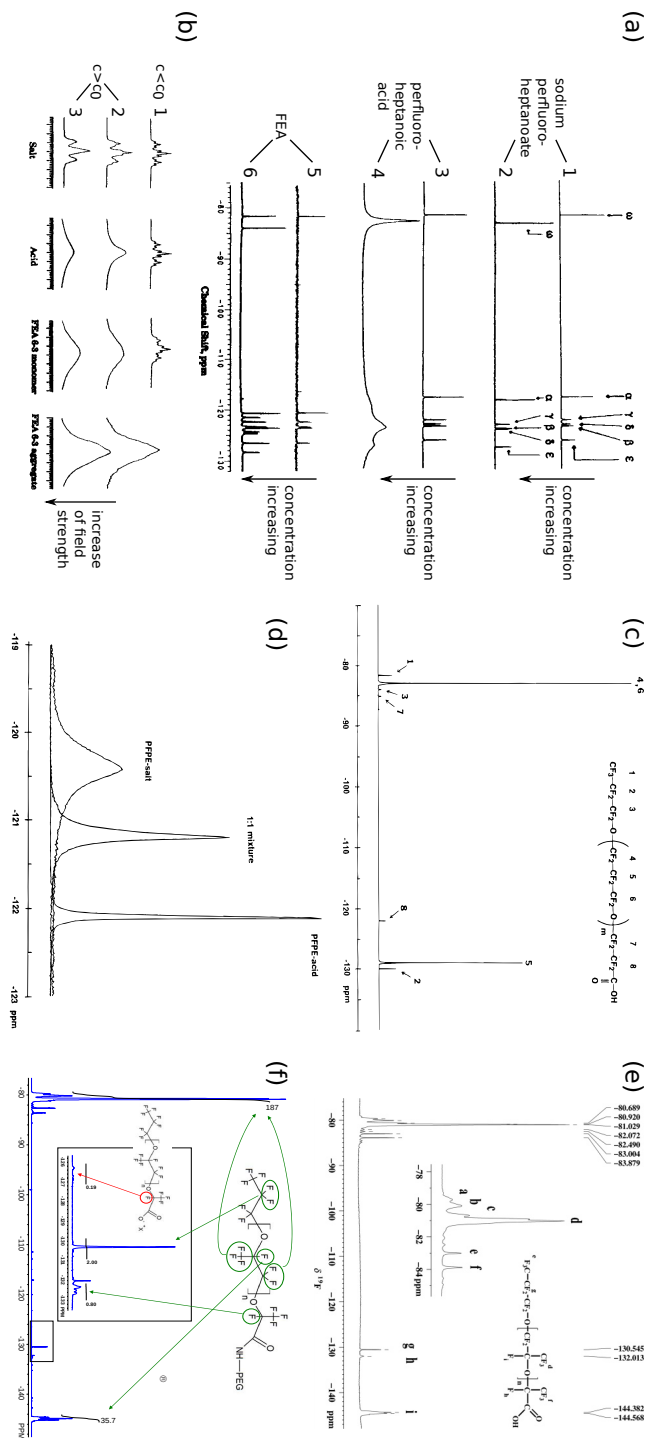
Figure E.9: ^{19}F-NMR spectra previously published with assigned peaks. (a) (1) 30 mM and (2) 180 mM sodium perfluoroheptanoate at 298 K, (3) 15 mM and (4) 60 mM perfluoroheptanoic acid at 298 K, (5) 0.4 mM and (6) 2.0 mM Perfluoroheptanoyl N-polyoxylated amides (FEA,CF$_3$(CF$_2$)$_5$C(O)NH(CH$_2$CH$_2$O)$_3$H) at 323 K [202] (b) Signals of FEA, perfluoroheptanoic acid and its sodium salt (1) below c_0 (aggregates form at a concentration of c_0) at 284 MHz, (2) above c_0 at 284 MHz, and (3) above c_0 at 470 MHz. The width of each plot is 80 Hz, except for the acid above c_0, which has a plotting width of 800 Hz.[202] . ((a)–(b) Reprinted with permission from W. Guo, T. A. Brown, B. M. Fung, *The Journal of Physical Chemistry* **1991**, *95*, 1829-1836. Copyright (1991) American Chemical Society.[202]) (c) The chemical shifts of the given molecule are measured in reference to CFCl$_3$.[155] (d) Peak 8 of (c), shown in an expanded scale for the acid, its sodium salt and the 1:1 mixture.[155] . ((c)–(d) Reprinted with permission from V. Doan, R. Köppe, P. H. Kasai, *Journal of American Chemical Society* **1997**, *119*, 9810-9815. Copyright (1997) American Chemical Society.[155]) (e) Krytox in supercritical CO$_2$ measured at high pressure and a temperature of 334 K (Reprinted with permission from M. Temtem, T. Casimiro, A. G. Santos, A. L. Macedo, E. J. Cabrita, A. Aguiar-Ricardo, *Journal of Physical Chemistry B* **2007**, *111*, 1318-1326. Copyright (2007) American Chemical Society.[199]) (f) Spectra of the Krytox carboxylate and the synthesised PFPE-PEG-PFPE surfactant. They compare the peaks in the region around −132 to −133 p.p.m. of the PFPE-PEG-PFPE surfactant and the peaks in the region around −126 to −127 p.p.m. of the molecule with the acid chloride end group, concluding a 80% completeness of the synthesis. (Reproduced from C. Holtze, A. C. Rowat, J. J. Agresti, J. B. Hutchison, F. E. Angilè, C. H. J. Schmitz, S. Köster, H. Duan, K. J. Humphry, R. A. Scanga, J. S. Johnson, D. Pisignano, D. A. Weitz, *Lab on a Chip* **2008**, *8*, 1632-1639 with permission of The Royal Society of Chemistry.[143])

138

Bibliography

[1] *Interfacial Science: An Introduction*, (Eds.: G. T. Barnes, I. R. Gentle), Oxford University Press, New York, 2nd ed., **2011**.

[2] *Surfactants and Interfacial Phenomena*, (Ed.: M. J. Rosen), John Wiley & Sons, Inc., Hoboken, New Jersey, 3rd ed., **2004**.

[3] D. Weaire, S. Hutzler, *The Physics of Foams*, Oxford University Press, New York, **1999**.

[4] J. Bibette, F. Leal Calderon, P. Poulin, *Reports on Progress in Physics* **1999**, *62*, 969–1033.

[5] N. Bremond, J. Bibette, *Soft Matter* **2012**, *8*, 10549–10559.

[6] H.-J. Butt, K. Graf, M. Kappl, *Physics and Chemistry of Interfaces*, Wiley-VCH Verlag GmbH & Co. KGaA, Weinheim, **2003**, pp. 118–144.

[7] J.-C. Baret, *Lab on a Chip* **2012**, *12*, 422–33.

[8] P. Gruner, B. Riechers, L. A. Chacòn Orellana, Q. Brosseau, F. Maes, T. Beneyton, D. Pekin, J.-C. Baret, *Current Opinion in Colloid & Interface Science* **2015**, *20*, 183–191.

[9] S. E. Maurer, P.-A. Monnard, *Entropy* **2011**, *13*, 466–484.

[10] E. V. Koonin, *Antonie van Leeuwenhoek* **2014**, *106*, 27–41.

[11] A. B. Theberge, F. Courtois, Y. Schaerli, M. Fischlechner, C. Abell, F. Hollfelder, W. T. S. Huck, *Angewandte Chemie - International Edition* **2010**, *49*, 5846–5868.

[12] O. J. Miller, A. El Harrak, T. Mangeat, J.-C. Baret, L. Frenz, B. El Debs, E. Mayot, M. L. Samuels, E. K. Rooney, P. Dieu, M. Galvan, D. R. Link, A. D. Griffiths, *Proceedings of the National Academy of Sciences* **2012**, *109*, 378–383.

[13] J.-C. Baret, Y. Beck, I. Billas-Massobrio, D. Moras, A. D. Griffiths, *Chemistry & Biology* **2010**, *17*, 528–536.

[14] D. Pekin, Y. Skhiri, J.-C. Baret, D. Le Corre, L. Mazutis, C. B. Salem, F. Millot, A. El Harrak, J. B. Hutchison, J. W. Larson, D. R. Link, P. Laurent-Puig, A. D. Griffiths, V. Taly, *Lab on a Chip* **2011**, *11*, 2156–66.

[15] E. Brouzes, M. Medkova, N. Savenelli, D. Marran, M. Twardowski, J. B. Hutchison, J. M. Rothberg, D. R. Link, N. Perrimon, M. L. Samuels, *Proceedings of the National Academy of Sciences* **2009**, *106*, 14195–14200.
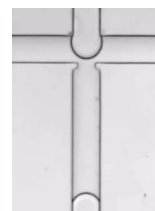
[16] R. Seemann, M. Brinkmann, T. Pfohl, S. Herminghaus, *Reports on Progress in Physics* **2012**, *75*, 016601.

[17] B. T. Kelly, J.-C. Baret, V. Taly, A. D. Griffiths, *Chemical Communications* **2007**, 1773–1788.

[18] M. T. Guo, A. Rotem, J. A. Heyman, D. A. Weitz, *Lab on a Chip* **2012**, *12*, 2146–2155.

[19] H. N. Joensson, H. Andersson Svahn, *Angewandte Chemie - International Edition* **2012**, *51*, 12176–12192.

[20] J. J. Agresti, E. Antipov, A. R. Abate, K. Ahn, A. C. Rowat, J.-C. Baret, M. Marquez, A. M. Klibanov, A. D. Griffiths, D. A. Weitz, *Proceedings of the National Academy of Sciences* **2010**, *107*, 4004–4009.

[21] A. Fallah-Araghi, K. Meguellati, J.-C. Baret, A. El Harrak, T. Mangeat, M. Karplus, S. Ladame, C. M. Marques, A. D. Griffiths, *Physical Review Letters* **2014**, *112*, 028301.

[22] B. Vazquez, N. Qureshi, L. Oropeza-Ramos, L. F. Olguin, *Lab on a Chip* **2014**, *14*, 3550–3555.

[23] I. Polenz, Q. Brosseau, J.-C. Baret, *Soft matter* **2015**, *11*, 2916–2923.

[24] D. J. McClements, *Soft Matter* **2012**, *8*, 1719–1729.

[25] G. Woronoff, A. El Harrak, E. Mayot, O. Schicke, O. J. Miller, P. Soumillion, A. D. Griffiths, M. Ryckelynck, *Analytical Chemistry* **2011**, *83*, 2852–2857.

[26] R. Miller, G. Kretzschmar, *Advances in Colloid and Interface Science* **1991**, *37*, 97–121.

[27] B. Dai, L. G. Leal, *Physics of Fluids* **2008**, *20*, 040802.

[28] Y. Skhiri, P. Gruner, B. Semin, Q. Brosseau, D. Pekin, L. Mazutis, V. Goust, F. Kleinschmidt, A. El Harrak, J. B. Hutchison, E. Mayot, J.-F. Bartolo, A. D. Griffiths, V. Taly, J.-C. Baret, *Soft Matter* **2012**, *8*, 10618.

[29] P. Taylor, *Advances in Colloid and Interface Science* **1998**, *75*, 107–163.

[30] Z. Izri, M. N. van der Linden, S. Michelin, O. Dauchot, *Physical Review Letters* **2014**, *113*, 248302.

[31] S. Thutupalli, R. Seemann, S. Herminghaus, *New Journal of Physics* **2011**, *13*, 073021.

[32] M. M. Hanczyc, *Philosophical Transactions of the Royal Society B: Biological Sciences* **2011**, *366*, 2885–2893.

[33] N. J. Alvarez, D. R. Vogus, L. M. Walker, S. L. Anna, *Journal of Colloid and Interface Science* **2012**, *372*, 183–91.

[34] H. Diamant, D. Andelman, *Journal of Physical Chemistry* **1996**, *100*, 13732–13742.

[35] R. P. Borwankar, D. T. Wasan, *Chemical Engineering Science* **1988**, *43*, 1323–1337.

[36] V. Kalinin, C. Radke, *Colloids and Surfaces A: Physicochemical and Engineering Aspects* **1996**, *114*, 337–350.

[37] G. Kretzschmar, R. Miller, *Advances in Colloid and Interface Science* **1991**, *36*, 65–124.

[38] S. N. Moorkanikkara, D. Blankschtein, *Langmuir* **2009**, *25*, 6191–6202.

[39] J. Eastoe, J. S. Dalton, *Advances in Colloid and Interface Science* **2000**, *85*, 103–144.

[40] Y. He, P. Yazhgur, A. Salonen, D. Langevin, *Advances in Colloid and Interface Science* **2015**, *222*, 377–384.

[41] F. Jin, R. Balasubramaniam, K. J. Stebe, *The Journal of Adhesion* **2004**, *80*, 773–796.

[42] D. J. Holt, R. J. Payne, C. Abell, *Journal of Fluorine Chemistry* **2010**, *131*, 398–407.

[43] B. Riechers, F. Maes, E. Akoury, B. Semin, P. Gruner, J.-C. Baret, *in preparation* **2015**.

[44] A. V. Makievski, G. Loglio, J. Krägel, R. Miller, V. B. Fainerman, A. W. Neumann, *Journal of Physical Chemistry B* **1999**, *103*, 9557–9561.

[45] P. G. de Gennes, *Advances in Colloid and Interface Science* **1987**, *27*, 189–209.

[46] I. Platzman, J.-W. Janiesch, J. P. Spatz, *Journal of the American Chemical Society* **2013**, *135*, 3339–3342.

[47] M. Pan, L. Rosenfeld, M. Kim, M. Xu, E. Lin, R. Derda, S. K. Y. Tang, *Applied Materials and Interfaces* **2014**, *6*, 21446–21453.

[48] R. Aveyard, B. P. Binks, J. H. Clint, *Advances in Colloid and Interface Science* **2003**, *100-102*, 503–546.

[49] P. Lo Nostro, *Advances in Colloid and Interface Science* **1995**, *56*, 245–287.

[50] R. L. Scott, *Journal of the American Chemical Society* **1948**, *70*, 4090–4093.

[51] A. R. Thiam, N. Bremond, J. Bibette, *Langmuir* **2012**, *28*, 6291–6298.

[52] H. N. Joensson, M. Uhlén, H. A. Svahn, *Lab on a Chip* **2011**, *11*, 1305–1310.

[53] D. J. McClements, S. R. Dungan, *The Journal of Physical Chemistry* **1993**, *97*, 7304–7308.

[54] B. J. Zwolinski, H. Eyring, C. E. Reese, *The Journal of Physical and Colloid Chemistry* **1949**, *53*, 1426–1453.

[55] F. Courtois, L. F. Olguin, G. Whyte, A. B. Theberge, W. T. S. Huck, F. Hollfelder, C. Abell, *Analytical Chemistry* **2009**, *81*, 3008–3016.

[56] N. Wu, F. Courtois, Y. Zhu, J. Oakeshott, C. Easton, C. Abell, *Electrophoresis* **2010**, *31*, 3121–3128.

[57] *Physical Chemistry*, (Eds.: P. Atkins, J. de Paula), Oxford University Press, 9th ed., **2010**.

[58] A. C. Mitropoulos, *Journal of Engineering Science and Technology Review* **2008**, *1*, 1–3.

[59] E. Ruckenstein, R. Nagarajan, *The Journal of Physical Chemistry* **1975**, *79*, 2622–2626.

[60] M. Zulauf, U. Fürstenberger, M. Grabo, P. Jäggi, M. Regenass, J. P. Rosenbusch, *Methods in Enzymology* **1989**, *172*, 528–538.

[61] P. Gruner, B. Riechers, B. Semin, J. Lim, A. Johnston, K. Short, J.-C. Baret, *Nature Communications* **2015**, in press.

[62] E. Ruckenstein, R. Nagarajan, *The Journal of Physical Chemistry* **1980**, *84*, 1349–1358.

[63] G. N. Smith, P. Brown, S. E. Rogers, J. Eastoe, *Langmuir* **2013**, *29*, 3252–3258.
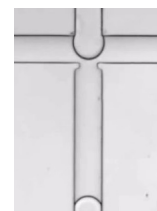
[64] J. C. Ravey, M. J. Stébé, *Progress in Colloid and Polymer Science* **1990**, *82*, 218–228.

[65] M. Monduzzi, *Current Opinion in Colloid & Interface Science* **1998**, *3*, 467–477.

[66] M. Karvar, F. Strubbe, F. Beunis, R. Kemp, N. Smith, M. Goulding, K. Neyts, *Langmuir* **2014**, *30*, 12138–12143.

[67] P. L. Du Nouy, *Journal of General Physiology* **1919**, *1*, 521–524.

[68] P. L. Du Nouy, *The Journal of General Physiology* **1925**, *7*, 625–631.

[69] W. D. Harkins, H. F. Jordan, *Journal of the American Chemical Society* **1930**, *52*, 1751–1772.

[70] C. Huh, S. G. Mason, *Colloid and Polymer Science* **1975**, *253*, 566–580.

[71] *Handbook of Applied Surface and Colloid Chemistry*, *Vol. 2*, (Eds.: K. Holmberg, D. O. Shah, M. J. Schwuger), John Wiley & Sons, LTD, Weinheim, **2002**.

[72] F. R. S. Lord Rayleigh, *Philosophical Magazine and Journal of Science* **1899**, *48*, 321–337.

[73] F. Kohlrausch, *Annalen der Physik* **1906**, *325*, 798–806.

[74] W. D. Harkins, F. E. Brown, *Journal of the American Chemical Society* **1919**, *41*, 499–524.

[75] *Progress in Colloid and Interface Scienc, Vol. 2, Bubble and Drop Interfaces*, (Eds.: R. Miller, L. Liggieri), Koninklijke Brill NV, Leiden, **2011**.

[76] C. E. Stauffer, *Journal of Physical Chemistry* **1965**, *69*, 1933–1938.

[77] A. F. H. Ward, L. Tordai, *The Journal of Chemical Physics* **1946**, *14*, 453.

[78] I. Langmuir, *Proceedings of the National Academy of Sciences* **1917**, *3*, 251–257.

[79] D. Colegate, C. Bain, *Physical Review Letters* **2005**, *95*, 198302.

[80] M. D. Reichert, L. M. Walker, *Langmuir* **2013**, *29*, 1857–1867.

[81] J. K. Ferri, S. Y. Lin, K. J. Stebe, *Journal of Colloid and Interface Science* **2001**, *241*, 154–168.

[82] H. Diamant, G. Ariel, D. Andelman, *Colloids and Surfaces A: Physicochemical and Engineering Aspects* **2001**, *183-185*, 259–276.

[83] A. Bonfillon, F. Sicoli, D. Langevin, *Journal of Colloid and Interface Science* **1994**, *168*, 497–504.

[84] I. Langmuir, *Journal of American Chemical Society* **1918**, *40*, 1361–1403.

[85] A. Bricard, J.-B. Caussin, N. Desreumaux, O. Dauchot, D. Bartolo, *Nature* **2013**, *503*, 95–98.

[86] K. Peddireddy, P. Kumar, S. Thutupalli, S. Herminghaus, C. Bahr, *Langmuir* **2012**, *28*, 12426–12431.

[87] T. Sanchez, D. T. N. Chen, S. J. DeCamp, M. Heymann, Z. Dogic, *Nature* **2012**, *491*, 431–434.

[88] T. Ban, T. Yamagami, H. Nakata, Y. Okano, *Langmuir* **2013**, *29*, 2554–2561.

[89] L. E. Scriven, C. V. Sternling, *Nature* **1960**, *187*, 186–188.

[90] M. Schmitt, H. Stark, *Europhysics Letters* **2013**, *101*, 44008.

[91] A. Farutin, S. Rafaï, D. K. Dysthe, A. Duperray, P. Peyla, C. Misbah, *Physical Review Letters* **2013**, *111*, 228102.

[92] H.-S. Kuan, R. Blackwell, L. E. Hough, M. A. Glaser, M. D. Betterton, *arXiv [cond-mat.soft]* **2014**.

[93] G. M. Whitesides, *Nature* **2006**, *442*, 368–373.

[94] J.-u. Shim, R. T. Ranasinghe, C. A. Smith, S. M. Ibrahim, F. Hollfelder, W. T. S. Huck, D. Klenerman, C. Abell, *ACS Nano* **2013**, *7*, 5955–5964.

[95] G. F. Christopher, S. L. Anna, *Journal of Physics D: Applied Physics* **2007**, *40*, R319–R336.

[96] C. N. Baroud, F. Gallaire, R. Dangla, *Lab on a Chip* **2010**, *10*, 2032–2045.

[97] C. D. Costin, R. E. Synovec, *Talanta* **2002**, *58*, 551–560.

[98] T. Thorsen, R. W. Roberts, F. H. Arnold, S. R. Quake, *Physical Review Letters* **2001**, *86*, 4163–4166.

[99] P. Garstecki, M. J. Fuerstman, H. A. Stone, G. M. Whitesides, *Lab on a Chip* **2006**, *6*, 437–446.

[100] V. Mengeaud, J. Josserand, H. H. Girault, *Analytical Chemistry* **2002**, *74*, 4279–4286.

[101] A. J. DeMello, *Nature* **2006**, *442*, 394–402.

[102] R. Dangla, E. Fradet, Y. Lopez, C. N. Baroud, *Journal of Physics D: Applied Physics* **2013**, *46*, 114003.

[103] S. L. Anna, N. Bontoux, H. A. Stone, *Applied Physics Letters* **2003**, *82*, 364–366.

[104] M. R. Bringer, C. J. Gerdts, H. Song, J. D. Tice, R. F. Ismagilov, *Philosophical Transactions. Series A: Mathematical Physical and Engineering Sciences* **2004**, *362*, 1087–1104.

[105] H. A. Stone, *Annual Review of Fluis Mechanics* **1994**, *26*, 65–102.

[106] L. Rosenfeld, L. Fan, Y. Chen, R. Swoboda, S. K. Y. Tang, *Soft Matter* **2014**, *10*, 421–430.

[107] P. Garstecki, H. A. Stone, G. M. Whitesides, *Physical Review Letters* **2005**, *94*, 164501.

[108] S. L. Anna, H. C. Mayer, *Physics of Fluids* **2006**, *18*, 121512.

[109] R. A. De Bruijn, *Chemical Engineering Science* **1993**, *48*, 277–284.

[110] J.-C. Baret, F. Kleinschmidt, A. El Harrak, A. D. Griffiths, *Langmuir* **2009**, *25*, 6088–6093.

[111] A. Günther, M. Jhunjhunwala, M. Thalmann, M. A. Schmidt, K. F. Jensen, *Langmuir* **2005**, *21*, 1547–1555.

[112] A. Günther, K. F. Jensen, *Lab on a Chip* **2006**, *6*, 1487–1503.

[113] Q. Brosseau, J. Vrignon, J.-C. Baret, *Soft Matter* **2014**, *10*, 3066–3076.

[114] J. Atencia, D. J. Beebe, *Nature* **2005**, *437*, 648–655.
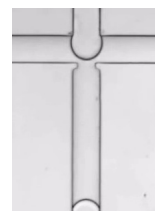
[115] L. Frenz, A. El Harrak, M. Pauly, S. Bégin-Colin, A. D. Griffiths, J. C. Baret, *Angewandte Chemie - International Edition* **2008**, *47*, 6817–6820.

[116] C. Priest, S. Herminghaus, R. Seemann, *Applied Physics Letters* **2006**, *89*, 134101.

[117] L. Mazutis, J. Gilbert, W. L. Ung, D. A. Weitz, A. D. Griffiths, J. A. Heyman, *Nature Protocols* **2013**, *8*, 870–891.

[118] K. Ahn, C. Kerbage, T. P. Hunt, R. M. Westervelt, D. R. Link, D. A. Weitz, *Applied Physics Letters* **2006**, *88*, 024104.

[119] J.-C. Baret, O. J. Miller, V. Taly, M. Ryckelynck, A. El-Harrak, L. Frenz, C. Rick, M. L. Samuels, J. B. Hutchison, J. J. Agresti, D. R. Link, D. A. Weitz, A. D. Griffiths, *Lab on a Chip* **2009**, *9*, 1850–1858.

[120] P. Abbyad, R. Dangla, A. Alexandrou, C. N. Baroud, *Lab on a Chip* **2011**, *11*, 813–821.

[121] E. Fradet, C. McDougall, P. Abbyad, R. Dangla, D. McGloin, C. N. Baroud, *Lab on a Chip* **2011**, *11*, 4228.

[122] R. Dangla, S. Lee, C. N. Baroud, *Physical Review Letters* **2011**, *107*, 124501.

[123] A. R. Abate, T. Hung, P. Mary, J. J. Agresti, D. A. Weitz, *Proceedings of the National Academy of Sciences* **2010**, *107*, 19163–19166.

[124] A. R. Thiam, N. Bremond, J. Bibette, *Physical Review Letters* **2009**, *102*, 188304.

[125] C. Priest, P. J. Gruner, E. J. Szili, S. A. Al-Bataineh, J. W. Bradley, J. Ralston, D. A. Steele, R. D. Short, *Lab on a Chip* **2011**, *11*, 541–544.

[126] A. C. Siegel, S. S. Shevkoplyas, D. B. Weibel, D. A. Bruzewicz, A. W. Martinez, G. M. Whitesides, *Angewandte Chemie - International Edition* **2006**, *45*, 6877–6882.

[127] C. Holtze, *Journal of Physics D: Applied Physics* **2013**, *46*, 114008.

[128] T. Nisisako, T. Torii, *Lab on a Chip* **2008**, *8*, 287–293.

[129] T. Nisisako, T. Ando, T. Hatsuzawa, *Lab on a Chip* **2012**, *12*, 3426–3435.

[130] M. B. Romanowsky, A. R. Abate, A. Rotem, C. Holtze, D. A. Weitz, *Lab on a Chip* **2012**, *12*, 802.

[131] G. P. Moss, P. A. S. Smith, D. Tavernier, *Pure & Applied Chemistry* **1995**, *67*, 1307–1375.

[132] W. J. Murphy, *Industrial & Engineering Chemistry* **1947**, 241–242.

[133] D. M. Lemal, *Journal of Organic Chemistry Persepective* **2004**, *69*, 1–11.

[134] D. O'Hagan, *Chemical Society Reviews* **2008**, *37*, 308–319.

[135] J.-M. Vincent, *Journal of Fluorine Chemistry* **2008**, *129*, 903–909.

[136] J. E. Brady, P. W. Carr, *Analytical Chemistry* **1982**, *54*, 1751–1757.

[137] M. A. Hamza, G. Serratrice, M. J. Stébé, J.-J. Delpuech, *Journal of the American Chemical Society* **1981**, *103*, 3733–3738.

[138] J. H. Simons, M. J. Linevsky, *Journal of American Chemical Society* **1952**, *74*, 4750–4751.

[139] Y. Bai, X. He, D. Liu, S. N. Patil, D. Bratton, A. Huebner, F. Hollfelder, C. Abell, W. T. S. Huck, *Lab on a Chip* **2010**, *10*, 1281–1285.

[140] J. Clausell-Tormos, D. Lieber, J.-C. Baret, A. El-Harrak, O. J. Miller, L. Frenz, J. Blouwolff, K. J. Humphry, S. Köster, H. Duan, C. Holtze, D. A. Weitz, A. D. Griffiths, C. A. Merten, *Chemistry & Biology* **2008**, *15*, 427–37.

[141] P. Abbyad, P.-L. Tharaux, J.-L. Martin, C. N. Baroud, A. Alexandrou, *Lab on a Chip* **2010**, *10*, 2505–2512.

[142] J. N. Lee, C. Park, G. M. Whitesides, *Analytical Chemistry* **2003**, *75*, 6544–6554.

[143] C. Holtze, A. C. Rowat, J. J. Agresti, J. B. Hutchison, F. E. Angilè, C. H. J. Schmitz, S. Köster, H. Duan, K. J. Humphry, R. A. Scanga, J. S. Johnson, D. Pisignano, D. A. Weitz, *Lab on a Chip* **2008**, *8*, 1632–1639.

[144] M. Trotta, M. R. Gasco, S. Morel, *Journal of Controlled Release* **1989**, *10*, 237–243.

[145] T. Koizumi, W. I. Higuchi, *Journal of Pharmaceutical Sciences* **1986**, *57*, 87–92.

[146] G. Calderó, M. J. García-Celma, C. Solans, M. Plaza, R. Pons, *Langmuir* **1997**, *13*, 385–390.

[147] G. Caldéro, M. J. García-Celma, C. Solans, M. J. Stébé, J. C. Ravey, S. Rocca, R. Pons, *Langmuir* **1998**, *14*, 1580–1585.

[148] G. Caldéro, M. J. García-Celma, C. Solans, R. Pons, *Langmuir* **2000**, *16*, 1668–1674.

[149] P. A. Sandoz, A. J. Chung, W. M. Weaver, D. Di Carlo, *Langmuir* **2014**, *30*, 6637–6643.

[150] V. G. Babak, M.-J. Stébé, N. Fa, *Mendeleev Communications* **2003**, *13*, 254–256.

[151] N. Fa, V. G. Babak, M.-J. Stébé, *Colloids and Surfaces A: Physicochemical and Engineering Aspects* **2004**, *243*, 117–125.

[152] G. Pozzi, M. Cavazzini, S. Quici, S. Fontana, *Tetrahedron Letters* **1997**, *38*, 7605–7608.

[153] B. Richter, A. L. Spek, G. van Koten, B.-J. Deelman, *Journal of the American Chemical Society* **2000**, *122*, 3945–3951.

[154] G. Pozzi, F. Cinato, F. Montanari, S. Quici, *Chemical Communications* **1998**, 877–878.

[155] V. Doan, R. Köppe, P. H. Kasai, *Journal of American Chemical Society* **1997**, *119*, 9810–9815.

[156] M. Remko, *Advances in Molecular Relaxation and Interaction Processes* **1979**, *15*, 193–206.

[157] P. Vishweshwar, A. Nangia, V. M. Lynch, *Journal of Organic Chemistry* **2002**, *67*, 556–565.

[158] K. L. O'Neal, S. Geib, S. G. Weber, *Analytical Chemistry* **2007**, *79*, 3117–3125.

[159] C. Palomo, J. M. Aizpurua, I. Loinaz, M. J. Fernandez-Berridi, L. Irusta, *Organic Letters* **2001**, *3*, 2361–2364.

[160] K. L. O'Neal, S. G. Weber, *Journal of Physical Chemistry B* **2009**, *113*, 149–158.
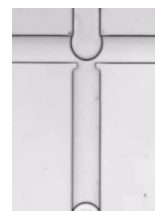
[161] C. J. Dejournette, J. Kim, H. Medlen, X. Li, L. J. Vincent, C. J. Easley, *Analytical Chemistry* **2013**, *85*, 10556–10564.

[162] W. L. Matochko, S. Ng, M. R. Jafari, J. Romaniuk, S. K. Y. Tang, R. Derda, *Methods* **2012**, *58*, 18–27.

[163] Y. Xia, G. M. Whitesides, *Angewandte Chemie - International Edition* **1998**, *37*, 550–575.

[164] J. C. McDonald, D. C. Duffy, J. R. Anderson, D. T. Chiu, H. Wu, O. J. A. Schueller, G. M. Whitesides, *Electrophoresis* **2000**, *21*, 27–40.

[165] D. Qin, Y. Xia, G. M. Whitesides, *Advanced Materials* **1996**, *8*, 917–919.

[166] B. Bohl, R. Steger, R. Zengerle, P. Koltay, *Journal of Micromechanics and Microengineering* **2005**, *15*, 1125–1130.

[167] Y. Xia, G. M. Whitesides, *Annual Review of Materials Science* **1998**, *28*, 153–184.

[168] P. Wägli, B. Y. Guélat, A. Homsy, N. F. de Rooij, *Proceeding of the 14th International Conference on Miniaturized Systems for Chemistry and Life Sciences (microTAS)* **2010**, 1937–1939.

[169] T. Lomas, S. Mongpraneet, A. Wisitsoraat, K. Jaruwongrungsee, A. Sappat, T. Maturos, F. Chevasuvit, A. Tuantranont, *6th International Conference on Electrical Engineering/Electronics Computer Telecommunications and Information Technology ECTI-CON* **2009**, *1*, 462–464.

[170] N.-T. Nguyen, S. Lassemono, F. A. Chollet, *Sensors and Actuators B: Chemical* **2006**, *117*, 431–436.

[171] J. H. Xu, S. W. Li, J. Tan, Y. J. Wang, G. S. Luo, *Langmuir* **2006**, *22*, 7943–7946.

[172] T. Nisisako, T. Torii, T. Higuchi, *Lab on a Chip* **2002**, *2*, 24–26.

[173] K.-S. Huang, T.-H. Lai, Y.-C. Lin, *Frontiers in Bioscience* **2007**, *12*, 3061–3067.

[174] B. Graß, A. Neyer, M. Jöhnck, D. Siepe, F. Eisenbeiß, G. Weber, R. Hergenröder, *Sensors and Actuators B: Chemical* **2001**, *72*, 249–258.

[175] N. Wu, Y. Zhu, S. Brown, J. Oakeshott, T. S. Peat, R. Surjadi, C. Easton, P. W. Leech, B. A. Sexton, *Lab on a Chip* **2009**, *9*, 3391–3398.

[176] Y. Molard, F. Dorson, K. A. Brylev, M. A. Shestopalov, Y. Le Gal, S. Cordier, Y. V. Mironov, N. Kitamura, C. Perrin, *Chemistry - A European Journal* **2010**, *16*, 5613–5619.

[177] A. Piruska, I. Nikcevic, S. H. Lee, C. Ahn, W. R. Heineman, P. A. Limbach, C. J. Seliskar, *Lab on a Chip* **2005**, *5*, 1348–1354.

[178] M. Heckele, W. K. Schomburg, *Journal of Micromechanics and Microengineering* **2003**, *14*, R1–R14.

[179] H. Bourbaba, C. Ben Achaiba, B. Mohamed, *Energy Procedia* **2013**, *36*, 231–237.

[180] J. M. Li, C. Liu, J. S. Liu, Z. Xu, L. D. Wang, *Journal of Materials Processing Technology* **2009**, *209*, 5487–5493.

[181] K.-S. Huang, T.-H. Lai, Y.-C. Lin, *Lab on a Chip* **2006**, *6*, 954–957.

[182] E. Sollier, C. Murray, P. Maoddi, D. Di Carlo, *Lab on a Chip* **2011**, *11*, 3752.

[183] J. Han, K. Burgess, *Chemical Reviews* **2010**, *110*, 2709–2728.

[184] R. Scanga, R. Nassar, B. Miller, H. Gang, L. Xinyu, J. B. Hutchison, *Polymer Preprints* **2009**, *50*, 148–149.

[185] P. Gruner, PhD thesis, Georg-August University, **2014**.

[186] J. G. Dick, *Analytical Chemistry*, McGraw-Hill Kogakusha, Tokyo, International Student Edition, **1973**.

[187] C. Bliefert, A. Linek, G. Morawietz, *pH-Wert-Berechnungen*, Verlag Chemie GmbH, Weinheim, **1978**.

[188] N. Agmon, *Chemical Physics Letters* **1995**, *244*, 456–462.

[189] R. Pan, J. Green, C. Maldarelli, *Journal of Colloid and Interface Science* **1998**, *205*, 213–230.

[190] *CRC Handbook of Chemistry and Physics, Internet Version 2005, <http://www.hbcpnetbase.com>*, (Ed.: D. R. Lide), CRC Press, Boca Raton, FL, **2005**.

[191] K. Nakanishi, *Infrared Absorption Spectroscopy - Practical*, Holden-Day, San Francisco, **1962**.

[192] F. Loeker, P. C. Marr, S. M. Howdle, *Colloids and Surfaces A: Physicochemical and Engineering Aspects* **2003**, *214*, 143–150.

[193] A. R. Abate, A. Poitzsch, Y. Hwang, J. Lee, J. Czerwinska, D. A. Weitz, *Physical Review E - Statistical Nonlinear and Soft Matter Physics* **2009**, *80*, 026310.

[194] B. Riechers, F. Wittbracht, A. Hütten, T. Koop, *Physical Chemistry Chemical Physics* **2013**, *15*, 5873–5887.

[195] J. Ernst, W. S. Sheldrick, J.-H. Fuhrhop, *Angewandte Chemie* **1979**, *88*, 851.

[196] N. Bremond, A. Thiam, J. Bibette, *Physical Review Letters* **2008**, *100*, 024501.

[197] H. Chen, Y. Zhao, J. Li, M. Guo, J. Wan, D. A. Weitz, H. A. Stone, *Lab on a Chip* **2011**, *11*, 2312–2315.

[198] S. Mashaghi, A. M. van Oijen, *Scientific Reports* **2015**, *5*, 11837.

[199] M. Temtem, T. Casimiro, A. G. Santos, A. L. Macedo, E. J. Cabrita, A. Aguiar-Ricardo, *Journal of Physical Chemistry B* **2007**, *111*, 1318–1326.

[200] X. Li, E. F. McCord, S. Baiagern, P. Fox, J. L. Howell, S. K. Sahoo, P. L. Rinaldi, *Magnetic Resonance in Chemistry* **2011**, *49*, 413–24.

[201] X. Li, E. F. McCord, P. A. Fox, J. L. Howell, P. L. Rinaldi, *International Journal of Polymer Analysis and Characterization* **2012**, *17*, 161–188.

[202] W. Guo, T. A. Brown, B. M. Fung, *The Journal of Physical Chemistry* **1991**, *95*, 1829–1836.
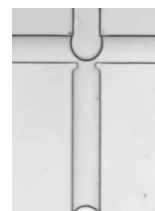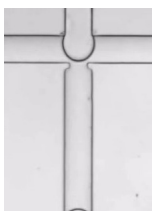
Acknowledgements

"Alone we can do so little. Together we can do so much." (by Helen Keller).

First of all, I want to thank my supervisor Jean-Christophe Baret for the great support throughout my thesis introducing me to an incredibly interesting topic in the scientific world. Thank you very much for being always available for discussions and for being a constant source of motivation. Vielen Dank für die schöne Zeit in Göttingen & merci beaucoup pour ces bons moments à Bordeaux.

I am grateful for the input and the helpful discussions with Sarah Köster and Oskar Hallatschek. Furthermore, I thank Sarah Köster and Jean-Christophe Baret to be the referees for my thesis and Thomas Burg, Philipp Vana, Manfred Konrad and Oskar Hallatschek to accept being members of the examination board for my thesis defence.

Additional thanks goes to the group members of the groups led by Jean-Christophe Baret at the Max Planck Institute of Dynamics & Self-Organization in Göttingen ('Droplets, Membranes and Interfaces') and at the Centre de Recherche Paul Pascal (CNRS) in Bordeaux ('Soft Micro Systems') with whom it was very wonderful to work. Thank you for the collaborations within these groups in Göttingen and Bordeaux, Philipp Gruner, Florine Maes, Deniz Pekin, Jérémy Vrignon, Quentin Brosseau, Ingmar Polenz, Laura Chacòn, Jiseok Lim, Ouriel Caën, Benoît Semin, Thomas Beneyton. I acknowledge Wolf

Pierre et Clement.

Vielen Dank an die Sportler – Merci à tous les sportifs – Thank you to all athletes. Danke an die Rhönradgruppen des TSVE 1890 Bielefeld und des ASC Göttingen 1846 für die guten Trainingseinheiten. Thank you my dear runners, climbers, surfers, swimmers and volleyball players for the good sport-work balance.

Vielen Dank an meine Mitbewohner Hanna, Kornelius, Enno, Freya für das entspannte und kurzweilige Zusammenleben & merci à mes colocs Johan, Bruno, Anaïs et Boris pour la cohabitation détendue et divertissante.

Special thank to my friends at the other side of the world, Stew, Cata, Brad, Alex, Krystal, Sam, Nicola, Ben and Annelie, for all the awesome time we have spent together even though living far apart.

Außerdem danke ich Inge, Dietmar und Farina F. für die schönen gemeinsamen Momente.

Ich bedanke mich zutiefst bei meiner Familie, die mich all die Jahre liebevoll unterstüzt hat und dies auch immer noch tut. Hierfür danke ich meinen Eltern, Ursula und Uwe, meinen Geschwistern, Swantje und Sören und meinem Opa, Gustav. Ich danke Alex für die liebevolle Unterstützung in jeder erdenklichen Situation.

Thank you very much

Merci Beaucoup   Vielen Dank   Ta Muchly   Grazie Mille
Muchas Gracias   Dziękuję bardzo   Muchas Gracias
ευχαριστώ   Çok teşekkür ederim   Muchas Gracias
Tatenda zvikuru   Благодаря   谢谢
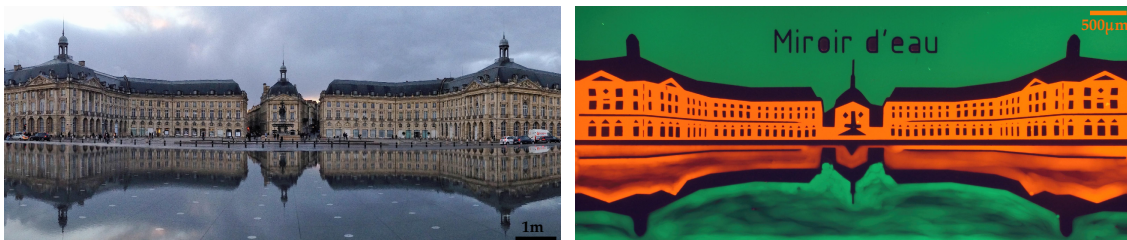
Figure 7.10: "Miroir d'eau" in Bordeaux with the "Place de la bourse" in the background. (left) Photo and (right) microfluidic chip (produced from mold in Fig. 3.1) with fluorescent dyes inside the channels (orange: 100 µM sulphorhodamine B, green: 10 µM fluorescein in water, experiment with D. Pekin, A. Vigne). The reflection pattern is generated flowing water-in-oil emulsions through the channels and using a high exposure time.
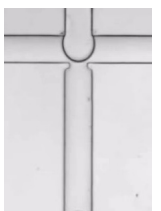
Birte Riechers

Curriculum Vitae

Personal Details

Date of Birth	23.06.1985
Place of Birth	Bielefeld
Nationality	German

Education and Research Experience

05/2012-12/2015	**PhD**, *Prof. Dr. J.-C. Baret*, From 05/2014: Centre de Recherche Paul Pascal, Centre National de la Recherche Scientifque, Soft Micro Systems, Pessac, France. From 05/2012: Max-Planck-Institute for Dynamics and Self-Organization, Droplets, Membranes & Interfaces, Göttingen, Germany.
	"Dynamics of Surfactants at Soft Interfaces using Droplet-Based Microfluidics": Characterisation of emulsions and their interfacial properties using conventional methods (pendant drop, Wilhelmy) and pH measurements at the micron scale using droplet-based microfluidics. pH detection in droplets on-chip with an optical setup. Stabilisation of emulsions with surfactants against coalescence and transport. Improvement of surfactant synthesis and analysis using infrared spectroscopy, light scattering, methods of exchange, microfluidics. Treatment of experimental data using MATLAB.
07/2012-08/2012	**Internship**, *Dr. V. Taly*, Université Paris Descartes, UMR-S775, France.
	"Surfactant synthesis for droplet-based microfluidics".
04/2008-07/2011	**Master of Science**, *Prof. Dr. T. Koop and Prof. Dr. A. Hütten*, Bielefeld University, Germany, Grade: 1.0.
	Chemistry, profile Physical Chemistry. Thesis: "Development of a microfluidic device for the production of water droplets for the investigation of homogeneous ice nucleation": Dynamic scanning calorimetry, droplet-based microfluidics. Master Studies: Focus on physical chemistry and spectroscopical methods for high resolution.
09/2010-11/2010	**Research**, *Prof. Dr. A. Hütten*, Bielefeld University, Germany.
	"Control of the morphology of cobalt nanoparticles in external magnetic fields": Synthesis of nanoparticles in bulk solution and analysis using transmission electron microscopy.
03/2009-10/2009	**Research**, *Prof. Dr. G. Metha*, University of Adelaide, Australia.
	"Experimental and Computational Study on Titanium and Tungsten Carbide Nanoparticles and Gold Ceria Oxide Clusters": Laser ablation techniques, Density Functional Theory of gold oxide clusters. Australian Synchrotron: Far infrared spectroscopy of nanoparticles.
10/2004-04/2008	**Bachelor of Science**, *Prof. Dr. T. Koop*, Bielefeld University, Germany, Grade: 1.5.
	Major Subject: Chemistry, Minor Subject: Science of Sport (Teaching Degree for High School). Thesis: "Modelling of water activities of ternary aqueous solutions".

Scholarships

05/2012-04/2015   **PhD**, "Göttingen Graduate School for Neurosciences, Biophysics and Molecular Biosciences" (GGNB), program: "International Max Planck Research School for Physics of Biological and Complex Systems" (IMPRS-PBCS), excellence stipend, Göttingen, Germany.

03/2009-06/2009   **Master Practical**, German Academic Exchange Service (Deutscher Akademischer Austauschdienst, DAAD), University of Adelaide, Australia.

Work Experience

04/2013-04/2014   **Teaching**, *Prof. Dr. J.-C. Baret*, Georg-August-Universität Göttingen and GGNB, Göttingen, Germany.
Microfluidics: Theory of droplet-based microfluidics, basic experiments, current research topics.

04/2008-03/2012   **Research, Teaching**, *Prof. Dr. T. Koop*, Bielefeld University, Germany.
Research on homogeneous ice nucleation. Teaching of physical chemistry: Kinetics and thermodynamics: Practical courses and tutorials.

05/2009-06/2009   **Teaching**, *Prof. Dr. G. Metha*, University of Adelaide, Australia.
Practical course of physical chemistry, examination.

Publications

2015   F. Maes, D. Pekin, B. Riechers, J. Vrignon, J.-C. Baret, Biomimetic behaviours in minimal soft matter systems, in preparation.

2015   B. Riechers et al., Adsorption kinetics of surfactants using pH measurements in droplet-based microfluidics at the micron scale, in preparation.

11/2015   P. Gruner, B. Riechers, B. Semin, J. Lim, A. Johnston, K. Short, and J.-C. Baret, Controlling molecular transport in minimal emulsions, *Nature Communications* **2015**, in press.

07/2015   P. Gruner, B. Riechers, L. Chacon, Q. Brosseau, F. Maes, T. Beneyton, D. Pekin, J.-C. Baret, Stabilisers for water-in-fluorinated-oil dispersions: Key properties for microfluidic applications, Current Opinion in Colloid & Interface Science, **2015** *20*, 183-191, doi:10.1016/j.cocis.2015.07.005.

04/2013   B. Riechers, F. Wittbracht, A. Hütten, and T. Koop, The homogeneous ice nucleation rate of water droplets produced in a microfluidic device and the role of temperature uncertainty, Physical Chemistry Chemical Physics, **2013** *15*, 5873-5887.

Selected Conference Contributions & Invited Talks

06/2015   B. Riechers, Surfactant adsorption in droplet-based microfluidics - Implications on exchange and biocompatibility, Brown University, Department Seminar: Department of Engineering and Physics, Providence, RI, USA, Invited Talk.

06/2015   B. Riechers, P. Gruner, F. Maes, J.-C. Baret, Dynamics of Surfactant Adsorption and Molecular Transport Across Interfaces in Droplet-Based Microfluidics, Physics & Chemistry of Microfluidics Gordon Research Conference 2015, Mount Snow, West Dover, VT, USA, Poster.

03/2015   B. Riechers, Surfactants in droplet-based microfluidics – Adsorption, Exchange and Biocompatibility, DPG Spring Meeting 2015, Berlin, Germany, Talk.

07/2014   B. Riechers, F. Maes, Q. Brosseau, and J.-C. Baret, Adsorption kinetics of surfactants determined by pH measurements in droplet-based microfluidics, Microfluidics 2014, Heidelberg, Germany, Poster.

04/2014   B. Riechers, Adsorption kinetics of surfactants in droplet-based microfluidics using pH measurements at the micron scale, DPG Spring Meeting 2014, Dresden, Germany, Talk.

04/2012   B. Riechers, F. Wittbracht, A. Hütten, and T. Koop, Investigation of Volume-Dependent Homogeneous Ice Nucleation of Water Droplets Using a Microfluidic Device, EGU General Assembly 2012, Vienna, Austria, Poster.